Fakultät für Physik
Technische Universität München

The Pacific Ocean Neutrino Experiment: feasibility study for a new Neutrino Telescope at Cascadia Basin, NE Pacific Ocean

Immacolata Carmen Rea

Vollständiger Abdruck der von der Fakultät für Physik der Technischen Universität München zur Erlangung des akademischen Grades eines

Doktors der Naturwissenschaften (Dr. rer. nat.)

genehmigten Dissertation.

Vorsitzender:
Prof. Dr. Andreas Weiler

Prüfende der Dissertation:
1. Prof. Dr. Elisa Resconi
2. Prof. Dr. Susanne Mertens

Die Dissertation wurde am 08.07.2021 bei der Technischen Universität München eingereicht und durch die Fakultät für Physik am 22.07.2021 angenommen.

> “ *Ma sopra tutte le invenzioni stupende, qual eminenza fu quella di colui che s'immaginò di trovar modo di comunicare i suoi più reconditi pensieri a qualsivoglia altra persona, benché distante per lunghissimo intervallo di luogo e di tempo? parlare con quelli che son nell'Indie, parlare a quelli che non sono ancora nati né saranno se non di qua a mille e dieci mila anni? e con qual facilità? con i vari accozzamenti di venti caratteruzzi sopra una carta.* ”
>
> Galileo Galilei,
> "Dialogo sopra i due massimi sistemi", 1632

Thesis advisor:
Professor Elisa Resconi

Abstract

This thesis summarises the design, assembly, and data analysis of the two pathfinder missions for the new neutrino telescope Pacific Ocean Neutrino Experiment (P-ONE).
P-ONE was conceived to extend and complement the field of view of the neutrino telescope IceCube at the South Pole and target the TeV-PeV detection energy range in the present multi-messenger era. With the other underwater neutrino detectors still in construction (KM3NeT and GVD), P-ONE will significantly boost the current sensitivity to high-energy cosmic neutrinos and reveal new phenomena in the extreme Universe.
Based on Ocean Networks Canada subsea infrastructure, the planned 70 moorings of P-ONE will be installed starting from 2023 at Cascadia Basin, a heavily sedimented abyssal plain region located at 2660 m depth about 200 km off Vancouver Island. Being identified as a potentially ideal site for a neutrino telescope, in spring 2018, the first pathfinder mission - STRAW (STRing for Absorption length in Water) - was constructed at TUM and deployed by ONC. To measure the water optical properties and evaluate the environmental background, STRAW is taking data since then. Afterwards, following up the promising STRAW results, in summer 2020 the second pathfinder mission - STRAW-b - was deployed 40 m from STRAW to test a more complex installation of a longer instrumented line and characterise the ambient background in more detail. Within this thesis, we describe the design of the pathfinders, the construction of the optical modules, and the first results from the Pacific Ocean. Focus is given to the data analysis of the STRAW long-term monitoring, which reveals the time behaviour of the ambient bioluminescence and its relation with other ambient parameters. We conclude with an outlook about the future of P-ONE.

Zusammenfassung

In dieser Arbeit wird der gesamte Entwicklungsprozess zweier Pfadfinder-Projekte dargestellt, vom Design über die Montage bis hin zur anschließenden Datenaufnahme. Diese zwei Projekte sind als die ersten Schritte einer Machbarkeitsstudie für ein neues Unterwasser-Neutrinoteleskop, P-ONE (Pacific Ocean Neutrino Experiment), geplant.
Die Idee von P-ONE entstand in der heutigen Multi-Messenger Ära, mit dem Ziel die Sichtfelder bereits existierender Neutrinoteleskope zu ergänzen und TeV-PeV Energien zu detektieren. Zusammen mit weiteren Unterwasser-Neutrinodetektoren, die sich noch in Konstruktion befinden, wird es die derzeitige Sensitivität bis zu den höchstenergetischen Neutrinos erhöhen. Unter Nutzung der Unterwasser-Infrastruktur von Ocean Networks Canada werden die geplanten 70 Verankerungen von P-One ab 2023 im Cascadia Basin angebracht. Cascadia Basin ist eine stark sedimentierte Abyssal-Ebene, die sich in 2660 m Tiefe befindet und etwa 200 km vor Vancouver Island zu finden ist.
Der erste Pfadfinder namens STRAW (STRing for Absorption length in Water) wurde im Frühling 2018 installiert, nachdem der Standort als idealer Kandidat identifiziert wurde. Das Ziel war die Messung der optischen Eigenschaften des Wassers und des Umgebungshintergrundes.
Im Anschluss an die vielversprechenden STRAW Ergebnisse wurde im Sommer 2020 der zweite Pfadfinder namens STRAW-b in 40 m Entfernung von STRAW ausgebracht, mit dem Ziel den Hintergrund zu charakterisieren.
In dieser Arbeit werden die Technologien, die für den Bau sämtlicher optischen Module verwendet wurden, ausführlich beschrieben und motiviert. Abschließend wird die Datenanalyse der STRAW Langzeitbeobachtung vorgestellt, mit besonderem Schwerpunkt auf den Hintergrund durch Biolumineszenz.

Contents

Introduction

Unveiling the mysteries of the Universe is one of the most intriguing challenges in the history of mankind. Generations of brilliant minded scientists have built our current knowledge of the Cosmos, pushing the boundaries to new open questions.

The Standard Model of particle physics describes accurately most of the experimental results collected so far, but it is not believed to be the final theory. Some still unanswered questions lead to the conclusion that the Standard Model is not complete and could represents a low energy limit of a still undiscovered fundamental theory, which can most likely be demonstrated at higher energies [1]. For example, according to the Standard Model the neutrino is massless and the three-family structure of leptons and quarks remains unexplained.

Higher energies needed for this kind of studies are so high that man-made particles accelerators could not reach them, also in the next future. In this framework *Astroparticle Physics* plays a fundamental role. Astroparticle Physics was born around 1912 with the discovery of cosmic radiation by Victor Hess, pointing out that part of natural radioactivity has an extraterrestrial origin. It is presently well known that cosmic objects are capable to accelerate protons and heavier nuclei up to 10^{20} eV (several orders of magnitude larger than the LHC energy), the so called *cosmic rays*.

The origin of Ultra High Energy Cosmic Rays is a puzzle for scientists since more than one century as still today the localisation of their acceleration sources is not straightforward: the presence of interstellar magnetic fields deviates the charged cosmic rays from their original path. At this scope it is needed to observe the same astrophysical event using the detection of particles that are not influenced by galactic or extragalactic magnetic fields, as *gamma rays* and *neutrinos*. Since also *gravitational waves* can be associated to high energy neutrinos (and gamma rays) emissions by the same source [2], their detection could provide additional information on the source emission dynamics.

The evolution of detector technology and some recent discoveries are opening a new golden age for fundamental physics research: the Multi-Messenger Era.

Two major milestones are tracing the path: the detection of high energy neutrino events from a single-point source by IceCube [3] and the first observation of gravitational waves by the LIGO/Virgo Collaboration [4]. The combined (and coordinated) detection of cosmic-generated high-energy neutrinos, gravitational waves, gamma rays, electromagnetic signals and cosmic rays represents an unprecedented source of information to study some of the most mysterious processes in the physical Universe. A coincident detection of gravitational waves and high-energy neutrinos has not yet been achieved, thus becoming the next big challenge of the astroparticle physics community. To this effort, the involved scientific collaborations are already implementing an ambitious upgrade program. A significant (probably decisive) boost will be provided by the realisation of new observatories, aimed at extending and complementing the energy range and the field of view of the existing ones.

Within such a scientific framework P-ONE neutrino telescope has been conceived. P-ONE aims to become an observatory for cosmic neutrinos in the boreal hemisphere at Cascadia Basin (Northern Pacific Ocean, offshore Vancouver Island), optimised for the detection of high-energy events. The project is currently in its developing phase thanks to the work of research groups from Canada, USA and Germany, with the precious effort of Ocean Networks Canada (ONC) that manages the underwater infrastructure that will host the neutrino telescope.
Different detector layouts and geometries are under evaluation, through an extensive simulation campaign, while the most advanced and reliable technologies are being explored as potential candidate solutions for P-ONE. Moreover, the extremely hostile environment of the deep-ocean water and the high variety of possible background sources determine an additional set of design constraints. Environmental parameters like deep-ocean currents and salinity, are already routinely monitored with high accuracy by ONC observatories. For all other factors, two dedicated test campaigns have ben carried out: the STRAW and STRAW-b pathfinders. The main scientific target of STRAW is to achieve a precise measurement of the optical properties of the candidate site water: attenuation length, scattering length and long-term monitoring of ^{40}K and bioluminescence background rate, all fundamental parameters for the detector design process.
STRAW-b is mainly focused on the characterisation of background sources spectra, with a special focus on the bioluminescence emission and atmospheric muon background.

Within this work, I was involved in the definition, integration, test and calibration phases for both pathfinder missions. For STRAW, I focused on the procurement and the following characterisation of the PhotoMultiplier Tubes. I contributed to the assembly and to the calibration of the optical modules besides the mechanical integration of the two mooring lines.
For STRAW-b, I have been responsible for the realisation of one of the detection modules: the Minispectrometer. In this context, I took part to all the project phases: design, characterisation, integration and calibration.

After STRAW deployment and for all the data-taking phase (still ongoing) I analysed STRAW data for the search and long term monitoring of bioluminescent background. This thesis will span over the full projects timeline: after an introductory part devoted to UHECR astroparticle physics and multi-messenger astronomy in Chapter 1, an overview about neutrino astronomy and neutrino telescopes will be presented in Chapter 2. Chapter 3 is fully dedicated to the STRAW project: from design to implementation. In Chapter 4, the STRAW-b pathfinder is thoroughly described, with a special focus on the Minispectometer module project. The last chapter of the thesis, Chapter 5, is fully dedicated to the STRAW data analysis: monitoring tools, site characterisation and study of bioluminescence phenomena.

“ *Non posso tacer quello che mille volte ho osservato, e non senza riso, cadere nella mente quasi di tutti gli uomini nel primo motto che sentono di questo muoversi la Terra, creduta da loro talmente fissa ed immota, che non solamente di tal quiete mai non hanno dubitato, ma fermamente creduto che tutti gli altri uomini insieme con loro l'abbiano stimata creata immobile e tale mantenutasi in tutti i secoli decorsi; e fermatisi in questo concetto, stupiscono poi nel sentire che alcuno le conceda il moto* [...]. *Ora, che tale stoltissimo pensiero [...] trovi luogo nelle menti de gli uomini vulgari e di senso leggiero, io non me ne meraviglio; ma che gli Aristoteli e i Tolomei siano essi ancora incorsi in questa puerizia, mi par veramente assai più strana ed inescusabil semplicità.* **”**

Galileo Galilei,
"Dialogo sopra i due massimi sistemi", 1632

Chapter 1

Cosmic Rays and Multi-Messenger Astronomy

The detection and the study of cosmic messengers are fundamental for the knowledge of acceleration and production mechanisms of the astrophysical sources. Different messengers as high energy cosmic rays, gamma rays, neutrinos and gravitational waves can provide complementary information according to their features.
In some cases, astrophysical sources of gravitational waves[1] are expected to emit also photons and neutrinos: the merger of binary systems containing a neutron star, for example, or the core-collapse of massive stars like Supernovae are associated with Gamma-Ray Bursts emission, whose ejected sub-relativistic material interacts with the interstellar medium possibly generating Ultra High Energy Cosmic Rays (UHECRs).
Identifying a source with UHECRs detection is challenging due to the incoming magnetic fields that deflect them inside and outside our Galaxy. Gamma-rays and neutrinos, resulting from the interaction of cosmic rays with matter or photons in the surroundings of cosmic accelerators, do not interact with magnetic fields along their path. For this reason, they can provide complementary insight into the physics of their origin.

The multi-messenger astronomy development needs interdisciplinary efforts to interpret observations and constrain models. In the next future, the collaboration between the different gravitational waves, gamma rays, neutrinos and cosmic rays communities will be fundamental to implement shared observational and analytic strategies [2].

---

[1] In September 2015 the two detectors of the LIGO Observatory (LIGO) [4] detected for the first time a transient signal of gravitational waves.

1.1 Cosmic rays and their mass composition

High-energy particles and atomic nuclei produced and accelerated by several possible sources and mechanisms travel through space at nearly the speed of light. These particles are defined as *cosmic rays*.

Cosmic rays were discovered by Victor Hess in 1912. In his balloon experiment, an ionization chamber was operating in the atmosphere up to a quota of 5km. During the ascent, he observed that the level of radiation first decreased but then, from about 1000 m, began to increase with increasing distance. This measurement led to the conclusion that the radiation must have an extraterrestrial origin and that its intensity decreased at sea level because of the atmosphere interaction [5]. Around 1920 Robert Millikan called this radiation "cosmic rays".

The cosmic rays outside the atmosphere are called *primary cosmic rays* and consist of high-energy protons (about 90%) and in smaller quantities helium nuclei, electrons, photons, neutrinos and antimatter (positrons and antiprotons). Travelling towards the Earth surface, these particles interact with the atmospheric nuclei leading to the formation, in a cascading process, of an *air shower* of new particles called *secondary cosmic rays*. For a cosmic ray proton and a nucleon (N), the basic reaction is the following:

$$p + N \rightarrow \pi^{\pm}, \pi^{0}, K^{\pm}, K^{0}, p, n, ... \tag{1.1}$$

Secondary cosmic rays can interact or decay, producing an exponential multiplication of the number of particles. According to their configuration, three main components can be identified within a shower: hadronic, electromagnetic and muonic, as illustrated in fig. 1.1.
The hadronic component is composed of neutrons, protons, kaons and pions, and strongly interacts with nuclei in the air, producing a cascade of hadronic particles with different energies [6].
The electromagnetic component is mainly originating from the decay of neutral pions $\pi^0 \rightarrow \gamma + \gamma$ with consequently pair production of positrons and electrons.
The muonic component is generated by the decay of $\pi^{\pm}$ and $K^{\pm}$: weakly interacting muons with relativistic energies produced in the shower are capable of reaching Earth surface despite their short half-life (2.2 μ s).
In addition, positive and negative pions (and consequently muons) decays produce showers of neutrinos (and antineutrinos): we refer to these neutrinos as *atmospheric neutrinos* and, as will be described in paragraph 2.2.3, these represent one of the principal background sources for neutrino telescopes.

The range of energies covered by the cosmic ray spectrum extends over 11 orders of magnitude, from 10^9eV to 10^{20}eV. Current accelerators can

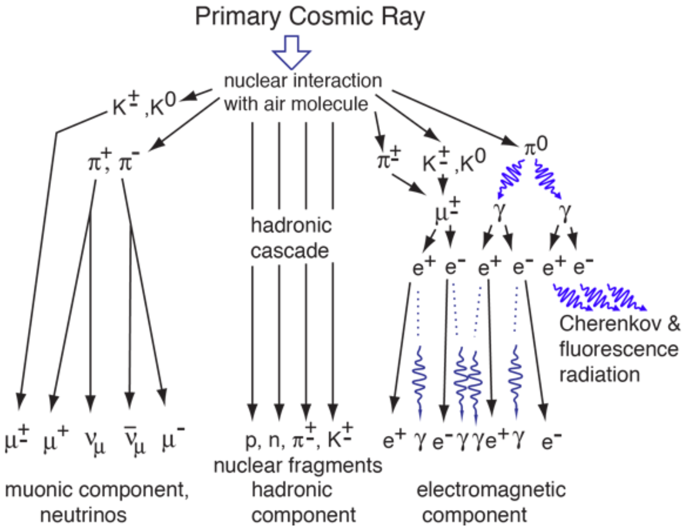

Figure 1.1: Illustration of a primary cosmic rays interacting with an atmospheric nucleus and producing an air shower of secondary particles. According to the decays processes, three main components can be identified: electromagnetic, muonic and hadronic. Picture taken from http://hydrogen.physik.uni-wuppertal.de/hyperphysics/hyperphysics/hbase/astro/cosmic.html

reach a maximum energy of TeV, way lower than the most energetic cosmic rays. For this reason, these represent one of the natural laboratories for the exploration of physics beyond the Standard Model.

The flux decreases rapidly vs energy: it goes from about 1000 particles per second per m^2 at the energies of GeV (10^{9}eV) to about one particle per year per m^2 at the energies of PeV (10^{15}eV). The flux drops to less than one particle per century per km^2 above EeV (10^{18}eV). The detection of cosmic rays at low energies up to 10^{15} eV is then possible in space with satellites and balloons. Anyway, to cover the higher energy range and collect adequate statistics, large surface instruments are required.

The plot in fig. 1.2 reports the observed energy spectrum of cosmic rays. It can be in first order approximated by an inverse power-law distributions with spectral index γ:

$$\frac{d\Phi}{dE} := \frac{d^4N}{dEdAd\Omega dt} \propto E^{-\gamma} \tag{1.2}$$

The γ index changes at two different points in the spectrum: the *Knee* at 10^{15} eV, and the *Ankle* at 10^{18} eV. At the beginning of the spectrum the power law index is 2.7, then from the Knee its value becomes 3.1, and then back to 2.7 at EeV energies. A less distinct change in the shape of the spectrum is the *Second Knee*, which can be found around 10^{16} eV. The spectrum then *cuts off* at very high energies around 10^{20} eV [8] [1]: this effect was

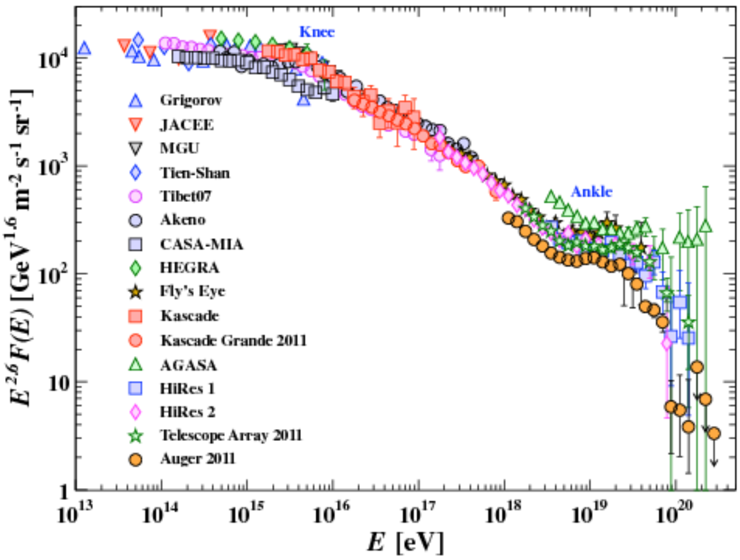

Figure 1.2: From [7]: The all-particle spectrum as a function of E (energy-per-nucleus) from air shower measurements. The differential energy spectrum has been multiplied by $E^{2.6}$ in order to display the features of the steep spectrum that are otherwise difficult to discern.

predicted by K. Greisen, V. Kuzmin and G. Zatsepin in 1966 and for this reason is called *GZK cut-off*. Its final interpretation remains elusive: it is not yet clear if the GZK cutoff is produced by the GZK mechanisms (see paragraph 1.2.3) or is related to sources running out of power.
Different energy regions in the spectrum may indicate a change in the emission from different sources, propagation processes and compositions. The lower energy part (up to few GeV) is dominated by cosmic rays originating in the Solar system. The region between few GeV up to the Knee is dominated by particles accelerated inside our Galaxy. The energy range between the Knee and the Ankle is dominated by particles accelerated inside and outside our Galaxy. The highest energy region is associated only with extra-galactic cosmic rays.

The cosmic rays *mass composition* varies in the path from the source to the Earth due to interactions with the interstellar medium (ISM): the main component is identified by protons and helium nuclei. Electrons and positrons contribute with few percentages [9] because of energy loss during their propagation. Small quantities of nuclei heavier than helium up to $Z \leqslant 30$

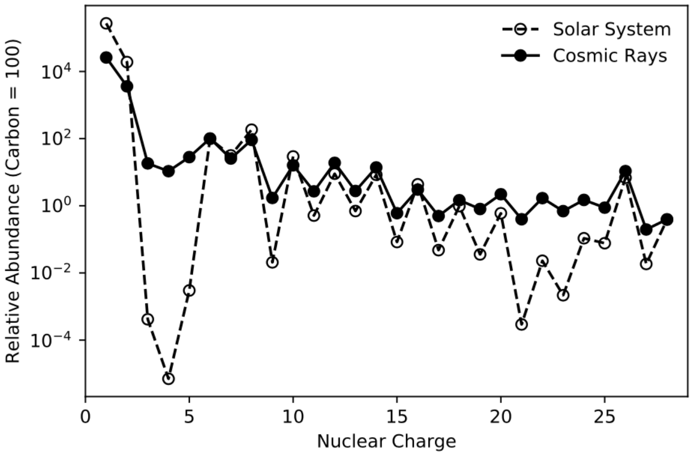

Figure 1.3: Relative abundance of elements in cosmic rays at Earth (solid circle, filled line), compared with the relative abundance of elements in the Solar System (open circle, dashed line). In the abscissa the atomic number Z is reported. It is found that the chemical composition of cosmic rays coincides, approximately, with that of the solar system. Reference is Carbon=100. Data is measured at energies between 100 MeV and 1-2 GeV [10].

are also present: their importance is based on the propagation mechanism information they can provide. The graph in fig. 1.3 shows the relative abundances of different elements in cosmic rays and in the Solar System as a function of the atomic number Z, normalized at the abundance of carbon, set at 100%. The chemical composition of cosmic rays at the source is presumably identical to the Solar System one. Anyway, the relative abundances of the various elements (Li, Be, B and Sc, Ti, V, Cr, Mn) is different at their detection: the interaction of cosmic rays with the interstellar medium makes the heavier nuclei split (*spallation*) into light nuclei, hence the relative overabundance of light elements with respect to the heavy ones.

1.2 Acceleration mechanisms and sources

The origin and the acceleration mechanisms of the cosmic rays, able to boost particles to the extremely high energies observed on the Earth, remain today not well understood.
There are two main classes of acceleration mechanisms [5]:

- *bottom-up*, that assumes the production of cosmic rays in astrophysical sources;
- *top-down*, that hypothesises the cosmic rays coming from exotic particles decay.

A statistical acceleration mechanism, in the framework of the **bottom-up** scenario, was suggested by Enrico Fermi in 1949 [11]: he assumed that individual charged particles could accelerate because of repeated collisions with large masses of moving magnetized plasma. It is the principal candidate mechanism for the particles to gain non-thermal energies.
Two types of Fermi acceleration have been discussed in the literature:

- the *First Order Fermi Acceleration* that occurs in shocks waves, where moving magnetic inhomogeneities that encounter a charged particle reflect it through the shock (from downstream to upstream) at increased velocity. If a similar process occurs multiple times back and forth, the particle will be accelerated at higher energies;
- the *Second Order Fermi Acceleration* occurs in moving magnetized gas clouds, "magnetic mirrors". If the magnetic mirror is moving towards the charged particle, this latter energy will increase upon reflection. The energy gained at each reflection depends on the mirror velocity squared β_m^2.

Both cases are collisionless because frequent collisions with the environment particles can cause high energy losses by non-thermal energy particles and, as a result, no acceleration will occur.
The main feature of the Fermi acceleration model is that, even if depending on the parameters used to describe the magnetic clouds, the spectral index calculated for a standard case of a plane shock front (in a mono-atomic gas) is close to the one measured in the observed cosmic rays energy spectrum [1].

The maximum energy E$_{max}$ at which a source can accelerate cosmic rays depends on its size and its magnetic field intensity [12] [5]:

$$E_{max} \simeq ZBR \tag{1.3}$$

where *Z* is the charge of the accelerated particle, *B* is the intensity of the magnetic field, and *R* is the size of the source. When the Larmor radius[2] of a charged particle moving inside a magnetic field becomes greater than the size R of the source, the particle is not contained anymore inside it and escapes.
The relation between the size R of the acceleration region and its magnetic field intensity B responsible for the shocks are represented in the so-called *Hillas plot*, fig. 1.4. he astrophysical objects lying above the lines in fig. 1.4 represent possible candidate sources for the acceleration of particles up to 10^{20}eV energies such as neutron stars with strong magnetic fields, Active Galactic Nuclei (AGN) jets, pulsars and Gamma-Ray Bursts (GRBs).

---

[2] The Larmor radius, or gyroradius, is the radius of the orbit of a charged particle moving in a uniform, perpendicular magnetic field, obtained by simply equating the Lorentz force $\mathbf{F} = \mathbf{q}(\mathbf{E} + \mathbf{v} \times \mathbf{B})$ with the centripetal force.

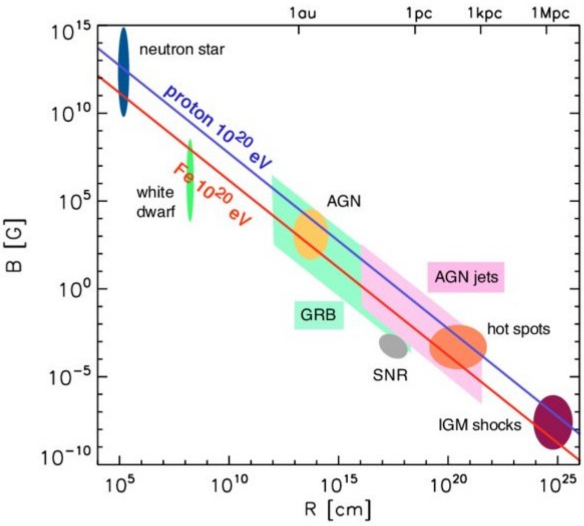

Figure 1.4: The Hillas diagram shows the size and the magnetic field intensity of possible sites of particle acceleration. Sources above the blue line are capable of accelerating protons up to 10^{21}eV, while sources above the red line are capable of accelerating iron atoms up to 10^{20}eV [13].

In the **top-down** scenario [5] is foreseen the production of particles by decays of exotic super-heavy particles (with masses at least of the order of 10^{21}eV): the candidates can be X bosons predicted by Grand Unification Theories (GUT)[3], super-heavy dark matter particles, heavy relics from the early Universe that are assumed to decay. There are two main classes of such models:

- the first one foresees the decay or annihilation of topological defects (TDs), like magnetic monopoles or strings, produced in the early Universe. From the TDs, supermassive particles are produced, which in turn decay into quarks and leptons. The former hadronize into jets containing mesons and small percentages of baryons. The pions thus produced decay into photons, neutrinos and antineutrinos, $e^{\pm}$ and muons, and cosmic rays would be the result of these secondary decays;
- the second one foresees the decay of supermassive particles produced directly in the primordial Universe and which have an average

---

[3] A Grand Unified Theory (GUT) is a model in particle physics in which, at high energies, the three gauge interactions of the Standard Model comprising the electromagnetic, weak and strong forces are merged into a single force.

lifetime longer than the age of the Universe. These particles are supposed to be part of the cold dark matter, hence the name "super-heavy dark matter (SHDM) particles". According to these models, very high energy photons and neutrinos are produced during the decay of the super-heavy particles into standard model particles.

The top-down models are strongly disfavoured by current experimental observations.

1.2.1 Galactic Cosmic Rays

Shock waves generated by Supernovae Remnants (SNRs) explosions are ideal candidates to explain the acceleration of cosmic rays to energies up to the *Knee* region around 10^{15}eV, as proposed by Fermi and as supported by many recent observations. Charged particles are scattered by the extreme magnetic fields of the expanding shells of Supernovae and gain a large amount of energy at each recrossing of the shock wave until they can escape the acceleration site.

The high density of the compressed core of a Supernova, combined with the increased energy of the charged particles, leads to the generation of neutrons and neutrinos through the *electron capture* process:

$$p + e^- \rightarrow n + \nu_e \tag{1.4}$$

The neutrinos escape from the source. The maximum energy attainable in this process is limited by the average lifetime of the supernova shell ($\sim 10^5$ years) and its size. A typical SNR can provide energies up to 10^{15}eV. Under particular conditions (extreme high density and strong interaction with the magnetic field), cosmic rays may reach energies of the order of 10^{17}eV.

Observation in association with the acceleration site of cosmic rays is impossible as they undergo deflection by the galactic magnetic field. Therefore, an isotropic flow of radiation is expected.

An additional candidate source of high energy cosmic rays are Pulsar Wind Nebulae (PWN). In PWN, the engine that powers and accelerates charged particles is represented by pulsars (rapidly rotating neutron stars), producing extremely intense magnetic fields by the gravitational collapse of massive stars.

Binary systems can also act as accelerators: an enormous gravitational potential energy is released by the collapse of a compact object (e.g. black hole, neutron star etc.) after the accretion of matter by a donor partner. The high-energy jets produced by such collapses represent an ideal environment for cosmic particles acceleration [6].

1.2.2 Ultra High Energy Cosmic Rays

In the energy range above the *Knee*, accelerated charged particles can escape from the magnetic field of their source origin and can travel through intergalactic space.

The sources of such high energy particles are under investigation since many years: it is difficult to locate them because, as already said, cosmic rays are charged particles undergoing angular deflections due to the magnetic fields in our galaxy and to the intergalactic medium between the sources and Earth.

The Pierre Auger Observatory (PAO) showed that UHECRs (above $\sim 6 \cdot 10^{19}$eV) arrival directions seem to be correlated with the position of nearby extragalactic sources [14], whose flux has not been reduced by interaction with the cosmic background radiation. Supermassive black holes at the centre of nearby galaxies, Active Galactic Nuclei (AGN), have been tentatively associated with UHECRs.

The AGN are among the most luminous sources in the Universe. A central supermassive black hole incorporates matter from the surrounding region, with the possible emission of two relativistic jets perpendicular to the accretion disk. One scenario foresees that particles in the jets can be accelerated up to ultra-high energies [1].

The Auger experiment has recently observed a large-scale anisotropy in the arrival direction of particles with energies above $8 \cdot 10^{18}$eV. This observation supports the extragalactic origin [15]. However, the Auger results do not unambiguously identify in the closest to our galaxy AGNs the only possible origin of such high energy particles.

Gamma-Ray Bursts (GRBs) are considered as other extreme accelerators up to 10^{20}eV. They are extremely energetic electromagnetic explosions occurring both in massive star core collapses like a supernova or hypernova, and in a binary system merger (e.g. neutron star - neutron star). These represent one of the most energetic transient objects in the Universe [8].

Neutron stars are also a suggested origin for UHECR: the very high magnetic field creates a relativistic magnetic wind believed to accelerate iron nuclei remaining from a previous supernova explosion.

More exotic scenarios are also discussed in the literature. One of the latest hypotheses on the origin of UHECRs associates them with the ability of AGNs to convert Dark Matter (DM) into high energy protons [16]. Heavy dark matter particles can decay into pairs of heavier virtual particles interacting with ordinary matter. The process involved in this production mechanism is the *Penrose process*[4], which theorises that one of the produced particles can fall into the black hole and the other escapes, colliding with other incoming DM particles. These very high energy collisions can produce very high energy protons that can be observed on Earth.

---

[4] The *Penrose process* theorises that energy can be extracted from a rotating black hole and that the extraction can occur if the rotational energy of the black hole is located in a region called *ergosphere* [17], outside the event horizon.

1.2.3 GZK limit

As described in the paragraph 1.2.2, at the energy above 10^{18} eV (the *Ankle*) cosmic rays are associated to extragalactic origin.
At $6\cdot 10^{19}$ eV the energy spectrum shows an abrupt steepening (see fig. 1.2), a so called *cut-off*. This effect was predicted by K. Greisen, V. Kuzmin and G. Zatsepin in 1966 (GZK) as the interaction of high energy protons with Cosmic Microwave Background (CMB) photons, producing Δ^+ resonances according to the processes 1.5 and 1.6:

$$p + \gamma_{CMB} \rightarrow \Delta^+ \rightarrow n + \pi^+ \tag{1.5}$$

$$p + \gamma_{CMB} \rightarrow \Delta^+ \rightarrow p + \pi^0 \tag{1.6}$$

The first decay channel follows the β decay for the unstable neutron (n $\rightarrow$ p + e^- + $\bar{\nu}_e$) while the pion π^+ decays into $\mu^+ + \nu_\mu$. The second decay channel is characterised by the production of two photons by the neutral pion π^0. Both decays produce high energy neutrinos or photons, pointing out the importance of very high energy neutrinos detection in astroparticles physics.
The GZK limit assumes that very high-energy cosmic rays are protons. Observations from the Pierre Auger experiment, however, suggest that most ultra-high-energy cosmic rays are heavier elements, as shown in fig. 1.5 [18]. In this case, the GZK limit is not consistent with the original hypothesis. However, there is no fundamental contradiction in observing heavier cosmic rays with energies that violate the above-mentioned limit since there is another *cut-off* interpretation that identifies the spectrum maximum energy as a consequence of the maximum possible acceleration of cosmic rays sources [19].

1.3 Cosmic Messengers

Cosmic rays can reach energies way higher than particles generated by existing accelerators. As already described in previous paragraphs, the fundamental issue about their origin cannot be answered yet because of their deflection in magnetic fields. For this reason, considering only cosmic charged particles may not be sufficient to get the final information on their sources [20]. However, the possible cosmic rays sources potentially satisfy the requirements for the production of astrophysical auxiliary messengers, as *gamma rays* and *neutrinos*. The detection and the study of high-energy extraterrestrial gamma rays and neutrinos spectra have recently represented a fundamental field of research since the additional information provided can contribute to the understanding of the cosmic rays origin [21] [22].
The study of the *gravitational waves* can reveal different information about

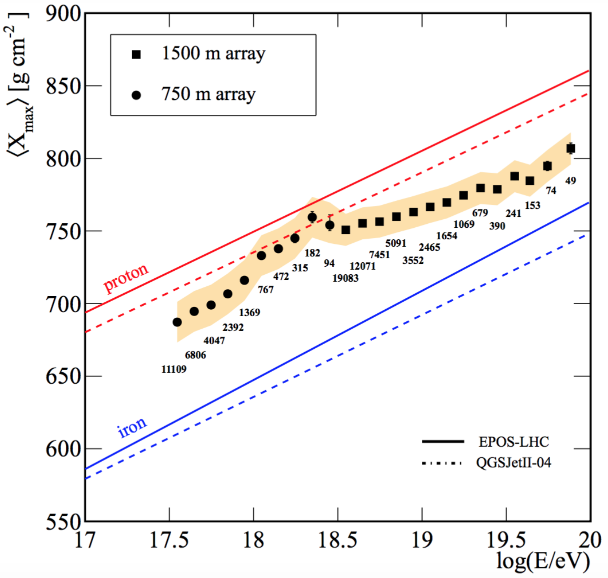

Figure 1.5: From [18]: Mean values of the X_{max} distributions obtained with the data of the 750 m and 1500 m surface arrays as a function of the energy. The shaded area indicates the systematic uncertainties. Data are compared to the predictions from simulations of protons and iron nuclei for two different hadronic models. The number of selected events in each energy bin is indicated.

astroparticles sources and their acceleration mechanism: the coordinated interpretation of these different types of "messenger" signals is known as **multi-messenger astronomy** and is summarised in fig. 1.6.

1.3.1 Gamma-rays

Gamma rays are high energy photons. Usually, the frequency of this radiation is higher than 10^{20} Hz, so it has an energy of over 100 keV and a wavelength of less than $3{\cdot}10^{-13}$ m, much less than an atom diameter.
Gamma rays can be produced by different interactions in the surroundings of a source or during cosmic rays travel along their path in the interstellar medium. The emission of photons can occur through leptonic and hadronic processes:

- the energy loss of cosmic ray particles by galactic and extra-galactic magnetic or electric fields (respectively *synchrotron radiation* and *bremsstrahlung*);
- the scattering between an ultra-relativistic electron and a photon, transferring to this latter some of the incident energy (*inverse Compton effect*);

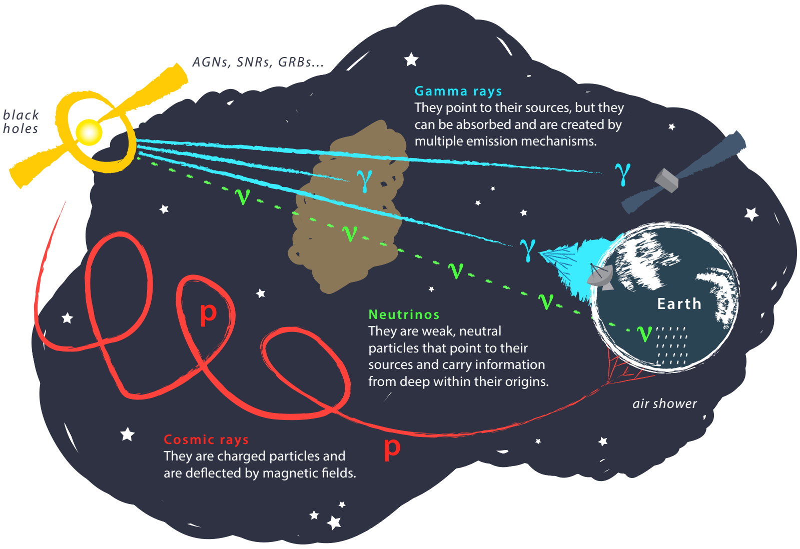

Figure 1.6: From [23]: Propagation of different messengers from an astrophysical source towards the Earth.

- the interaction of cosmic rays with interstellar gas molecules and the consequent production of π^0 that, in turn, decays into photons (*astrophysical beam dump mechanism* $p + p \rightarrow \pi^+, \pi^-, \pi^0, K^+, K^-, K^0$...).

Differently from cosmic rays, photons are not deflected by magnetic fields. For this reason, they point directly at their source. Anyway, the opaqueness of the atmosphere to high energy photons (see fig. 1.7) sets a limit to their probability of reaching the Earth. Ground telescopes are used for the detection of high energy gamma rays [5] while space satellites cover the lower energy range from MeV to GeV.
Photons at very high energy interact with the Extragalactic Background Light (EBL) and the Cosmic Microwave Background (CMB) radiation, undergoing a significant attenuation above tens of TeV. Because of this attenuation, the detection of photons at the Earth is correlated to their amount of energy. For example, photons with 10^{15} eV generate electron-positron pairs after interacting with a CMB photon and their probability to reach the Earth decreases.

---

[5] Gamma rays interact electromagnetically with the atmosphere and produce electrons and positrons with enough energy to generate Cherenkov light. This light is detected by ground-based large arrays of telescopes.

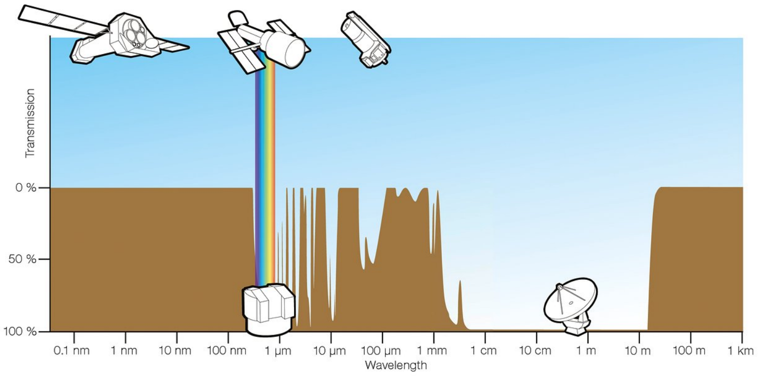

Figure 1.7: Transparency of the atmosphere: In this diagram, the brown curve shows how transparent the atmosphere is at the given wavelength to radiation from space. The main windows are at visible wavelengths (marked by the rainbow) and at radio wavelengths from about 1 mm to 10 m. Credit: ESA/Hubble (F. Granato) $https : //www.eso.org/public/images/atm_{o}pacity/$.

1.3.2 Neutrinos

Neutrinos are weakly interacting particle with small mass and no electric charge. Like gamma rays, they don't interact with magnetic fields and are not deflected along the path from their source to the Earth. Therefore, they point directly to their origin.
Due to the low cross-section, they can travel through the interstellar medium essentially without obstacles and, consequently, the corresponding observable Universe is not limited at a specific energy range.
Even if the neutrinos low interaction probability is a key feature for their travel towards the Earth, it makes their detection very challenging, since kilometre-scale of instrumented volumes of ice or water is needed.
However, they are valuable cosmic messengers that can provide additional information about astrophysical sources generation and acceleration mechanism at highest energies that, as described in paragraph 1.3.1, are opaque to photons.

In the Chapter 2, neutrino generation processes and detection techniques will be thoroughly described.

1.3.3 Gravitational waves

Gravitational waves are perturbations of spacetime curvature generated by accelerated masses: they can propagate from their source at the speed of light.
They can be considered a form of radiation, as the distances between points within the gravitational field rhythmically contract and expand, generating wavefronts of high intensity. The cosmic phenomena associated with

gravitational waves production are explosions of supernovae or collision of objects such as neutron stars and black holes, binary stars and pulsars, producing huge masses changes.

They were predicted in 1916 by A. Einstein [24] as part of the general relativity theory. Anyway, their existence was finally demonstrated only in September 2015 by the LIGO experiment [4], after the detection of a signal generated by the merger of two black holes. Such observation provided evidence of the merger of stellar-mass binary black holes and the existence of black holes with a mass higher than 25 solar masses.

In the multi-messenger astronomy framework, gravitational waves can be associated with high energy neutrinos (and gamma rays) emissions by the same source [2]. For example, gravitational waves sources (like binary neutron stars and black hole mergers) can emit relativistic outflows that are signatures of high energy neutrinos emission. Such detection from well-known sources could help establish the connection between the dynamics of the progenitor and the properties of the outflow [25].

> “ *Ma vengo ad un altro punto. Sopra che fondamento dice egli che le stelle appariscano cosí piccole? forse perché tali le veggiamo noi? e non sa egli che questo viene dallo strumento che noi adoperiamo in riguardarle, cioè dall’occhio nostro? E che ciò sia vero, mutando strumento le vedremo maggiori e maggiori, quanto ne piacerà: e chi sa che alla Terra, che le rimira senza occhi, elle non si mostrino grandissime e quali realmente elle sono?* ”

Galileo Galilei,
"Dialogo sopra i due massimi sistemi", 1632

Chapter 2

Neutrino Astronomy

Three hours before the visible light from the supernova SN 1987A reached the Earth, a flux of neutrinos was observed simultaneously in three separate detectors built to study the solar neutrino problem[1].
The observation of solar neutrinos and neutrinos from the supernova 1987A led to a new discipline: the High Energy Neutrino Astronomy, thus extending conventional astronomy beyond the usual electromagnetic messengers.
High energy neutrinos are produced in the most energetic events in the Universe and, due to their small cross-section, they can travel from astrophysical objects to the Earth without interacting along their path, pointing to their origin.
The small cross-section is a benefit, on one side, since it allows neutrinos to escape from the core of their sources, bringing out information on the internal processes. On the other side, the disadvantage is that their challenging detection requires huge target masses to achieve appreciable event rates: it is hence convenient to exploit *deep* underwater or ice sites as "natural" neutrino detectors [26].
The first idea of building such a *neutrino telescope* was developed by Markov [27] around the '60s. The working principle consisted in the detection of secondary particles produced by neutrino interactions through arrays of light sensors distributed over a large volume of transparent material.

---

[1] The *solar neutrino problem* refers to the discrepancy between the observed flux of solar neutrinos and the theorised one. From the first observation in the 1960s, the problem has been solved only in 2002. According to the Standard Solar Model, the Sun is expected to produce only electron neutrinos, ν_e. Anyway, the number of solar ν_e detected by neutrino experiments was one half or one-third of the predicted ones. Thus the Standard Model of the particles has been modified to include neutrino *oscillations*: the neutrinos produced in the Sun are not massless particles and a neutrino created with a specific flavor can change during its propagation and can afterwards be measured to have a different flavor.

2.1 What is a *neutrino*?

The *neutrino* is an elementary subatomic particle with spin of 1/2 (fermion) that interacts only via weak interaction[2] and gravity; hence it typically passes through matter without being absorbed. It is electrically neutral and its mass is so extremely small, 0.05 eV/c^2, that it was thought to be zero for a long time.

The neutrino was postulated by Wolfgang Pauli in 1930 to explain the beta decay mechanism (see 2.1.1) and was, later in 1934, studied by Enrico Fermi. Only in 1956, 22 years later, it was discovered by Clyde Cowan and Fred Reines [28], during an experiment at the Savannah River reactor (Nobel Prize 1995).
The two scientists, assuming the production of electron antineutrinos in the reactor by beta decay (during the nuclear fission, the produced free neutrons undergo beta decay), placed a large water tank nearby. The electron antineutrinos interacted with the protons of the water through the reaction 2.1:

$$\bar{\nu}_e + p \rightarrow n + e^+. \tag{2.1}$$

The generated e^+ annihilated with a random e^- producing two γ rays; the neutron could be captured by a nucleus producing a γ ray. Thus the detection of these two simultaneous γ events has been the electron antineutrino interaction prove and, consequently, it was the first direct evidence of its existence.
There are three different flavors of neutrinos: the electron neutrino ν_e, the muon neutrino ν_μ and the tau neutrino ν_τ (with their respective antineutrinos) according to the three lepton families of the Standard Model of particles. Until recently, they were thought to be massless, but the discovery of *neutrino oscillations* led to the awareness that they do have mass.
A neutrino generated with a specific lepton flavor can be detected with a different lepton flavor, after a certain propagation in space. First predicted by Bruno Pontecorvo in 1957, this oscillation phenomenon and the consequent neutrino mass has been discovered by the Super-Kamiokande Observatory [29] and the Sudbury Neutrino Observatories (Nobel Prize 2015). The observation regarded the atmospheric muon neutrinos generated by cosmic rays-atmosphere collision. In particular, the number of upward going ν_μ was half of the number of down going ν_μ. The reason was attributed to the flavor change of the upward going ν_μ that, after passing the Earth, turned into (not detected at that moment) ν_τ.

Due to their mass, then, neutrinos can oscillate between their flavors: os-

---

[2] The weak interaction belongs to the four fundamental interactions and it is connected to atoms radioactive decays. It involves leptons and quarks (semileptonic interactions), only leptons (leptonic interactions) or only quarks (non-leptonic interactions) through the exchange of W$^\pm$ and Z bosons (vector bosons with mass).

cillation phenomena can be explained by the *mixing* between their flavor eigenstates $|\nu_\alpha\rangle$, with α = e, μ, τ, and their mass eigenstates $|\nu_i\rangle$, with i= $1, 2, 3$, through the $U_{\alpha i}$ unitary 3x3 transformation (Pontecorvo-Maki-Nakagawa-Sakata matrix) following the 2.2 [8]:

$$|\nu_\alpha\rangle = \sum_i U^*_{\alpha i} |\nu_i\rangle \qquad |\nu_i\rangle = \sum_i U_{\alpha i} |\nu_\alpha\rangle \tag{2.2}$$

Hence, each neutrino flavor state is a linear combination of the three discrete mass eigenstates and viceversa and the probability that a neutrino originally of flavor α, after a distance L, can be detected as having flavor β can be expressed as 2.3:

$$P_{\alpha\to\beta} = \left|\left\langle \nu_\beta(L) \middle| \nu_\alpha \right\rangle\right|^2 = \left| \sum_i U^*_{\alpha i} U_{\beta i} e^{-i\frac{m_i^2 L}{2E}} \right|^2 . \tag{2.3}$$

Due to the weak nature of neutrino interactions, neutrino oscillation experiments are very challenging. In addition, they are currently sensitive only to the squared difference between the masses $\Delta m^2_{ij} = m^2_i - m^2_j$, but not to the absolute mass of the neutrinos. For example, the observed oscillation produced in the sun has determined $m_1^2 - m_2^2$ while the observed oscillation of neutrinos produced in the Earth's atmosphere has determined $m_1^2 - m_3^2$. Not only the single values of m_1, m_2 and m_3 remain unknown but also whether m_2 is heavier than m_3 is still not finding an answer. If this *neutrino mass hierarchy problem* would be solved attributing a lighter mass to m_2 compared to m_3, then the mass hierarchy would be considered "normal", otherwise would be considered "inverted".

The understanding of the neutrino mass hierarchy has deep connections in determining if the neutrino is its own antiparticle (Majorana particle), which in turn would shed light on the unsolved mystery about the abundance of particles in the Universe compared to their antiparticles, that were assumed to exist in equal numbers at the beginning.

2.1.1 Beta decay

The β decay is an atomic nucleus radioactive decay generating a beta particle, as an electron or a positron. In particular, the neutron beta decay (or β^- decay) produces a proton by emitting an electron and an electron antineutrino 2.4:

$$n \to p + e^- + \bar{\nu}_e \tag{2.4}$$

As represented in the following Feynman diagram, fig. 2.1, the elementary process involves the conversion of a quark down belonging to the neutron into a quark up belonging to the final proton with the emission of a W$^-$ boson. In turn, the W$^-$ boson decays into the electron and the electron antineutrino.

Similarly, the proton beta decay (or β^+ decay) produces a neutron by emitting a positron and an electron neutrino 2.5:

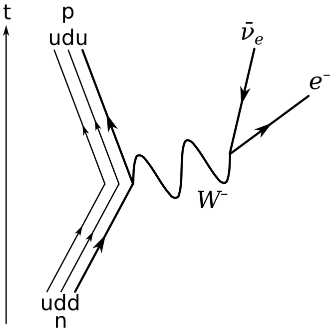

Figure 2.1: β^- decay of a neutron into a proton, electron, and electron antineutrino via an intermediate W$^-$ boson.

$$p \rightarrow n + e^+ + \nu_e \tag{2.5}$$

As above, the Feynman diagram for β^+ decay in fig. 2.2 represents the conversion of a quark up belonging to the proton into a quark down belonging to the neutron by the emission of a W$^+$ boson that decays generating the positron and the electron neutrino.

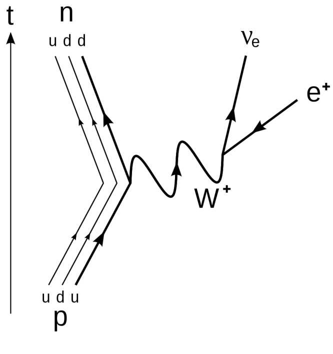

Figure 2.2: β^+ decay of a proton into a neutron, positron, and electron neutrino via an intermediate W$^+$ boson.

2.2 Astrophysical Neutrino Sources

Acceleration mechanism theories (see paragraph 1.2) postulate, in most cases, particles production in distant astrophysical sources.
Strong acceleration environments as shock waves and magnetic clouds are the ideal sites for high energy proton interactions with matter and radiation, with the following generation of pions (*astrophysical beam dump*) whose decay explain the production of high energy neutrinos.
Thus proton-proton (p-p) collisions and photo-hadronic (p-γ) interactions generate positively charged and neutral pions 2.6, 2.7 [26]:

$$p + p \rightarrow \begin{cases} p + n + \pi^{+} \\ p + p + \pi^{0} \end{cases} \tag{2.6}$$

$$p + \gamma \rightarrow \Delta^{+} \begin{cases} n + \pi^{+} \\ p + \pi^{0} \end{cases} \tag{2.7}$$

Neutral pions decay into two γ rays, while positive pions produce neutrinos through leptonic decays 2.8 and the consequent μ^{+} decays in turn according to the 2.9 producing additional neutrinos:

$$\pi^{+} \rightarrow \nu_{\mu} + \mu^{+} \tag{2.8}$$

$$\mu^{+} \rightarrow \bar{\nu}_{\mu} + \nu_{e} + e^{+} \tag{2.9}$$

Similarly to proton, also neutron collision can originate pions (negatively charged) with their production of muons and neutrinos 2.10 and 2.11:

$$\pi^{-} \rightarrow \bar{\nu}_{\mu} + \mu^{-} \tag{2.10}$$

$$\mu^{-} \rightarrow \nu_{\mu} + \bar{\nu}_{e} + e^{-} \tag{2.11}$$

The p-p collisions cross-section is higher (by two orders of magnitude) than the photo-hadronic interactions one, but, regardless of this, one pions production mechanism can dominate on the other according to the peculiar scenario environment of the considered source. Hence, the generation rates of pions are strictly connected to the photon density and the non-relativistic matter density of the source [1].
Taking into account the assumption that both positive and negative charged pions arise equally at the source site, the decays in 2.8, 2.9, 2.10, 2.11 reveal that neutrinos are produced following the flavor ratio $\nu_e : \nu_\mu : \nu_\tau$ = 1 : 2 : 0 even if, due to oscillation phenomena during their propagation from astrophysical sources to the Earth, this ratio becomes 1 : 1 : 1.

As already mentioned in the Chapter 1, shock-accelerated particles (protons and nuclei) that interact with astrophysical sources matter and radiation can produce high energy neutrinos. Hence, in general it is possible to

consider as candidate sources all those capable of baryonic acceleration processes.
The main sources connected to neutrino production are, as for UHECR, Supernovae explosions, Active Galactic Nuclei (AGN) and Gamma Ray Bursts (GRBs).

When a massive star evolution last step corresponds to the collapse of its core into a neutron star or black hole, the star explodes as a **Supernova**. In this framework ν_e are abundantly produced by electron capture processes ($p + e^- \rightarrow n + \nu_e$) that accelerate the star neutronization converting protons into neutrons. With the following emission of neutrinos (and antineutrinos), the binding gravitational energy decreases, bringing the star from the initial hot state to the final cold one [30].
The first neutrino from a Supernova explosion event was detected on the 23rd of February 1987 by Kamiokande II, Irvine-Michigan-Brookhaven and Baksan, fig. 2.3, three underground experiments. After the explosion of the SN 1987A in the Large Magellanic Cloud, twenty-three neutrinos were recorded over a time interval of about 12 seconds. Despite the small number of detected neutrinos, the signal was much higher than the background level: this marked the beginning of *neutrino astronomy*.

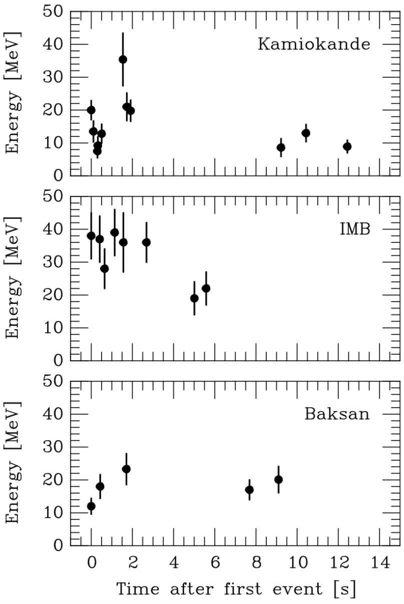

Figure 2.3: From [30]: Neutrino events recorded by the Kamiokande, IMB and Baksan underground experiments. The energies do not refer to the primary ν_e but to the secondary positrons produced by the captures of such neutrinos on protons.

Active Galactic Nuclei (AGN) are very luminous sources, emitting over an energy range that covers more than 20 orders of magnitude, from radio to TeV gamma-rays. The innermost regions of many galaxies host supermassive black holes, with a mass larger than 10^6 $M_\odot$. According to the most widely accepted models, the gas clouds and the matter surrounding the black hole form an accretion disc that emits an extremely high amount of electromagnetic radiation. Under precise conditions, also a relativistic jet is expected to form, which can be observed over astronomical distances.

AGN are typically classified into two main categories, based on their spectral features. Type I AGN have an optical emission spectrum including both narrow and broad lines, while the spectrum of type II AGN is characterised by the presence of narrow lines only. According to an alternative classification, AGN can be divided into two classes: radio-loud (when the emission includes a relativistic jet, dominating at radio wavelengths) and radio-quiet (when any jet-related emission is negligible). In particular, when the relativistic jet is oriented towards the observer's line of sight, the AGN is called **blazar**.

Radio-loud AGN are among the principal candidate sources of high energy astrophysical neutrinos. The interaction of the protons and neutrons of the relativistic jets with the surrounding matter and radiation is expected to produce high energy pions, from whose decay chain (2.8, 2.9, 2.10, 2.11) a production of TeV gamma rays and neutrinos is foreseen. This model opens the possibility of a multi-messenger observation of AGN, including gravitational waves.

The IceCube neutrino telescope has developed a dedicated AGN trigger, that can provide a real-time alert to other observatories and trigger simultaneous observations in a wide range of the electromagnetic spectrum. One of these public alerts, released on the 22nd of September 2017, ended up with the birth of multi-messenger astrophysics. IceCube and the Fermi Large Area Telescope observed a simultaneous emission of neutrinos and gamma rays (respectively) from the TXS 0506-056 blazar, with a 3 σ confidence level. The emission of blazars is characterized by a typical time variability that ranges over a timescale from few days to several years. Interestingly, the analysis of archival data evidenced that a neutrino signal had already been detected by IceCube from the same direction in 2014-2015. This demonstrates that TXS 0506-056 was an active neutrino source already for several years [31] [3].

Gamma Ray Bursts (GRBs) are the brightest cataclysmic events in the Universe, with typically released energies that can reach values up to 10^{54} erg. Given the extreme variability and diversity of the emitted light curves, the classification of GRBs is conventionally based on the duration of the burst. More precisely on the T90 parameter, that is the time over which the GRB releases from the 5% to the 95% of its total energy. This time can be as short as few milliseconds or last up to several minutes: a GRB is defined as "short" if the burst duration is lower than two seconds and "long" if the T90 is higher. In many cases, the prompt emission occurring during the explosion is followed by an afterglow phase that can last several months.

According to the most widely accepted models, GRBs can be originated by the collapse of massive stars or by the merger of binary systems, resulting in two collimate, oppositely directed jets. The so-called fireball model of the relativistic jets describes the mass emission from the GRB central engine in the form of successive plasma shells at different speeds. The interaction of the internal shock fronts is expected to accelerate electrons

and protons to energies up to 10^{21} eV.
An intense neutrino production is expected by the interaction of such high energy protons with the surrounding matter and radiation both during the explosion phase and during the afterglow [32].

2.2.1 Cosmic neutrino background CνB

The cosmic neutrino background (CNB or CνB) is the Universe's background particle radiation composed of neutrinos, also known as *relic neutrinos*.
The Big Bang cosmology predicts the existence of a relic sea of neutrinos. Three cosmic backgrounds are foreseen: the Cosmic Microwave Background (CMB), originated 380000 years after the Big Bang, the Cosmic Neutrino Background, which decoupled about one second after the Big Bang, and the Cosmic Gravitational Wave Background, created by the inflationary expansion decoupled directly after the Big Bang.
Early cosmic neutrinos were in equilibrium by frequent weak interactions with other particles. Anyway, as the temperature of the Universe reached the order of 2-5 MeV, these interactions became ineffective and the process of neutrino decoupling took place [33].
As neutrinos rarely interact with matter, these neutrinos still exist today. But since they have extremely low energies, around 10^{-4} to 10^{-6} eV, it is almost impossible to observe them with current technologies. Nevertheless they represent a huge opportunity to probe the early stages of the Universe, therefore several detection methods are under investigation, including the induced beta decay ($\nu_e +^3 H \rightarrow^3 He + e^-$) that seems to be the most promising [34] [35] [36].

2.2.2 Solar neutrinos

The greatest amount of neutrinos observed on the Earth is represented by neutrinos coming from the Sun.
Among nuclear fusion reactions occurring in the Sun's core that are responsible for neutrino production, the greatest contribution comes from the proton-proton reaction 2.12:

$$p + p \rightarrow d + e^+ + \nu_e \tag{2.12}$$

The detection of solar neutrinos started in 1968. Since the earliest results, a large discrepancy between the observed flux and the predicted one was revealed. This discrepancy is known as the "Solar Neutrino Problem", later explained by oscillation phenomena.
The Sun produces only electron neutrinos, whose number can be predicted by the Standard Solar Model. When detectors on the Earth became sensitive enough to measure the flux of ν_e from the Sun, the number observed was only 1/3 of the predicted one. The mechanism proposed by Bruno Pontecorvo in 1957 (see paragraph 2.1) can explain this discrepancy: if

the neutrinos produced in the Sun are not massless particles, but a combination of mass eigenstates in different proportions, a ν_e can change its flavor during its propagation from the Sun to the Earth.

2.2.3 Atmospheric neutrinos

When cosmic rays enter the Earth's atmosphere, interact with its nuclei.
These high-energy nuclear interactions produce many pions and kaons that, since are unstable, decay to other particles according to the processes already mentioned in 2.8, 2.9, 2.10 and 2.11. In this way a shower of neutrinos is produced: we refer to these neutrinos as *atmospheric neutrinos*.
Atmospheric neutrinos and their companion muons represent one of the largest background sources for neutrino detectors (they can be treated as quasi-aligned given the typical granularity of optical modules in a neutrino telescope).
For example, the IceCube experiment (as the other neutrino detectors, see paragraph 2.4) undergoes to atmospheric neutrinos background from both Earth's hemispheres.
On one side, the Earth acts like a filter to suppress the background of atmospheric muons coming from the northern hemisphere (in an up-going direction for the detector). The atmospheric muon background from the southern hemisphere registered by the detector (down-going direction) is more important since the only ice layer is not thick enough to act as an absorber.
For this reason, there is the need to prevent that downward-going atmospheric muons are misidentified as muons induced by neutrino interactions. A basic strategy is to identify only neutrino-induced upward or horizontal muons.
In this way, the field of view of a neutrino telescope is limited only to the opposite hemisphere with respect to the geographical position of the detector.
To open the field of view of large neutrino telescopes also to the hemisphere above the detector and discriminate between extra-terrestrial neutrinos and the background of atmospheric muons/neutrinos, there is the possibility to use part of the instrumented volume as an active veto for atmospheric down-going events. For example, if a down-going ν_μ event starts inside a *fiducial* volume of the detector and cannot be detected any companion muon (from the same direction) in the outer *veto* region, then the detected ν_μ has an extra-terrestrial origin [37].

2.2.4 Cosmogenic neutrinos

At ultra-high energies, neutrinos are produced by the interaction of high energy cosmic particles with cosmic microwave background (CMB) photons. After generating a Δ^+ resonance, there are two possible channels of decay, equ. 2.13:

$$\begin{aligned} p + \gamma_{CMB} \rightarrow \Delta^+ \rightarrow\ & n + \pi^+ \\ & p + \pi^0 \end{aligned} \tag{2.13}$$

The channel that produces the charged pion π^+ is responsible for the ultra-high energy neutrinos production.

2.2.5 Neutrino Flux

Because of the wide range of energies and the very different types of sources and detectors, it is difficult to keep up with every development of the entire field of neutrino astronomy.
A graphical representation that gives an overview in one single plot of the neutrino and antineutrino flux at the Earth, from the low energies of the CνB in the meV range to the highest PeV energies of cosmic neutrinos, is given by the *Grand Unified Neutrino Spectrum* (GUNS) in fig. 2.4. In the GUNS plot are shown the neutrinos from the CνB, the decay of neutrons and tritium during big-bang nucleosynthesis (BBN), solar neutrinos, geoneutrinos[3], reactor neutrinos, diffuse supernovae neutrino background (DSNB), atmospheric neutrinos, high-energy astrophysical neutrino flux as measured by IceCube, and cosmogenic neutrinos.

2.3 Neutrino Detection Principles

As described in paragraph 2.1, neutrinos interact only through *weak interaction* and, for this reason, the detection processes that can be used are limited and usually indirect. The attention is focused on the output charged leptons since they follow the initial neutrino direction.

A very diffuse detection technique is based on the observation of Cherenkov radiation emitted by secondary leptons (produced after neutrino interaction) while travelling in a scintillator medium, described in detail in paragraph 2.3.1.
The idea of building a *neutrino telescope* using a matrix of light detectors inside a transparent medium was firstly developed by Markov [27]. The medium should be deep ice or water as they can offer a large volume of free target for neutrino interaction, allow ideal transmission of the Cherenkov

---

[3] Geoneutrinos are primarily ν_e produced in decays of radioactive elements with lifetime comparable to the age of the Earth. They provide indirect information on plate tectonics, mantle convection, magnetic-field generation, as well as the processes that led to the Earth formation.

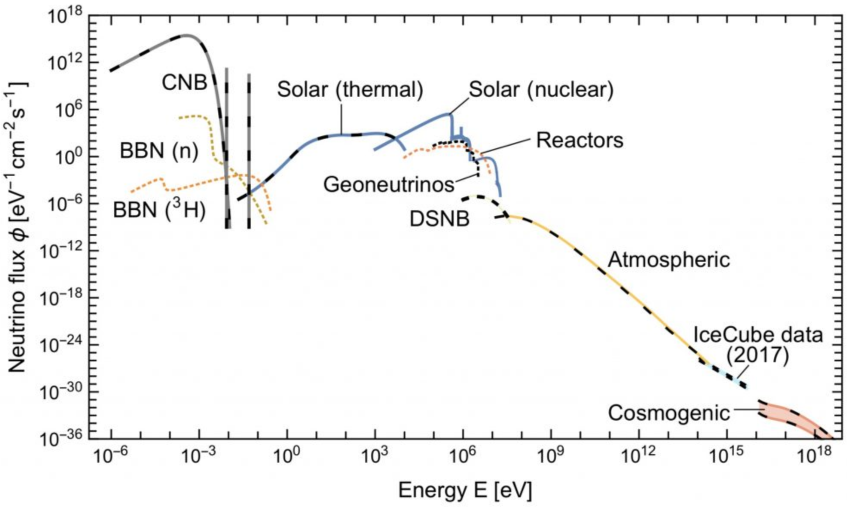

Figure 2.4: From [38]: Grand Unified Neutrino Spectrum (GUNS) at Earth, integrated over directions and summed over flavors. Solid lines are for neutrinos, dashed or dotted lines for antineutrinos. Here are shown the neutrinos from the CνB, the decay of neutrons and tritium during big-bang nucleosynthesis (BBN), solar neutrinos, geoneutrinos, reactor neutrinos, diffuse supernovae neutrino background (DSNB), atmospheric neutrinos, high-energy astrophysical neutrino flux as measured by IceCube, and cosmogenic neutrinos.

light and shield the secondary particles produced by cosmic rays interacting with the atmosphere [26].

When a high-energy neutrino impacts the Earth, it interacts with a nucleon (proton or neutron) of an atomic nucleus. In the *charged-current* (CC) weak interaction, the interaction is mediated by the W$^{\pm}$ boson, with the consequent creation of a charged particle. The *neutral-current* (NC) weak interaction is mediated by the Z^0 boson, with the consequent creation of a neutrino. The Feynmann diagrams of these reactions are represented in fig. 2.5 and described by the equation 2.14:

$$\begin{aligned} CC &: \nu_l(\bar{\nu}_l) + N \rightarrow l(\bar{l}) + X \\ NC &: \nu_l(\bar{\nu}_l) + N \rightarrow \nu_l(\bar{l}) + X \end{aligned} \tag{2.14}$$

where *l* is the neutrino flavor and the corresponding produced lepton, while *X* is the hadronic remnant after the nucleon interaction [32].

Charged current interactions cross sections are greater than neutral current ones, thus making CC processes probability higher. Their respective signatures in a detector are different. The neutrinos that interact via NC process create hadronic showers independently of their flavor, while the signatures of those that interact via CC process depend on the generated lepton flavor.

For example, an electron neutrino interaction generates an electromagnetic shower, usually too compact to be resolved in a large detector that,

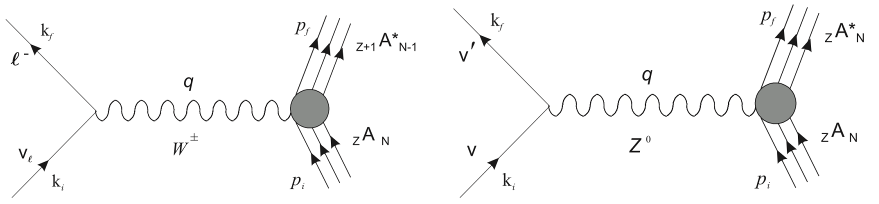

Figure 2.5: From [39]: Feynman-diagrams of lowest order for: (left) the CC neutrino-nucleus reaction and (right) the NC neutrino-nucleus process. The diagrams corresponding to the antineutrino reactions, are similar.

hence, sees it as a spherical-shaped deposit of energy [9].

A high-energetic muon neutrino interaction produces a hadronic shower and a muon, that travels over long distances before decaying. In this case, the signature is a track-like event, since the high energy muon generates a cone of Cherenkov light while travelling in the medium.

Tau neutrino has two possibilities of event signatures. For energies lower than 1 PeV, the immediate decay of the τ produced right after the interaction generates a shower-like event. For energies higher than 1 PeV, after the hadronic shower, the τ travels for a long distance before decaying and producing a second hadronic shower and a second neutrino: this kind of events is called *double bang*. A representation of the different signatures of neutrinos interactions are shown in fig. 2.6.

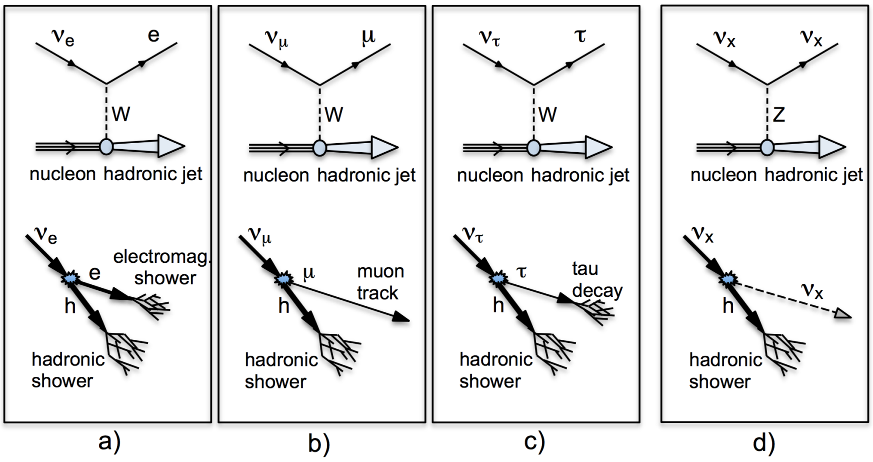

Figure 2.6: From [40]: Different types of neutrino interactions with matter. **Top**: interaction diagrams. **Bottom**: event signatures. **a)** CC interaction of a ν_e produces both an electromagnetic shower and an hadronic shower; **b)** CC interaction of a ν_μ produces a muon and an hadronic shower; **c)** CC interaction of a ν_τ produces an hadronic shower and a τ that, in turn, produce a second shower and decays into a ν_τ; **d)** NC interaction (all neutrino flavors) produces an hadronic shower. Particles and antiparticles cannot be distinguished in a neutrino telescope.

2.3.1 The Cherenkov Effect

Secondary leptons, produced after neutrino interactions, generate Cherenkov light while travelling in a transparent medium. This light is then detected by optical modules equipped usually with PMTs. The information provided by the number of detected photons and their arrival times is used for the neutrino flavor, direction and energy reconstruction [26].

According to the Theory of Relativity, no particle can travel faster than the light in vacuum ($\sim 3 \cdot 10^8$ m/s).
Since the speed of light in a medium is lower than in vacuum, a charged particle can travel faster than the phase velocity[4] of the light in that medium. Hence, the charged particle along its path polarizes the atoms or molecules of the medium that, when returning in their initial configuration, emit electromagnetic radiation: this radiation is called *Cherenkov light*.
The radiation is emitted in a cone with a characteristic angle θ_C represented in fig. 2.7 and following the equation 2.15:

$$cos\theta_C = \frac{c/n}{\beta c} = \frac{1}{\beta n} \tag{2.15}$$

where n is the refractive index of the medium and $\beta = v_{particle}/c$ is the velocity of the charged particle with respect to the speed of light in vacuum. For relativistic particles in seawater, when $\beta \sim 1$ and $n \sim 1.364$, the Cherenkov angle is equal to $\theta_C \sim 43^\circ$ [26]. The spectral distribution of Cherenkov emission in terms of number of photons N_γ emitted per wavelength $d\lambda$ and per travelled distance dx by a particle with charge $\pm Ze$, is expressed in relation

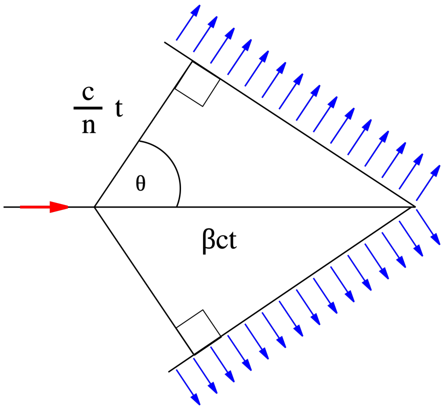

Figure 2.7: The geometry of the Cherenkov radiation. In the figure, v is the velocity of the particle (red arrow). The blue arrows shows the direction of the radiation. Credits to Arpad Horvath.

---

[4] Speed of propagation of a wave in a medium.

of the emitted wavelength as in the 2.16:

$$\frac{dN^2}{dxd\lambda} = \frac{2\pi Z^2\alpha}{137\lambda^2}(1 - \frac{1}{n^2\beta^2}) \tag{2.16}$$

where α is the fine structure constant.
Thus for shorter wavelengths, the Cherenkov radiation is more intense.

The best fit for PMT specifications in an underwater neutrino telescope is determined by the combination of few crucial requirements. More precisely, the wavelength range of highest photon detection efficiency must match with the maximum of the Cherenkov emission spectrum, minimize the cut-off effect introduced by the glass sphere and correspond to the region of highest water transparency (longest attenuation length around $\sim$420 nm, as described in paragraph 5.1.1). For these reasons, the most widely adopted PMTs in neutrino telescope applications have a bialkali photocathode on a borosilicate window, with a typical detection efficiency ranging between 300-600 nm and maximum efficiency at about 400nm.

2.4 Neutrino Telescopes

The task for a Neutrino Telescope is to detect neutrinos determining their direction and energy.
Differently from an astronomical telescope that collects light arriving from a specific direction of the sky and directs it with mirrors, a neutrino telescope cannot exploit a similar mechanism for neutrinos detection. Thus the only possible strategy is to observe single neutrinos and determine their direction and energy through the detection of the energy of secondary particles produced in the neutrino interaction (as described in paragraph 2.3).
The low probability of neutrino interaction with matter implies the need for a large detector mass: 10^6 tons of target mass for the detection of GeV energy neutrinos and 10^9 tons for the detection in the TeV region. For this reason, a target medium in its natural environment, as ocean water or ice, must be instrumented. To instrument such a high volume of ice or water, the adopted detectors must be simple and cost-efficient. The optical modules used are equipped with photomultiplier tubes and tested to withstand high pressure, distributed according to a specific geometry to form the detector.

The fundamental parameters that describe the performances of a neutrino telescope are the *effective area* and the *angular resolution*. Such quantities are peculiar to each telescope since they are highly technology-dependent. Moreover, they act as a reference when one needs to correlate the sensitivity of each of them.
The *effective area* is defined as the surface of the detector on which 100%

of crossing neutrinos would be detected.
It is expressed as in 2.17:

$$A_{\nu}^{eff}(E_{\nu}) = P_{\nu\mu}(E_{\nu}, E_{thr}^{\mu}) \cdot A \cdot e^{-\sigma(E_{\nu})\rho N_A Z(\theta)} \tag{2.17}$$

where $P_{\nu\mu}(E_{\nu}, E_{thr}^{\mu})$ is the probability that a neutrino with energy E_{ν} produces a muon with energy E^{μ} that survives with energy E_{thr}^{μ} after the propagation from the interaction point to the detector, A is the surface surrounding the instrumented volume, $\sigma(E_{\nu})$ is the neutrino cross section, ρN_A is the target nucleon density (N_A is the Avogadro number) and $Z(\theta)$ is the distance traveled by the neutrino though di Earth coming from the direction θ with respect to the nadir.
As a consequence, for a defined neutrino flux $\frac{d\Phi_{\nu}}{dE_{\nu}}$, the number of detected neutrinos events is given by the following 2.18:

$$\frac{N_{\mu}}{T} = \int \frac{d\Phi_{\nu}}{dE_{\nu}} A_{\nu}^{eff}(E_{\nu}) dE \tag{2.18}$$

where T is the observation time (for example, the event rate in a neutrino telescope as big as the IceCube experiment is N($E_{\mu} \geq 1$ TeV) $\sim$ 2.8 yr^{-1}).
Another quantity that characterises a neutrino telescope is the *effective volume*. It corresponds to the product between the detector effective area and the muon range R$_{\mu}$, defined as the distance travelled by the muon produced after ν_{μ} CC interaction (to give an estimation, a 1 TeV muon has an R$_{\mu}$ in the water of 2.42 km). The effective volume is larger than the instrumented volume and increases with increasing neutrino energy.
The *angular resolution* of the telescope is defined mainly by two factors: one is the angle between the neutrino and the generated secondary particles at the interaction point, the other is the quality of energy and direction reconstruction of these latter.
Both factors depend on the energy of the particles. The angular resolution improves with increasing energy. It can reach the order of a fraction of degree only for ν_{mu} CC interactions because of their track-like signature in the detector. For the other flavors and NC interactions, due to their approximately spherical signature, the angular resolution is inadequate for a proper direction reconstruction. For example, the IceCube detector can reconstruct shower-like events with a median angular resolution of 10°-15°. On the other side,x muon neutrinos tracks above 1 TeV can be reconstructed within 1° [41].
The muon neutrino events are detectable even if the muon is generated outside the detector thanks to the long track produced, and this effect provides a larger *effective area* for muon neutrinos. But, as already mentioned, muons represent one of the principal sources of background, since they can reach the detector and mimic neutrino events. One of the techniques to reduce such background consists in the identification of up-going muons, that can be associated with neutrinos that traversed the Earth.
Differently from other telescopes, neutrino telescopes are "downward-looking",

i.e. they cover mainly the hemisphere below the detector. For example, the IceCube experiment at the South Pole observes neutrinos coming from the northern hemisphere while the ANTARES experiment observes those from the southern hemisphere. In this way, the advantage is that different telescopes in different places of the Earth look at complementary portions of the sky.
Another strategy to suppress this kind of background is to identify the *starting events*, defined as those events whose neutrino interaction vertex inside the detector volume. In this way, atmospheric muons can be efficiently rejected.
At this scope, from the angular resolution and the effective area, can be defined the *sensitivity* of the telescope as the ability, given a specific neutrino flux, to discriminate the signal from the background and identify neutrino point sources.

The above discussion followed mainly the approach used in [26] and [40].

2.4.1 Water and ice

The largest natural environment mediums are ocean waters and Antarctic ice.
To describe their features, two experiments, one in the water and the other in the ice, are compared: ANTARES and IceCube (for details see paragraphs 2.4.3 and 2.4.2).

Water and ice show small differences, since water has slightly higher electron density and a higher refractive index: for example at 400 nm wavelength n$_{water}$ ~1.36 while n$_{ice}$ ~1.32 and this influences also the respectively Cherenkov emission angles ($\theta_{water} \sim 42^{\circ}$ and $\theta_{ice} \sim 41^{\circ}$) [40].
Also, the propagation of light in water (developed in details in paragraph 5.1.1) has different features compared to the ice one. In particular, the *absorption length* and the *scattering length* (respectively the propagation path of photons before being absorbed/scattered by 1/e factor) for the water of the ANTARES experiment, for example, are equal to 55 m and 265 m for a wavelength of 470nm and are constant all over the detector. For the IceCube experiment, instead, these parameters are quite different (of the order of 100 m for the absorption length and 30 m for the scattering one) as the scattering phenomenon is predominant and change consistently with the densities of the different layers of the ice [40]. In the figure 2.8 is shown the variation of the absorption length with depth for a 400 nm wavelength.
The strong ice inhomogeneity can influence the reconstruction of neutrino direction and energy. For this reason, the optical ice properties are constantly measured by the IceCube collaboration to improve their knowledge.
Nevertheless, in ANTARES fewer photons propagate for long distances. Com-

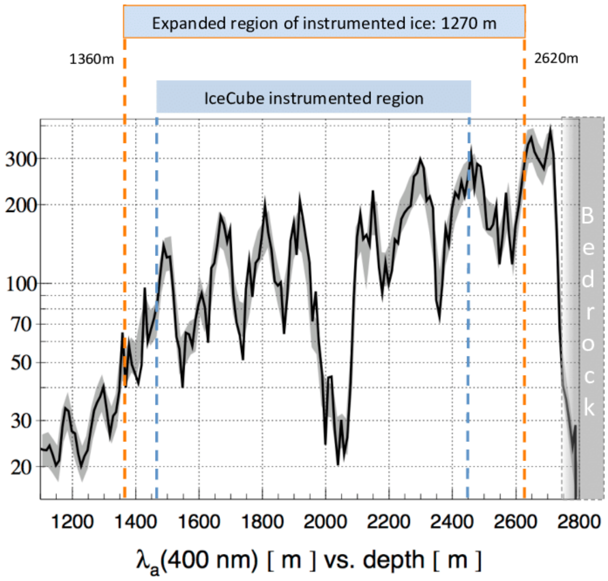

Figure 2.8: From [42]: Absorption length in the glacial ice versus depth. The layer of high dust concentration starts at about 2000 m depth. The ice above and below that layer is very clear. In the plot are indicated the current instrumented depth range and the future upgrade.

pared to IceCube, they travel almost unscattered and bring with them the information of the direction of neutrino interaction process.
Another difference between water and ice is the environmental background: a PMT from IceCube registers low noise rates (of the order of 1 kHz) while an ANTARES PMT registers a minimum of 40 kHz up to hundreds of kHz of noise [40]. This difference is due to the presence in the seawater of ^{40}K constant radioactive decays and the additional bioluminescence from deep-sea organisms (see paragraphs 5.1.4 and 5.1.5 for details).

The existing neutrino telescopes that use water as a scintillator medium are ANTARES, GVD-Baikal and KM3NeT, while the only telescope built in the ice is IceCube. They will be thoroughly described in the following paragraphs.

2.4.2 IceCube

Icecube is the largest and most advanced neutrino telescope worldwide. It is located at the Amundsen-Scott south pole station, deployed at a depth between 1450 m and 2450 m. The detector consists of a cubic kilometre of ultra-clean antarctic ice instrumented with 5160 Digital Optical Modules (DOMs), distributed over an array of 86 strings frozen into boreholes.
The installation is arranged over a hexagonal grid, as represented in fig.

2.9. The average inter-string distance is about 125 m, while the DOMs are spaced at 17 m.

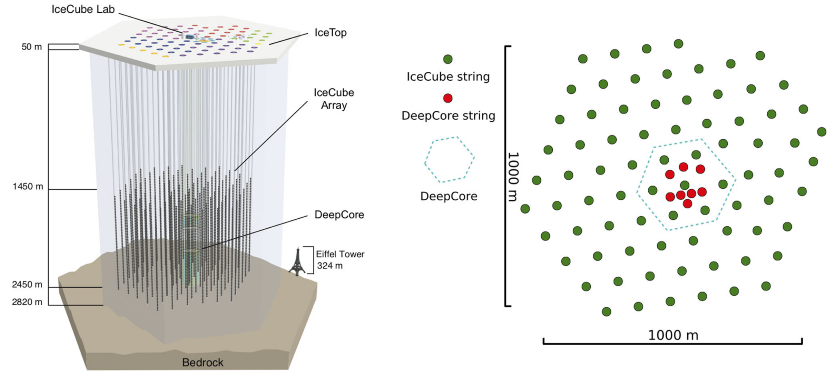

Figure 2.9: From [43]: Sketch of the IceCube observatory. The right plot shows the surface footprint of IceCube. The green circles represent the standard IceCube strings, separated by 125 m, and the red ones the more densely instrumented strings with high quantum efficiency photomultiplier tubes. Strings belonging to the DeepCore sub-array are enclosed by the dashed line.

The neutrino energy threshold corresponding to such geometrical configuration is about 100 GeV.
An additional group of 8 units has been deployed at the centre of the array, with a denser spacing among strings and a closer distance between consecutive DOMs. With the surrounding layer of "standard" strings, such a group of units constitutes the so-called "IceCube Deep core", a high sensitivity inner region with an energy threshold of 10 GeV. The telescope layout is completed by a surface array, called "IceTop", developed for calibration and background rejection purposes. IceTop is arranged over 81 stations, for a total of 162 ice tanks, each equipped with two DOMs, acting as a veto for downing atmospheric events.
The IceCube optical sensor, the DOM, consists of a 17" high-transparency glass sphere containing a 10" photomultiplier tube and electronics boards for signal readout, power distribution and additional calibration purposes. The PMT waveform, triggered on a single photoelectron level, is digitized and time-stamped with nanosecond accuracy. Data from all DOMs are synchronised and sent to the computer centre of the IceCube Laboratory through surface cables.
The IceCube detector is running in its final configuration since the end of 2010. The first important result dates back to 2013 [41], with the observation of an extraterrestrial diffuse flux of high-energy neutrinos above 100 TeV. Its origin is expected to be extra-galactic, but no potential source has been identified, keeping many questions still open. A few years later, on the 22nd of September 2017 [3], the IceCube Collaboration announced a discovery that still today represents one of the principal milestones of multi-messenger astroparticle physics. For the first time in history, an ex-

tremely high energy neutrino event (290 TeV) has been observed in spatial coincidence with a known gamma-ray blazar named TXS 0506+056 (γ-rays detection within 0.1 degrees from the direction of the neutrino event), with a statistical significance at the level of 3 standard deviations. The blazar is located 5.7 billion light-years away in the direction of the constellation Orion, at a measured redshift of 0.34. An extensive measurement campaign at x-ray, optical, and radio wavelengths has been performed, providing an enormous amount of information and setting constraints for the muon-neutrino luminosity of this source.

2.4.3 ANTARES

ANTARES (Astronomy with a Neutrino Telescope and Abyss environmental RESearch) is currently the largest operating neutrino telescope in the Northern hemisphere since KM3NeT is still under construction (see paragraph 2.4.5 for details).
It is located in the Mediterranean Sea, 40 km offshore Toulon (France), at about 2500 m depth. ANTARES consists of 12 strings of 450 m length, spaced about 70 m from each other, coupled to a junction box that connects them to the station located on the shore via an electro-optical cable. Every string hosts 25 storeys equipped with three optical modules containing a 10" PMT [44]. ANTARES PMTs look downward with the axis of the photocatode at 45° with respect to the vertical, thus maximising the capabilities of detecting up-going tracks, see fig. 2.10.
The deployment of the first five strings took place in 2007, while the configuration of 12 strings was finalised in 2008.

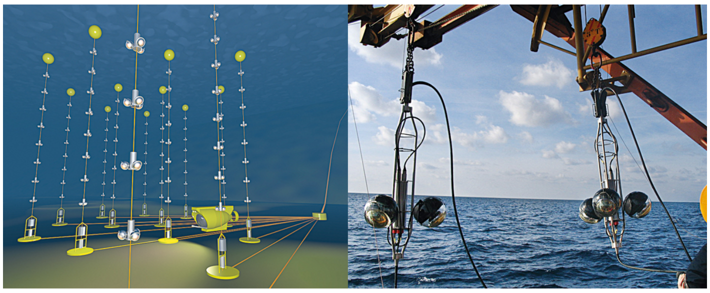

Figure 2.10: **Left**: Artistic rendering of the ANTARES telescope. **Right**: Picture of two storeys, each one equipped with three optical modules.

The ANTARES detection energy ranges from 10 GeV to 100 TeV, with a field of view complementary to the IceCube one. Since in the water the light undergoes a low scattering process, the result is better resolving power. On the other side, the water provides more background sources as potassium decay and bioluminescence, thus leading to different background-suppression methods.

2.4.4 Baikal - GVD

The Gigaton Volume Detector (GVD) is the neutrino telescope situated in one of the largest lakes in the world, Lake Baikal (Russia). It has a modular structure consisting of several sub-arrays (clusters) deployed at 1 km depth, at about 4 km from the shore.

During the preliminary phase of the experiment, in 2015, it was deployed a demonstration *cluster*, with 192 optical modules. The first phase of construction started in 2016 with the deployment of the first of the eight clusters, consisting of 288 optical modules (hosting a 10" PMT, similar to IceCube) distributed in 8 strings (with a vertical distance between optical modules of 15 m). The inter-string space is 60 m, while the distance between the clusters is around 300 m. Between 2015 and 2020, seven clusters were installed, making GVD the largest neutrino telescope in the Northern hemisphere. By design, the Baikal-GVD telescope is the most sensitive to the upward or nearly horizontal neutrinos, in the energy range between about 0.1 TeV and 100 PeV [45]. In fig. 2.11 is shown a schematic drawing of a single Baikal-GVD cluster with seven strings along a circle and one central string, and the layout of seven Baikal-GVD clusters already deployed during the 2015-2020 years. The final configuration of the telescope is planned by the end of 2021, with an instrumented effective volume of around 1.5 km^3.

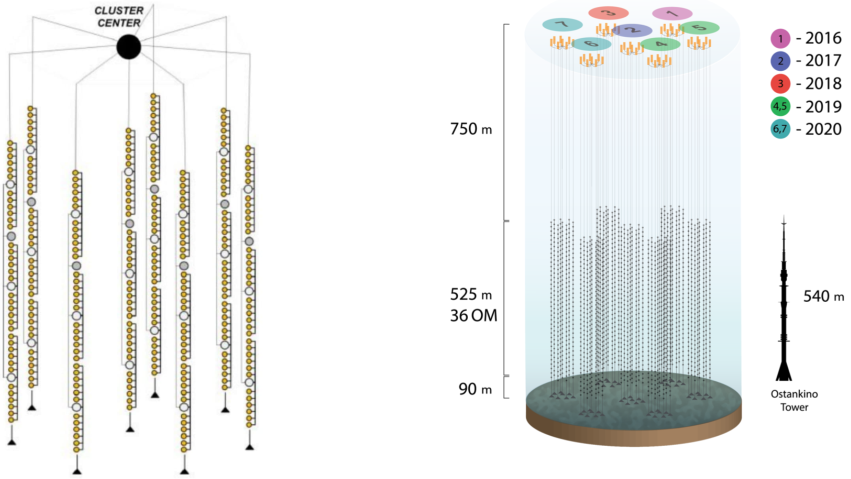

Figure 2.11: From [45]: **Left**: A schematic view of a single Baikal-GVD cluster with seven strings along a circle and one central string. Solid circles correspond to optical modules (OMs). Open circles illustrate electronics modules of a section (CMs). **Right**: A schematic view of seven Baikal-GVD clusters installed in the period 2015-2020.

Each cluster can be considered an independent detector. Therefore, such a structure allows adding new clusters without reconfiguring the whole

telescope.
During the Winter period, the ice layer covers the entire lake, with a thickness reaching about 40-50 cm. This is sufficient for transportation of heavy equipment and smooth deployment operations (the positioning of the string is performed directly through drilled holes).

Acknowledgements go to the GVD collaboration that helped the TUM team during the feasibility study of the first prototype of the POCAM, deploying it at 1100 m of depth, during Winter 2017, coupled to one of their string. It stably took data for one year before being recovered, confirming its proof of concept (see paragraph 3.3).

2.4.5 KM3NeT

KM3NeT is the last generation underwater neutrino telescope under construction in the Mediterranean Sea. The detector is distributed over two installations, sharing the same technologies but arranged in different layouts, to cover complementary ranges of energy and consequently address various science topics.
ARCA (Astroparticle Research with Cosmics in the Abyss) is located in Italy about 100 km offshore Portopalo di Capopassero and will identify and study the sources of high-energy cosmic neutrinos in the range from 100 GeV to 10^8 GeV [46].
The second installation ORCA (Oscillation Research with Cosmics in the Abyss) has a more compact detection volume and higher granularity, optimised in a lower energy range (few GeV to 100 GeV [46]) for neutrino oscillation studies. The installation site is located 10 km away from the ANTARES neutrino telescope, 40 km offshore the coast of Toulon (France).
An representation of the future detector is shown in fig. 2.12.

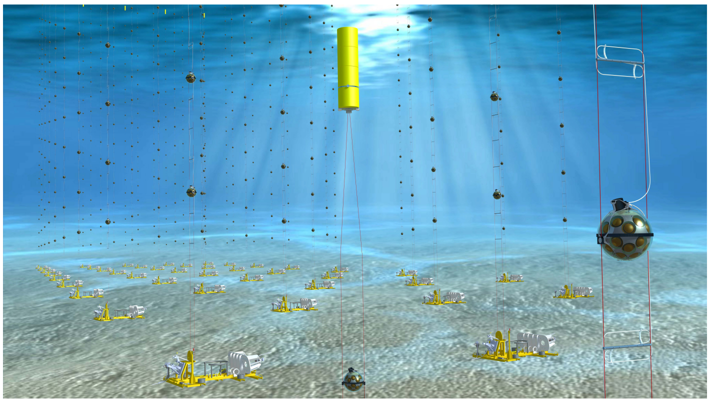

Figure 2.12: From *KM3net.org*: Representation of many Detection Units in the KM3NeT telescope.They are anchored to the seabed of the Mediterranean and stretched out in water by the yellow buoys.

The scientific goal of KM3NeT is to pick up the baton form ANTARES and achieve a complementary sky coverage with respect to IceCube, with a comparable detection volume and an improved reconstruction accuracy.
KM3NeT aims at revolutionising the standard detection strategy of previous neutrino telescopes with the implementation of the so-called "multi-PMT" Digital Optical Module (DOM) design, consisting of a 17" borosilicate glass sphere hosting 31 small size (3 inches diameter) PMTs, shown in fig.2.13.
Compared to the design of the optical modules of IceCube and ANTARES, the KM3NeT DOM has a larger overall photocathode area and single-photon counting capabilities, allowing a more accurate Cherenkov light direction and energy reconstruction. Groups of 18 DOMs are arranged in vertical structures called "Detection Units" (DUs), with different spacings for ARCA and ORCA. Moreover, the DUs of both installations have different lengths: the length of an ARCA DU is 630 m while that of an ORCA DU is 170 m.
In their final layout, ARCA will consist of 230 DUs and ORCA of 115, for a total instrumented volume of seawater of one gigaton and few megatons, respectively. Both detectors are currently under construction and have already been deployed 6 DUs for each of them, with a combined effective area that is already comparable to that of ANTARES. In the next few years, the deployment of additional tens of DUs is scheduled.


Figure 2.13: KM3NeT digital optical module with 31 PMTs.

2.5 P-ONE: Pacific Ocean Neutrino Experiment

The IceCube discovery of the isotropic signal of an astrophysical flux of neutrinos at the TeV-PeV scale in 2013 [41] and the discovery of neutrino emission from the TXS0506+056 blazar in 2017 [3] have shed light even more on the need of particularly improving the exposure to high energy astrophysical neutrinos [47].
Thus, to significantly detect more astrophysical neutrinos, two approaches in principle should be followed: one is to increase the size of already existing telescopes by several orders of magnitude, the other one is building new telescopes.
In this framework, the idea of building a new underwater neutrino telescope originated after fruitful discussions between different research groups

from Canada, the USA and Germany and the Pacific Ocean Neutrino Experiment (P-ONE) was born.
The main goal is to build a large volume neutrino telescope exploiting the already existing Ocean Networks Canada's (ONC) cabled large subsea infrastructure offshore Vancouver Island.
ONC has several underwater installations, among which the two large oceanographic observatories are situated in the North East Pacific Ocean: one is NEPTUNE, the other is VENUS. The first one has five powered nodes distributed alongside the Juan de Fuca tectonic plate. The node located in Cascadia Basin has been chosen for P-ONE.
Cascadia Basin is a heavily sedimented abyssal plain region located at 2660 m depth (water temperature $\sim 2^{\circ}$) about 200 km off Vancouver Island and represents the ideal candidate site, see fig. 2.14.
P-ONE will be built for detecting neutrinos in the energy range of TeV-PeV.

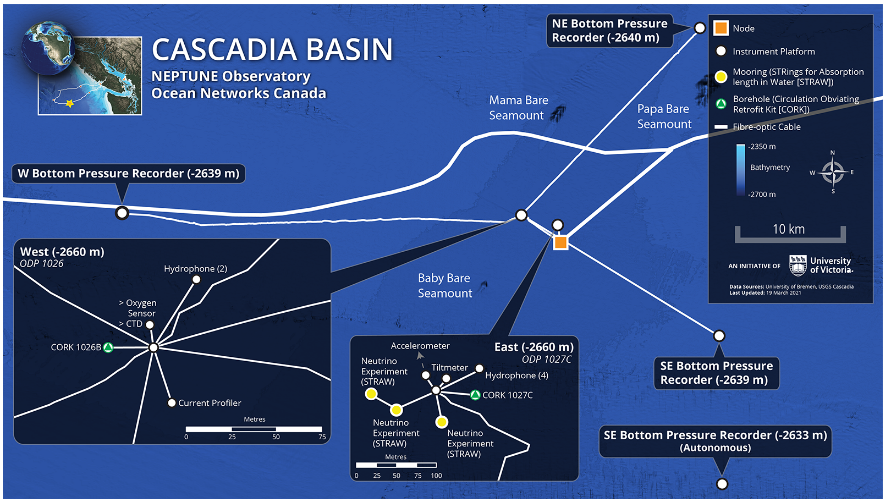

Figure 2.14: Map of Cascadia Basin. In the instrument platform next to the node are connected the three pathfinder strings of STRAW and STRAW-b projects. Picture courtesy of Ocean Networks Canada, $https://www.oceannetworks.ca/observatories/pacific/cascadia-basin$.

The deployment is planned to start in 2023, with the first segment of 10 strings named *Explorer*.
A typical attenuation length ranging between 20-70 m would require thousands of photosensors distributed all over the detector volume. Targeting primarily horizontal high energy muons, induced by very high-energy neutrinos, leads to a *segmented* neutrino telescope design exploiting the fact that such muons travel for several kilometres in the water. The Cherenkov light produced can provide sufficient information for the energy/direction reconstruction with an angular resolution of a fraction of a degree [47]. In the fig. 2.15 is represented a scheme of the entire detector: for each string are planned 20 optical modules and 2 calibration modules, for a total of 70

strings to be deployed in 2028-2030.

The first steps towards P-ONE have been focused on the feasibility studies

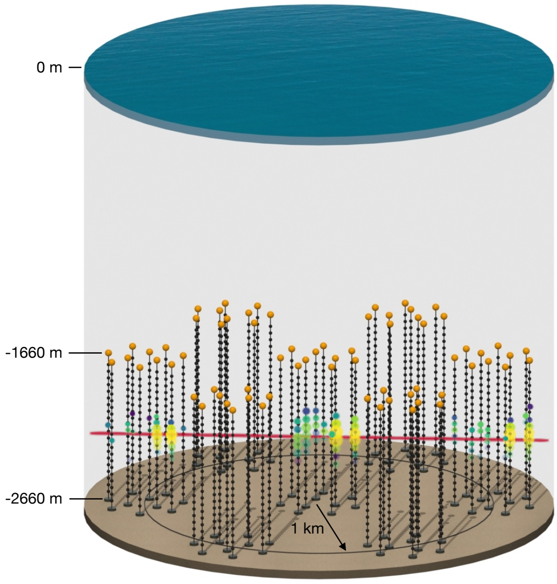

Figure 2.15: Sketch of P-ONE geometry: seven segments of 10 strings each, optimized for energies 10 TeV-10 PeV. Moreover is represented the track produced by a 50 TeV horizontal neutrino.

aiming at the characterisation of the Cascadia Basin site optical properties and the long term monitoring of the light background.

The two pathfinder missions named STRAW (STRing for Absorption length in Water) and STRAW-b have been deployed respectively in spring 2018 and summer 2020.

STRAW is taking data continuously with a duty cycle of 98%, providing the first preliminary in-situ measure of the attenuation length at different wavelengths (details in paragraph 5.1.2). The long term monitoring of almost two years didn't show any peculiar increased environmental background period (details in paragraph 5).

STRAW-b is currently under a fine-tuning process of data acquisition by TUM and ONC teams. In the meanwhile, P-ONE members are finalising the design for the following Explorer array.

STRAW and STRAW-b experiments as feasibility studies for P-ONE have been the main object of this thesis.

> “ *In oltre, non chiamate voi una stella fissa, piccolissima, dico anco delle più apparenti, non che di quelle che fuggono la nostra vista? e le chiamiamo cosí in comparizione dello spazio circonfuso. Ora, quando tutta la sfera stellata fusse un corpo solo risplendente, chi é che non capisca che nello spazio infinito si può assegnare una distanza tanto grande, dalla quale tale sfera lucida apparisse cosí piccola ed anco minore di questo che dalla Terra ci pare adesso una stella fissa? di lí dunque giudicheremmo allora piccola quella medesima cosa, che ora di qui chiamiamo smisuratamente grande.* ”

Galileo Galilei,
"Dialogo sopra i due massimi sistemi", 1632

Chapter 3

”STRAW” String for Absorption length in Water: first pathfinder mission

STRAW (STRings for Absorption length in Water) pathfinder idea [48], was born in August 2017 aiming at the feasibility study for a new underwater neutrino telescope in Cascadia Basin. Its mission is to achieve a complete characterisation of the optical properties of the candidate site by measuring the scattering length and the absorption length, besides the monitoring of the light background.

The 146 m length mooring lines have been deployed only eight months later from the start of their design, during the summer of 2018, by Ocean Networks Canada and connected to its deep-sea infrastructure offshore Vancouver Island: the strings are continuously taking data since then.

In the short STRAW timeline, we have designed, assembled and calibrated all modules besides strings mechanical structure development.

3.1 Design of the strings

Following the underwater neutrino telescopes design, STRAW is composed of two 146 m length moorings equipped with 5 modules for light detection and 3 modules for light emission.

The modules for light detection are called SDOM-*Straw Digital Optical Module* (described in detail in paragraph 3.4) whose titanium high pressure resistant housing is hosting two 3$''$ PMTs with their read out and data acquisition electronics, while the light sources called POCAM-*Precision Optical CAlibration Module* (described in detail in paragraph 3.3) provide isotropic and nanosecond pulsed light, see fig 3.1 [49].

The two strings are identified as *yellow string* and *blue string*: the yellow one is equipped with two POCAMs and two sDOMs while the blue string has one POCAM and three sDOMs, see fig. 3.2.

Figure 3.1: **Left**: The POCAM housing. Titanium cylinder with BK-7 glass hemispheres on either ends allowing isotropic light emission. **Right**: sDOM (POCAM-like) housing with PMT and electronics.

The idea behind the attenuation length measure [48] is concretized by emitting a flash of photons of known intensity $\boldsymbol{N_0}$ and known wavelength from one of the POCAMs, and measuring the light intensity $\boldsymbol{N(r)}$ detected by one of the sDOMs at distance $\boldsymbol{r}$, whose effective collection area is $\boldsymbol{A_{\mathrm{det}}}$ and $\boldsymbol{L_c(\lambda)}$ is the *attentuation length in water* (explained in detail in paragraph 5.1.1) for a certain wavelength, see equation 3.1.

$$\boldsymbol{N\left(r\right) = \frac{N_0}{4\pi r^2}\ \exp\left(-\frac{r}{L_c(\lambda)}\right)\ A_{\mathrm{det}}} \tag{3.1}$$

From previous studies of other underwater neutrino telescopes, [50], the expected maximum values for the absorption length in water is around 50 m. For this reason, we have designed STRAW geometry to cover distances from 20 to 90 m. The modules are mounted at different heights such as 30, 50, 70 and 110 m above the seafloor. During the design, we have also considered the possibility of data loss: the maximum exploitable length in the STRAW experiment for the Ethernet cable has been 70 m and for the RS485 connections over twisted-pair copper wires has been 130 m.

As showed in fig. 3.2, the instruments and the vertical electrical cables (VECs) have been mounted on a two-line structure made of steel ropes and spacers. Between the top spacer and the buoy, a swivel has been mounted, so that the buoy can freely rotate without affecting the entire structure. In this way, the movements (caused by the pull of the buoys) are limited, to perform measurements keeping a free path for the light travelling from the POCAMs to the sDOMs of both strings.

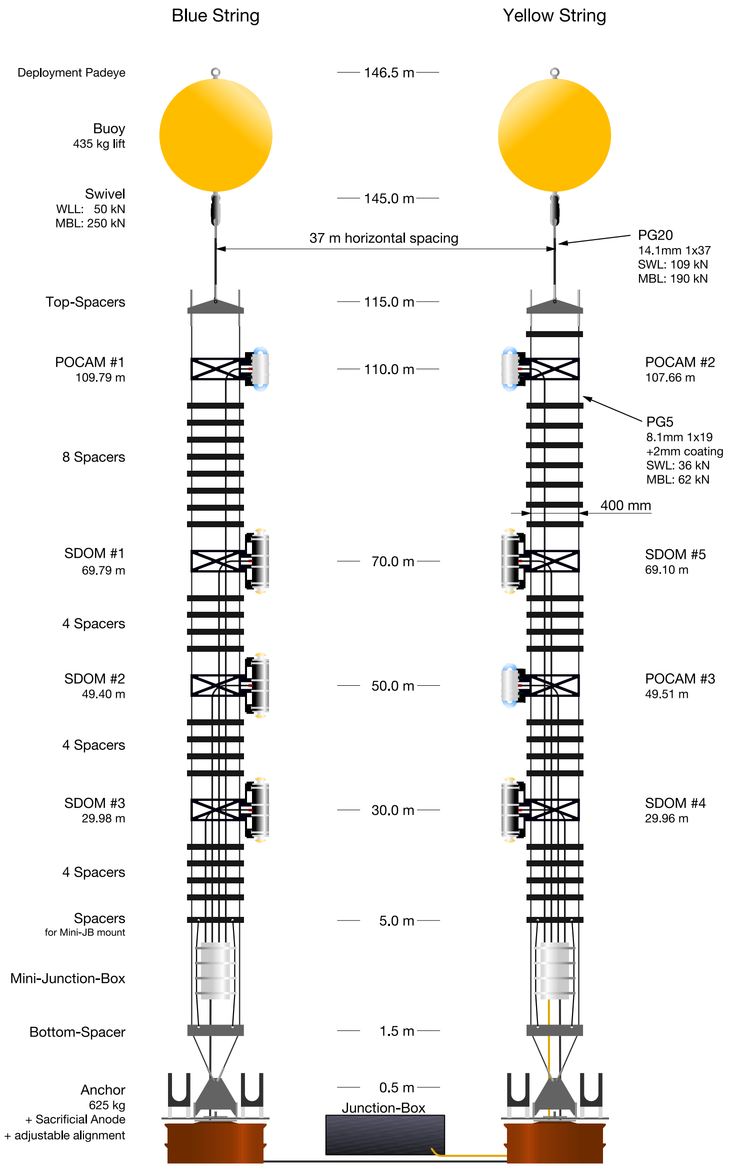

Figure 3.2: Detailed technical sketch of the two STRAW moorings showing the exact (measured) geometry of all modules.

To reduce light reflection on the metal surfaces of the structure and to preserve the mechanical parts from the saltwater, the components have been hot-dip galvanized. When not already available in black, we have coloured

them with a black paint made on purpose for deep-sea application (SikaCor EG-5) [48] [51].
The connection of the two STRAW moorings to the main junction box (node) in Cascadia Basin is carried out through a *mini junction box*, coupled to the VECs and positioned at the end of each string, and an oil-filled subsea cable. A *mini junction box*, fig. 3.3, hosts inside the ONC electronic boards for power and network, the special board named Medusa for the sDOMs synchronization and the microcontroller for the Ethernet accesses, fundamental for handling the power distribution, the synchronization pulse between all the sDOMs and the data acquisition.

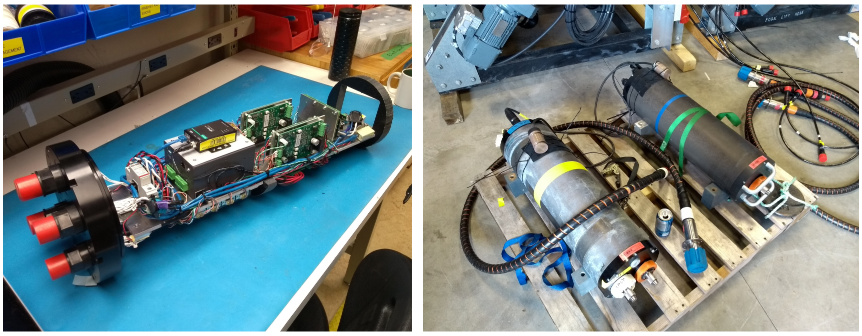

Figure 3.3: **Left**: The internal electronics of a *mini junction box*. **Right**: Exsternal housing of a *mini junction box*. Pictures courtesy of Andreas Gärtner.

The anchor, fig. 3.4, has been designed by Dirk Brussow from the ONC team and is made of two train wheels weighing 625 kg in water. It has been connected to the string structure in a way that, after the deployment, any kind of rotation or repositioning is allowed so that both strings can be aligned as designed.

3.2 Mechanics, deployment and first inspection

3.2.1 Mechanics

The two STRAW strings have been wound around two winches, as shown in fig. 3.5, to ship everything safely to Canada, perform the pool test easily and consequently the deployment. The winches have been designed and produced on purpose (described in detail in the thesis of Andreas Gärtner [52]). To allow the operations of spooling at TUM and unspooling during the deployment directly on the ship, each winch has been coupled to a motor with a gearbox and brakes (by SEW Eurodrive).
All the components have been qualified for the expected deep-sea con-

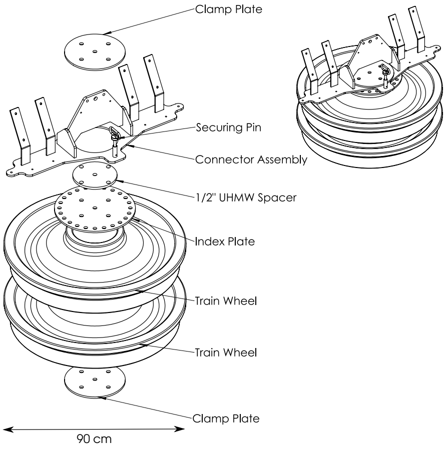

Figure 3.4: Anchor design by Dirk Brussow from ONC team. The rotating structure is held together by threaded bars connecting the clamp plates. The two steel lines of a string are connected to the connector assembly. The connector assembly part also provides two mounting points for two ODI connector plates [48].

Figure 3.5: One of the two spooling systems once arrived at Marine Technology Center in Victoria, Canada: all the modules are covered for light protection and secured to the winch.

ditions and the huge stress that they undergo during the deployment. Vibration tests have been performed at IABG[1], following a standard test procedure for subsea equipment. The modules and their attached mountings have been exposed to sine vibrations in a frequency sweep from 5 to 150 Hz at 5 G in three different axes. Additionally, several shock tests were per-

---

[1] Industrieanlagen-Betriebsgesellschaft mbH (IABG)

formed with an acceleration of 10 G [48].

3.2.2 Deployment and first inspection

In general, two different deployment strategies are used:

- the *bottom-up*, when the string is packed in a structure that is deployed on the seafloor; then a triggered mechanism "opens" the structure and the string starts the unfolding dragged up by the buoyancy force;
- the *top-down*, when the string is unfolded completely on the sea surface and then lowered down through the water until it reaches the seafloor.

Each STRAW mooring has been deployed using a top-down approach. The buoy was laid on the sea surface and dragged out behind the ship by a *rigid-inflatable boat* (RIB). The winch, operated by the ONC team on the back deck, fig. 3.6, unspooled slowly the string with the modules into the water accordingly. After a string was completely unspooled, the ONC team coupled to the steel structure the mini junction box and at last the anchor, as shown in fig. 3.7. After this, the top of the string has been connected to an acoustic release on the heavy-lift line of the ship and the string started to descend by its anchor weight. The string was then released few meters above the seafloor [53].

Figure 3.6: Picture was taken from the live stream camera on the Tully ship during the deployment phase.

Afterwards, the ROPOS ROV has been lowered into the water. Once arrived at the seafloor next to STRAW, it adjusted the position of the strings so that

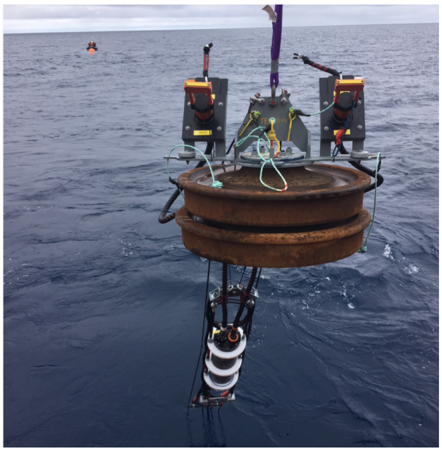

Figure 3.7: Final step of the deployment: one of the STRAW strings attached to its anchor and its mini junction box. At the top-left side of the picture, there are the RIB and the orange buoy of the string.

the modules could face each other.
Then, to check if the modules have been somehow damaged during the descent, the ONC team performed the visual inspection of both strings. The ROV camera looked very closely along the moorings, from the buoy to the anchor, as reported from some video stream screenshots in fig. 3.8.

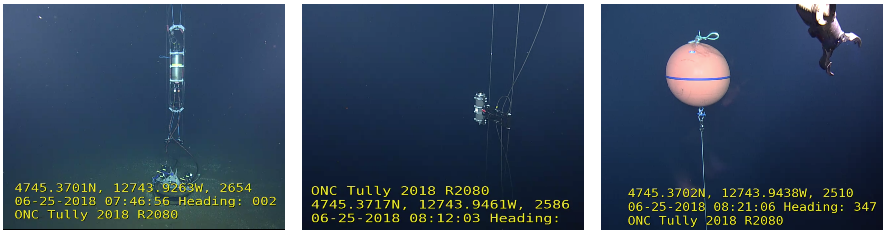

Figure 3.8: Pictures of STRAW from the ROV visual inspection right after the deployment.

As final steps, the ROV connected one string to the junction box of the node, and connected in a daisy-chain the second string to the first: the power switched on revealed that all instruments were perfectly functioning, fig. 3.9.

3.3 Precision Optical Calibration Module: POCAM

The *Precision Optical Calibration Module* - POCAM - provides isotropic, multi-wavelength and nanosecond pulsed light intending to calibrate neutrino telescope detectors.
In the beginning, the design was developed to deploy the POCAM in the

Figure 3.9: The ROV arm holding the cable during the connection operations of the yellow string.

IceCube-Gen2 (upgrade of the IceCube experiment) for reducing the systematic uncertainties by improving the calibration of individual optical modules and the understanding of the optical properties of the ice [54]. The first POCAM prototype was deployed successfully in March 2017 in lake Baikal, fig. 3.10, into the GVD detector where it worked for one year at 1100 m of depth, confirming its proof of concept.
In 2018 it has been adapted for the STRAW experiment. As the POCAM light flashes can be observed by the surrounding sDOM units, it could work perfectly for attenuation length measurements purposes.

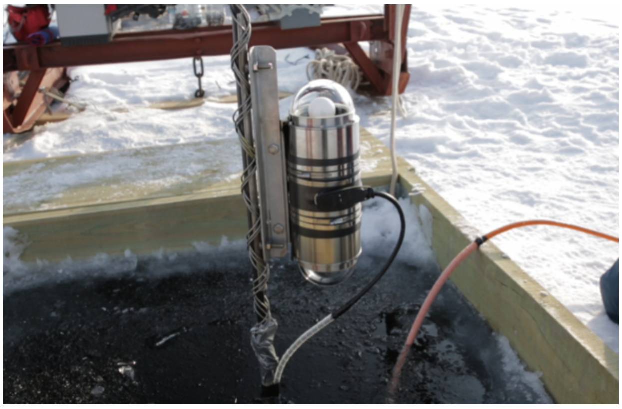

Figure 3.10: Deployment of one POCAM module into GVD detector - lake Baikal, southern Siberia. Picture courtesy of Felix Henningsen.

POCAM module consists of two glass hemispheres made of optically enhanced borosilicate glass N-BK7, less bent to temperature shock damage useful also for the IceCube application. The transmissivity is >95% in the range between 350 nm and 600 nm. They are attached to the flanges of a cylindrical high-pressure resistant titanium housing using deepsea grade epoxy resin [48] (the total length of the module is 40 cm).
On one side of the titanium cylinder, there is a penetrator for the VEOC connection and on the other side a vacuum port allows for degassing and nitrogen-flushing of the module to remove air and humidity: to ensure sealing also in low-pressure water environments, like test tanks before deployment, the pressure inside the housing is set at ∼0.3 bar. This design is certified to withstand an external pressure of 1500 bar, way higher than the working conditions in Cascadia Basin where the pressure at 2600 m depth is around 260 bar, and temperatures down to -40°C. A schematic view of the POCAM housing design can be seen in fig. 3.11.

Figure 3.11: **Left:** Sketch of the POCAM housing: a titanium cylinder with BK-7 glass hemispheres on both ends. **Right:** Picture of the first complete POCAM before shipment.

In each glass hemisphere there is a custom made inverted integrating sphere of *polytetrafluoroethylene* (PTFE) [55] that converts the strongly anisotropic light from the LEDs multi-wavelength matrix into an isotropic diffuse emission profile without altering significantly the pulse shape.
The integrating sphere consists of two mechanical parts: the emitting external part is a hollow sphere with a circular recess on the bottom and a neck, the second part is a plug that completes the sphere providing a prediffusing PTFE layer as shown in fig. 3.12 [48].

The design chosen for this PTFE sphere homogenizes the light pulses of different LEDs. The isotropic emission profile achieved is shown in fig. 3.13

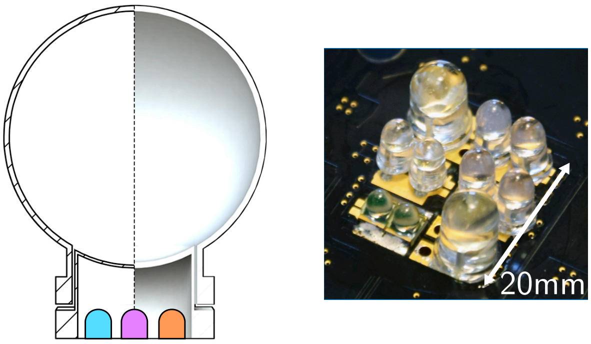

Figure 3.12: **Left:** POCAM integrating sphere two parts sketch. The plug that completes the sphere is coupled on the bottom to the LEDs matrix. **Right:** POCAM LED layout as used inside the integrating sphere plug. The corner LEDs are Kapustinsky-driven, the central LEDs are backup flashers driven by the FPGA directly [48] [51].

with polar isotropy of 5.4% and an azimuthal uniformity of 4.7%. The intensity of the light output is constantly monitored in-situ by a 3x3 mm^2 SIPM from Ketek (PM3315-WB) and a large-area PIN-photodiode from Hamamatsu (S3590-08), mounted right next to the integrating sphere.

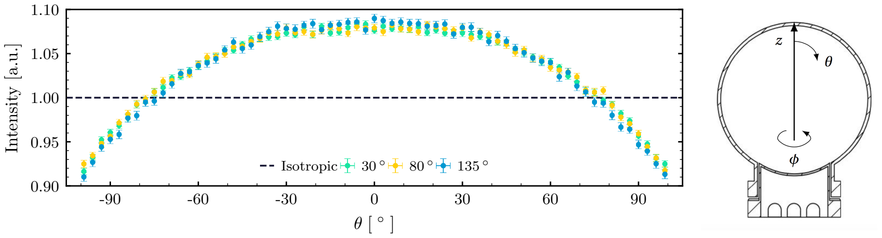

Figure 3.13: The achieved emission profiles are homogeneous for different LEDs emission opening angles. The considered polar angle θ is measured with respect to the axis of LED emission pulse, as shown in the right side of the figure.

The array of LEDs is driven by a Kapustinsky-style circuit [56] [57] that emit light pulses of about 10 ns time width and a maximum of 10^8 - 10^{10} photons. Thanks to the adjustable light intensity, POCAM flashes can cover a large range of distances for different possible attenuation lengths measurements while thanks to the timing it is possible to discriminate between direct and scattered light.
In addition to the Kapustinsky driven LEDs array two backup FPGA driven LEDs have been mounted on the flasher board (to be used in case the optical properties would have been much worse than expected): they emit high-intensity pulses with respect to the Kapustinsky ones, with a time width of 40 ns. The final LEDs configuration is showed in the tab. 3.1.

LED	Color	Wavelength[nm]	Kapust.	FPGA
XSL-365-5E [58]	UV	365 ± 8	1x	–
XRL-400-5E [59]	Violet	405 ± 8	1x	–
NSPB300B [60]	Blue	465 ± 7	2x	2x
WP710A10LZGCK [61]	Green	525 ± 17	–	2x
CSL0701DT5 [62]	Orange	605 ± 6	2x	–

Table 3.1: The chosen POCAM LEDs of STRAW are listed in this table with their wavelengths and their multiplicity on the flasher board (Kapustinsky or FPGA cicuit driven) [51].

The functionalities of the POCAM are implemented on three different boards [48]:

- *the power supply board* converts the input voltage to local 12 volts and it provides a local 10 MHz clock to both hemispheres;
- *the digital board* hosts a microcontroller, an FPGA, a 10-bit/10 MHz ADC and storage memory;
- *the analog board* hosts the LED flashers, the photodetectors for the in-situ monitoring and their readout electronics.

Acquired data are first stored in the module and then transferred to the ONC shore station where all the data are collected.

The isotropic light emission of the POCAM has been at the end verified measuring the light output considering the whole housing geometry. Nevertheless, the potential refraction of the glass hemispheres effects, the light emission profile was still compatible with the one measured considering only the PTFE sphere coupled to the LEDs matrix. The results of these measurements are shown in the plot in fig. 3.14.

3.4 STRAW Digital Optical Module: sDOM

The *STRAW Digital Optical Module* (sDOM) main goal is to estimate the attenuation length and to monitor the deep-sea optical background by detecting POCAM flashes.
The mechanical design chosen for the sDOM is similar to the POCAM one, exploiting the fact that this latter was successfully tested and deployed in lake Baikal as described in paragraph 3.3. It just includes a longer titanium cylinder (the length of the module is 60 cm) to have more space for hosting different electronics boards.

Also the sDOM module has at both ends two borosilicate glass N-BK7 hemispheres and, such as the POCAM, its titanium cylinder is equipped

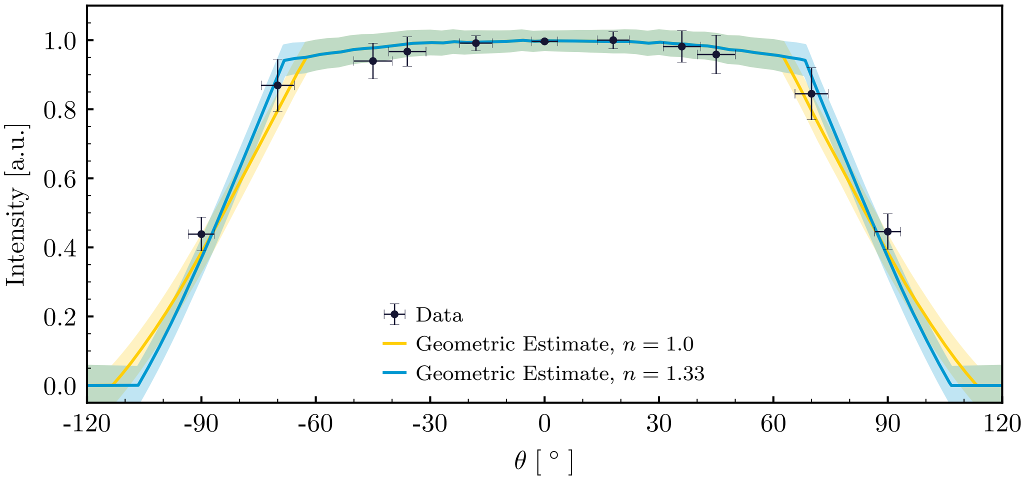

Figure 3.14: One POCAM hemisphere emission profile in air or water geometric estimation: light output intensity versus polar angle θ. The data points show a preliminary measurement of the angular intensity emission in the air. They match pretty well the bands of geometric estimation.

with a penetrator for the VEOC connector coupling and with a vacuum port (used to set a very low internal pressure - always ∼0.3 bar - and remove air and humidity that could damage the electronics).
The sDOM design is qualified to withstand an external pressure of 600 bar (while for the POCAM this value is equal to 1500 bar), still way higher than the pressure conditions present at 2600 m b.s.l. at Cascadia Basin.
A schematic view of the POCAM housing design can be seen in fig. 3.15.

Differently from the POCAM, the two glass hemispheres are coupled with the *optical gel* to two 3" *photomultiplier tubes* - PMT - that are connected to their HV bases and readout electronics. The details on the photosensors chosen and their characterisation tests are described in detail in the paragraph 3.6.

The sDOM electronics, whose schematic view is shown in fig. 3.16 can be identified with three main parts [48]:

- *analog part*: the PMT readout is implemented with a four-channel resistive splitter board connected to the Padiwa board (initially developed at GSI in Darmstadt for collider experiments) to shape and discriminate the signal. For a better reconstruction of signals shape, the four different thresholds allow the measure of PMT signals at different levels, thus providing pulse charge information.
- *digital part*: connected to the Padiwa, the standard Trigger Read-out Board (TRB3sc - always developed at GSI) handles the measurements

Figure 3.15: **Left**: Schematic design of the sDOM. **Right**: Picture of the sDOMs and POCAMs ready for the shipment to Canada. Picture courtesy of Felix Henningsen [51].

of PMT signals implementing the whole DAQ system (CTS and TDC) in one FPGA. It records the time over threshold (ToT) of the PMT pulses, including precise timestamps, at four different voltage levels [63].

- *ethernet part*: an Odroid C2 computer running on a standard Armbian OS has the main control of the entire sDOM module. It is connected to the TDC board (on the TRB3sc) on one side and on the other to an auxiliary board called Polyphem that is responsible for converting the incoming 48 VDC power to the internal 5 VDC supply voltage as well as connection to the surface (through a standard USB ethernet adapter).

The sDOM housing is moreover equipped with different sensor for long term monitoring: an MS8607 sensor provides temperature, relative humidity and pressure of the entire module; a DS1822 temperature sensor provides the DC/DC stage temperature and a unique 48 bit ID for all sDOMs; two additional DS18B20 temperature sensors are mounted on the PMT bases.

As described in paragraph 3.1, a Medusa board (developed by Michel Böhmer - ZTL at TUM) hosted in the mini junction box of each string provides a synchronization signal to the sDOMs by use of the LVPECL signal standard, and handles the power distribution and the data acquisition.

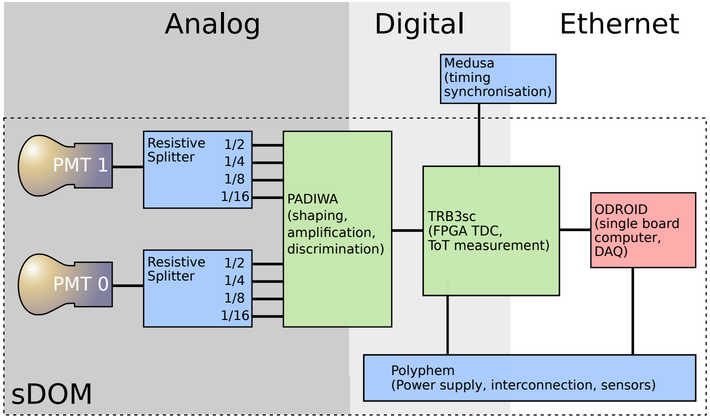

Figure 3.16: Scheme of the sDOM electronics. Custom designed and produced electronic parts are shown in blue, TRB hardware by GSI is shown in green, and the Odroid C2, which could be bought from stock is shown in red [48].

3.5 Final water tank test at ONC facility

Once arrived in Canada, before the deployment, each module has been tested in a small saltwater tank to check for any current leakage and ground faults potentially caused by the shipment.
Since no issues showed up, the modules have been integrated into the strings whose cables systems were previously wound around the winches.
Hence, the entire assembled spools were deployed in a saltwater pool at Marine Technology Center (MTC) of ONC for the underwater functional tests that lasted several days. In this phase, the ONC IT team ran the firsts tests with the driver software required to operate STRAW and to collect the data stream on the ONC web platform.
Since the PMTs of the sDOMs needed to be completely shielded from light, 3D-printed protective shells covered the glass hemispheres of the sDOMs, as can be seen in fig. 3.17, and additionally a black tarp covered the entire pool. The 3D-printed protective shells have been removed just right before the deployment in ocean water.

Figure 3.17: One string entering the pool for final underwater functional tests at MTC some days before the deployment.

3.6 Photosensors of STRAW

3.6.1 The PhotoMultiplier Tube: PMT

A photomultiplier tube, PMT, is a light detector extremely sensitive to ultraviolet, visible and near-infrared wavelengths. A schematic of a PMT is shown in fig. 3.18.
This device is so sensitive that it can detect even just one single photon.
The PMT working principle is mainly based on two effects: the *photoelectric effect* and the *secondary electrons emission*.
It consists of a vacuum tube with an input window, a photocathode, a focusing electrode, an electron multiplier chain and an anode. The working principle steps can be listed as follows [64]:

- a photon passes through the input window;
- it excites electrons on the photocathode, emitting photoelectrons (photoelectric effect);
- photoelectrons are accelerated and focused by the focusing electrode into the first dynode where they are multiplied through secondary electrons emission (this secondary emission is repeated through the entire dynode chain: there is thus a cascade phenomenon whereby up to 10^6 electrons are generated on average for a single photon hitting the tube);
- the electrons emitted from the last dynode are finally collected by the anode that produces the output signal.

The PMT **quantum efficiency** is the ratio between the number of photoelectrons emitted by the photocathode n_k and the number of incident photons

n_p:

$$\eta = \frac{n_k}{n_p}. \tag{3.2}$$

Photons at shorter wavelengths carry higher energy if compared to those at longer wavelengths: this can increase the probability of electron emission. As a consequence, the maximum quantum efficiency occurs at a slightly shorter wavelength than the *radiant sensitivity* [2] peak one, as shown in fig. 3.19.

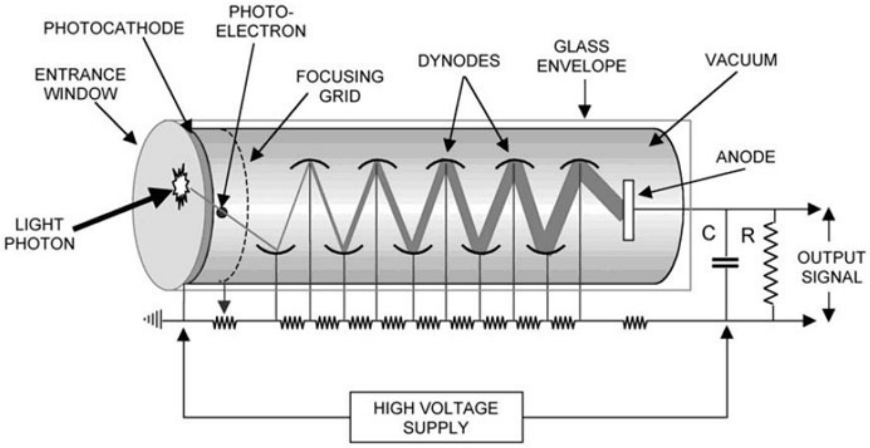

Figure 3.18: Photomultiplier design and illustrated working principle scheme.

Even in absence of light sources, the PMT can produce a signal. In this case, it generates a weak intensity current defined as **dark current** whose presence is due to different phenomena that can occur within the PMT as:

- *thermoioic emission current* from the photocathode and dynodes (even at room temperature): it consists in the thermal electrons emission after their kinetic energy increases so much to allow them to win the bonding force of the electrodes atoms;
- *leakage current*, caused by imperfect insulation of the glass or the pin socket;
- *photocurrent* produced by scintillation from glass envelope: the electrons emitted by the photocathode may deviate from their normal trajectories and if they hit the glass envelope, scintillations may occur and result in dark pulses;

---

[2] Radiant sensitivity is defined as the photoelectric current generated by the photocathode divided by the incident radiant flux at a given wavelength [64]

- *ionization current* from residual gases: even if the internal part of a PMT is at a high vacuum, there are residual gases whose molecules may be ionized by collisions with electrons;
- *noise current* caused by cosmic rays and radiation from radioisotopes contained in the glass envelopes.

One of the basic features of a PMT is the **gain** that can be defined as the ratio between the anode current and the cathode current; this is equal to the ratio between the number of electrons present on the anode and the number of photoelectrons emitted by the cathode.
If the voltage difference between the dynodes is the same, the gain follow the low 3.3:

$$G = k(HV)^{N\alpha} \tag{3.3}$$

where HV is the supply voltage, k depends on dynodes material, N is the number of dynodes and α is a constant between 0.6 and 0.8.
Usually the electrons secondary emission δ is function of the voltage between the dynodes and it is expressed as in 3.4:

$$\delta = a \cdot E^k \tag{3.4}$$

where a is a constant, E is the electric field between the dynodes and k is the already cited constant that depends on the dynode material. If the field E is not constant it is necessary to calculate the different δ for each dynode and the final *gain* then will be written as in 3.5:

$$G = \alpha \cdot \delta_1 \cdot \delta_2 ... \delta_n \tag{3.5}$$

Even if the electron multiplier mechanism is designed on purpose for an efficient electron trajectory, it needs to consider that some electrons may deviate from their favourable trajectories, not contributing to multiplication and then to the *gain*. This is related to the **collection efficiency**, defined as the probability that photoelectrons will land on the effective area of the first dynode. This is a merely technological issue: typical values of collection efficiency are between 90% and 95% [64]. If the cathode-to-first-dynode voltage is low, the number of photoelectrons that enter the effective area of the first dynode starts to decrease as well as the collection efficiency.

Another basic characteristic of the PMT is the **linearity** of the response, defined with respect to the input light signal; good linearity requires that each dynode collects all the current from the previous one, to maintain a certain proportionality from the cathode through the entire dynodes chain.
In general PMTs show good linearity for a wide range of incident light level but if this quantity is too high, the output signal will start to deviate from the ideal linearity behaviour.
Thus, the anode *non-linearity* depends mainly on the space charge density

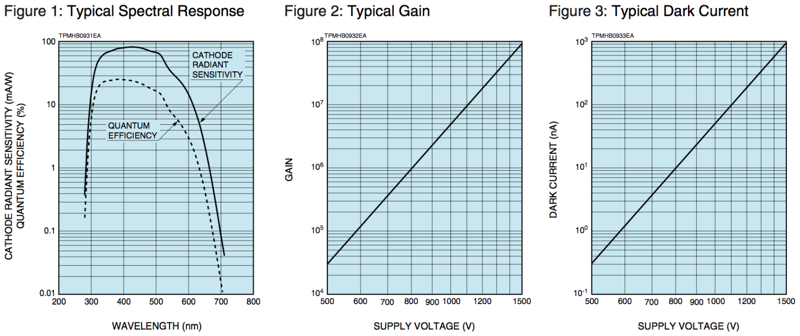

Figure 3.19: Characteristics of the Hamamatsu PMT R12199 from the datasheet provided by the manufacturer.

effect, due to the huge current that flows within the dynodes when a high-intensity light pulse hit the photocathode. This reduces the electric field and the multiplicative effect. In the end, the amount of collected current will be less than the one expected. These *saturation* effects depend also on the power supply: when the HV increases the space charge density around the dynodes decreases, but more electrons will reach the anode and, as a consequence, the PMT saturates for a higher value of anodic current.

The PMT time response is exceptionally fast, on the order of nanoseconds. It is defined by the *transit time* necessary to the emitted photoelectrons to reach the anode after being multiplied (called also *electron transit time*). When a PMT photocathode is in single-photon illumination conditions, the transit time of each photoelectron has a fluctuation: this fluctuation is called TTS (transit time spread) and it is measured as the FWHM of the transit time Gaussian distribution (equal to $\sim 2.35\sigma$) [64].
The TTS is caused by the spread in the electron path length: for example, some electrons produced at the edge of the photocathode have longer trajectories and a weaker electric field to reach the dynode chain. Additionally, the TTS is influenced by differences in the velocity emission of the secondary electrons [32].

In the paragraph 3.6.3 I will illustrate the characterisation phase of the STRAW PMTs and the evaluation methods of all the quantities listed above.

3.6.2 The PMT chosen for the sDOM

Inside each glass hemisphere, the sDOM includes two Hamamatsu Photonics R12199 PMTs, having a 3″ hemispherical Bialkali photocathode with a spectral response range of 300-650 nm and an average 25% peak quantum efficiency at 390 nm, fig. 3.20.

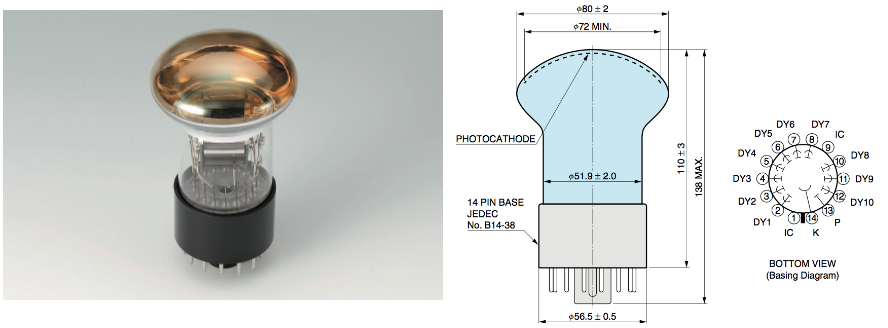

Figure 3.20: Picture of the Hamamatsu Photonic PMT R12199 and its dimensional outline and basic diagram.

The two PMTs are glued to the glass hemispheres, whose refractive index is n_{Glass} = 1.53, with an optical gel (Wacker *SilGel 612*) having a similar refractive index (n_{Gel} = 1.4 at 589 nm) thus optimizing the transmission between 350 nm and 600 nm. In this way, the reflections and refractive losses are reduced and the overall field of view is maximised.
Due to this spectral response, the sDOM is perfectly able to monitor bioluminescence phenomena (see paragraph 5.1.5), Cherenkov light and POCAM light emission, whose LED array produces light from 350 to 610 nm (see paragraph 3.3).
The power supply minimum value for the PMTs to be functional is 1000 V; thanks to the active base socket C12842-02 MOD (Cockcroft-Walton) from Hamamatsu, fig. 3.21, customized on purpose for STRAW by the manufacturer, it is possible to generate high voltage maintaining low power consumption since this base is working with only 5 V.
STRAW moorings system is powered with 48 Volts coming from the ONC infrastructure and, for this reason, each sDOM is equipped with a DC/DC converter transforming the 48 V supply voltage into the 5 V needed to the PMT socket. An additional analog control input, which is 1/1000 of the PMT HV setting, sets a control voltage value from 0 V to 1.5 V allowing the setting of the PMT working point.

3.6.3 PMT characterisation and tests

I focused part of my PhD on the characterisation of all the 10 PMTs chosen for the STRAW optical modules.
To achieve a homogeneous response of the entire STRAW system all the PMTs needed to be set at the same gain. Thus the main goal of this work has been to find the optimal working point for the photosensors [48].

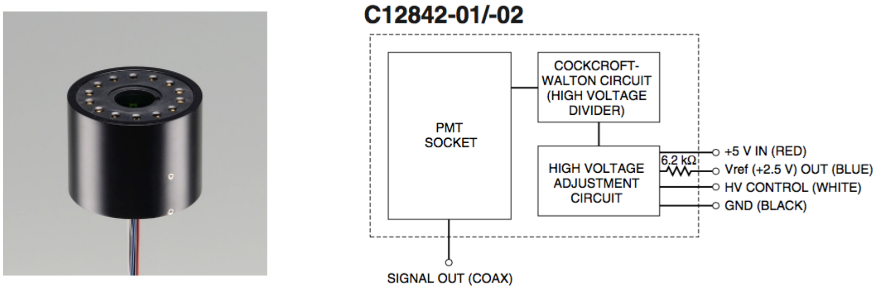

Figure 3.21: Picture of the custom made C12842-02 MOD socket and its electronic schematic diagram. Pictures provided by Hamamatsu Photonics.

Through an extensive characterisation campaign on the adopted PMTs I have measured mainly five quantities: single photoelectron signal amplitude and charge, gain, dark counts, transit time spread (TTS) and linearity (dynamic range), all described in detail in paragraph 3.6.1.
The setup used for the PMT characterisation is described in Fig. 3.22.
It is mounted inside a sealed dark box and it is composed by:

- a picosecond pulsed laser (PiLas, $\lambda = (405 \pm 15)$ nm, pulse width < 45 ps, up to 100 MHz),
- an optical attenuator (PiLas, attenuation range 0 to -80 dB),
- two optical fiber splitters (50% and 10-90% emission ratio, respectively),
- a power meter (Newport 2936-R) with power probe (Newport 918D-UV-OD3R),
- an oscilloscope (Teledyne LeCroy HDO6054, 500 MHz, 2.5 GS/s).

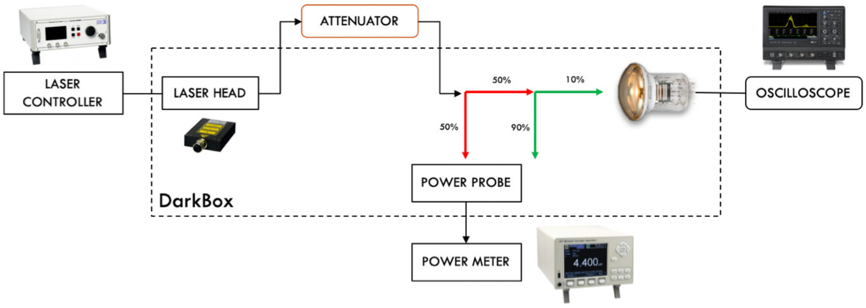

Figure 3.22: Experimental setup used for PMT characterization.

Using the calibrated power probe and power meter, thanks to in-depth measurements, I have firstly estimated all the insertion losses and attenuations of the overall optical fiber splitters system.

The characterisation phase of the PMTs[3] started measuring, in absolutely dark condition, the *single photoelectron signal charge* at different HV values to calculate the *gain* of the PMTs: this has been done after scaling down the laser light emission to the single-photon level.
In fig. 3.23 the single photoelectron signal charge distribution is expressed in $Volt \cdot sec$. Excluding the pedestal due only to triggered PMT electronics noise (whose mean value is zero), the considered total charge for each chosen HV is the peak of the second Gaussian, divided by the 50-ohm oscilloscope impedance. Consequently, the *gain* is calculated as the total charge, divided by the single-electron charge.
The trend of the gain with respect to the HV, for all the PMTs tested, is shown in fig. 3.24 [49] (with a logarithmic scale on both axis).

During the identification of the single photoelectron signal charge, I have measured also the *single photoelectron signal amplitude*. This has been helpful to identify the trigger thresholds for the next steps.
Both acquisitions have been carried out by the oscilloscope using the external trigger provided by the laser source.

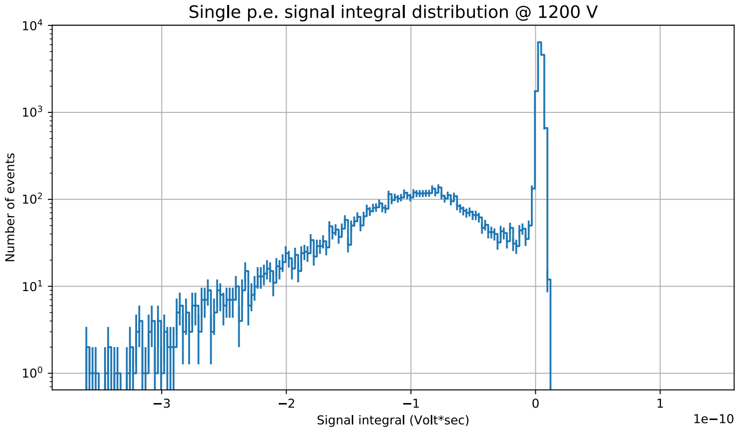

Figure 3.23: Example of single photoelectron signal charge distribution.

The next step of the characterisation focused on measuring the dark rates of the bare PMTs with respect to the power supply as shown in the

---

[3] Each PMT has been tested with its socket.

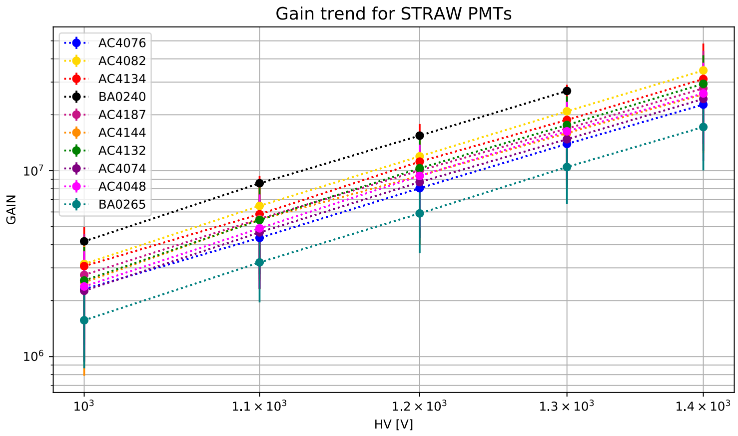

Figure 3.24: Gain vs. supply voltage of all PMT of STRAW. For the BA0240 the gain has been measured only up to 1300 V.

example in fig. 3.25, to discriminate, once STRAW has been deployed, the background produced by bioluminescence and ^{40}K decay.

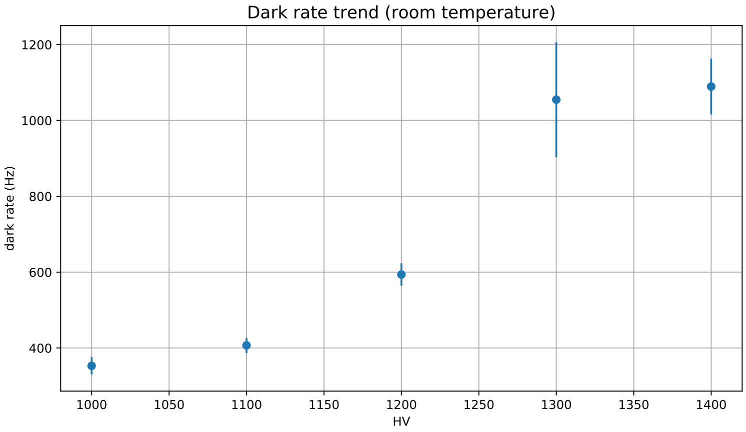

Figure 3.25: Example of dark rate vs. HV for one of the STRAW R12199 PMTs. The measures have been taken after 24h of pre-darkening and with a 1/3 photoelectron threshold.

The long-term monitoring of the dark rates revealed the day-night modulation induced by a slight temperature change in the laboratory. An example of one PMT is reported in fig. 3.26; this fluctuation, produced by a variation of the ambient temperature of ∼2 degrees during the night, can

be considered negligible when compared to the dark rate measured after coupling the PMT with the glass hemisphere (in a range from 1 kHz to 2.5 kHz), fig. 3.27. In this case, the large increase of dark noise is caused by the radioactivity of the glass envelope.
It is worth remarking that these dark rates measurements have been performed at ambient temperature, thus representing an upper limit with respect to the operating conditions in Cascadia Basin (stable temperature of the water at about 2°C).

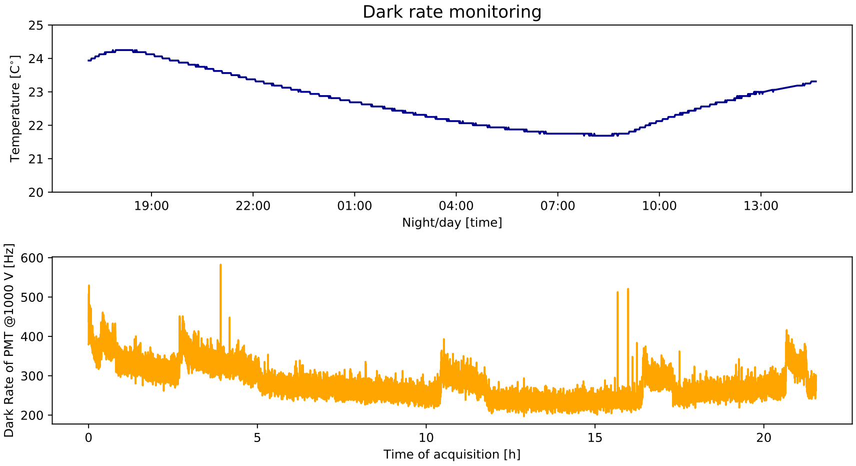

Figure 3.26: Long term monitoring of dar rates at room temperature. Measures are taken after 24h of pre-darkening and with a 1/3 photoelectron threshold.

The Transit Time Spread (TTS) is the intrinsic fluctuation of the electron transit time, as already described in paragraph 3.6.1.
Evaluating the TTS at different HV is fundamental for the arrival time of light pulses estimation. Always using the same setup as in fig. 3.22, to illuminate completely the photocathode with single photons, the distance to set between the PMT and the light output of the optical fiber, has been calculated considering the numerical aperture of the fiber and the size of the photocathode diameter. Once in the single-photon conditions, it has been measured the time interval between the laser output trigger signal (START) and the 0.3 *pe* threshold of the PMT output signal (STOP): this time corresponds to the sum of two quantities, the Electron Transit Time (ETT) and the time that light needs to propagate through the fibers and splitters chain. Considering negligible the fluctuations of the latter, the overall measured fluctuation corresponds to the TTS of the PMT.
For each HV run, the histograms of the distributions have been analyzed. The TTS has been estimated as the FWHM of these distributions. The results are in the range between 2.5 ns and 4 ns, fully in agreement with

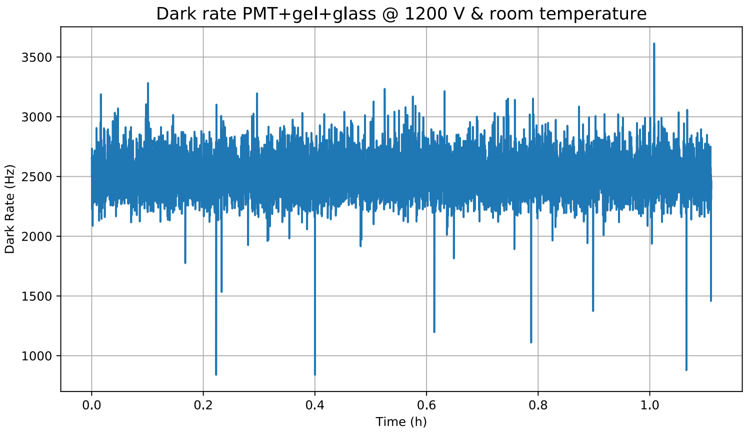

Figure 3.27: After the integration of the PMT in the glass hemisphere, due to the radioactivity of the glass, the PMT dark rates increase from 600 Hz to 2500 Hz at 1200 V and room temperature. See fig. 3.25.

expectations and with the TTS measurements done by the KM3NeT collaboration on the same type of PMTs [65].
In fig. 3.28 are shown the TTS trends at different HV for each STRAW PMT tested.

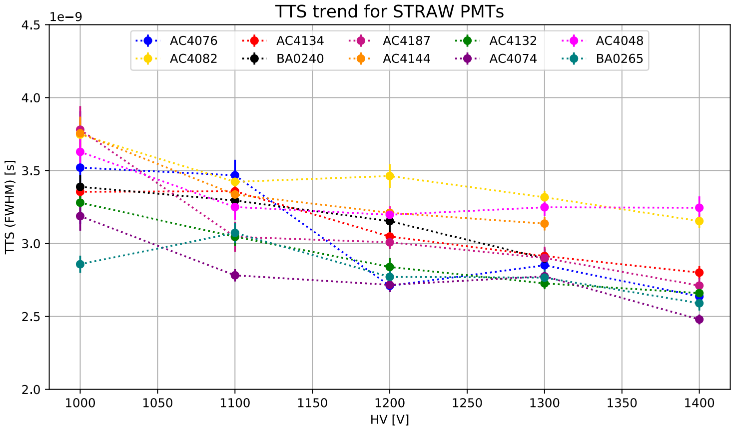

Figure 3.28: TTS trends at different HV for each STRAW PMT tested

The last step of the characterisation has been the study of the linearity of the PMTs response and the consequent saturation.
In general, a PMT shows good linearity in output current over a large range

of incident light levels but if the incident light amount is too large, the output signal begins to deviate from the ideal linearity. To define this range in terms of detected photons, and consequently predict the amount of light that a POCAM should emit to reach a certain sDOM without saturating its PMTs, the linearity behaviour of PMTs has been investigated. The PMT has been illuminated with different amount of light and powered with different HV values, the output signal charge is measured with the oscilloscope.
In the plot in fig. 3.29 is shown as an example for the linearity of one R12199 PMT, at different HV: the number of electrons at the first dynode to the number of photons that reach the photocathode.
The number of photons has been estimated from the values measured by the power meter considering the attenuations of the fiber splitter chain; the number of electrons at the first dynode N_{e^-} is calculated as in the equation 3.6:

$$N_{e^-} = \frac{Q_{TOT}}{G \cdot q_e} \tag{3.6}$$

where G is the Gain previously measured, Q_{TOT} is the total charge measured at the anode with the oscilloscope and q_e is the electron charge [48] [49]. The number of produced electrons in the dynode chain increases as the *gain* increases with the power supply. This means that for the same amount of light (i.e. same amount of photoelectrons produced by photocathode), the dynodes chain produces a greater number of charges on the anode and the PMT response will not be linear anymore.
Moreover, from the slope of the fitted line in the linear region, it is possible to evaluate the *quantum efficiency* of the PMT.
In reality, in this case, it is not trivial to discriminate between the *quantum efficiency* and the *collection efficiency*, thus it is possible to estimate their product estimating the slope (which is the ratio between the number of photoelectrons that reach the first dynode and the number of photons that hit the photocathode). In the plot, the three slopes are in agreement and, considering a typical collection efficiency for the R12199 of $\sim 95\%$, point to an estimated value for the quantum efficiency (QE) of the PMT of about 29% [48] [49].

3.7 STRAW first results

In this chapter, I have described extensively design, mechanics, light sources, light sensors, the fundamental working principle and the goal of the two STRAW moorings besides my contributions to the realization of this experiment.
Immediately after the successful deployment STRAW started the data-taking, even if the final stability has been achieved after some months of DAQ fine-tuning at the end of February 2019.
So far STRAW has collected more than two years of data that are currently still under investigation.

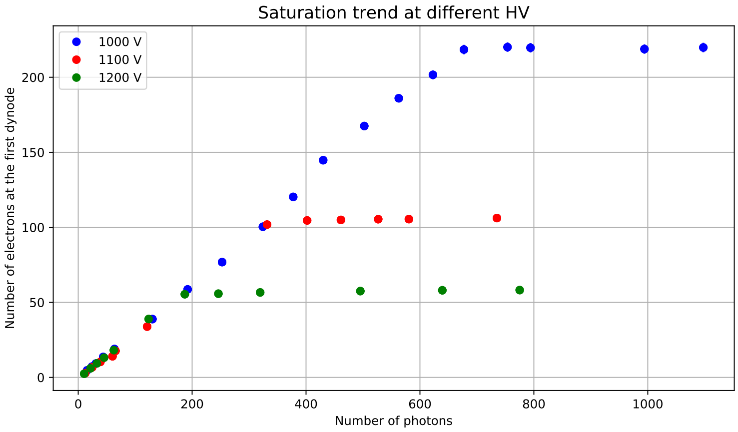

Figure 3.29: Linearity trend for one STRAW PMT at three different power supply values. The slope of the fitted line in the linear region is the *quantum efficiency*: ratio between the number of incident photons and number of electrons at the first dynode.

The measurements of the attenuation length looked promising from the beginning: this topic will be treated in depth in a next future publication but preliminary results are described in the paragraph 5.1.2 thanks to the work of Dr Christian Fruck (TUM) and Andreas Gärtner (TUM-ONC).
The long term monitoring of the light background, which has been another significant part of my PhD work, has been focused on the understanding of bioluminescence phenomena and environmental radioactivity around the detector in Cascadia Basin, in view of the future P-ONE neutrino detector design.
I have described the entire STRAW data analysis in the chapter 5.

> “ *Secondariamente, io tengo per fermo che nella Luna non siano piogge, perché quando in qualche parte vi si congregassero nugole, come intorno alla Terra, ci verrebbero ad ascondere alcuna di quelle cose che noi col telescopio veggiamo nella Luna, ed in somma in qualche particella ci varierebber la vista; effetto che io per lunghe e diligenti osservazioni non ho veduto mai, ma sempre vi ho scorto una uniforme serenitá purissima.* ”

Galileo Galilei,
"Dialogo sopra i due massimi sistemi", 1632

Chapter 4

”STRAW-b”: second pathfinder mission

The STRAW-b experiment, the second pathfinder for the Cascadia Basin site, started to be designed at the end of 2018.
After the successful deployment of STRAW and its first promising results, STRAW-b was born to verify the attenuation length measurements and study the spectrum of the light background, thus adding new information to the intensity of the rates registered by STRAW sDOMs.
STRAW-b consists of a longer mooring ($\sim$500 m) compared to STRAW ones. The mission included the deployment technique test for future P-ONE moorings, as the string length is very close to the one generally used for underwater neutrino telescope moorings.
The deployment of STRAW-b took place during summer 2020, about two years after the beginning of the project. During this relatively small time window, all modules, together with their mechanical structure, have been designed, assembled and tested. The mooring has been connected to the underwater ONC infrastructure $\sim$40 meters from STRAW, as shown in fig. 4.1 and since then is taking data while the TUM team is fine-tuning the acquisition process and the ONC team is finalising the integration into the ONC web platform.

4.1 Design of the string

In order to be as close as possible to the future P-ONE moorings, STRAW-b design is based on one 500 m length mooring equipped with ten modules: three *Standard Modules* and seven *Specialised Modules* all composed by a spherical 13$''$ high-pressure resistant glass housing, see fig. 4.2.

The *Standard Modules* (described in detail in paragraph 4.3.1) provide constant monitoring of pressure, temperature and humidity. In addition,

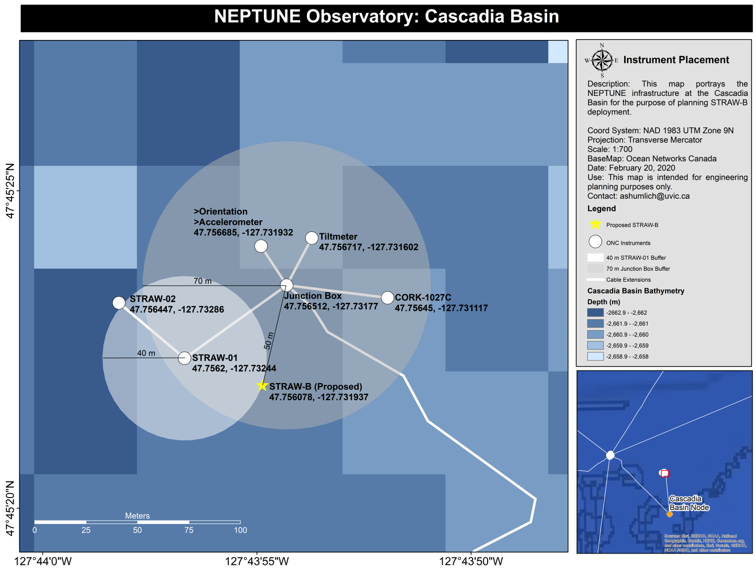

Figure 4.1: Map of the positions for STRAW and STRAW-b in Cascadia Basin.

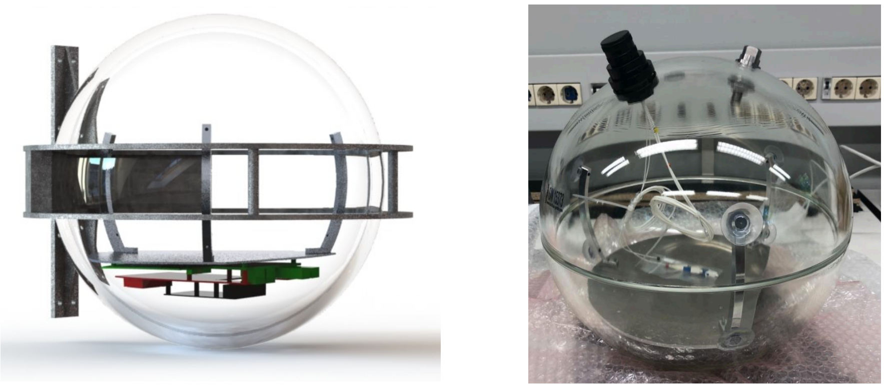

Figure 4.2: **Left**: Schematic of STRAWb 13″ high-pressure resistant glass housing and its mounting. **Right**: Picture of the housing sphere sent from the manufacturer (Nautilus MarineService Gmbh) equipped with penetrator, cable connector and internal mountings for hosting the electronics.

they are used as testing ground for components and electronics that will be used for P-ONE.

The *Specialised Modules* (described in paragraph 4.3.2), instead, have the goal of performing new measurements compared to STRAW ones. The aim is a further characterisation of the Cascadia Basin site water optical properties and light background. These modules are:

- two PMT-based spectrometers,
- two LiDARs (Light Detection And Ranging) based on laser diode and μPMT,
- one muon tracker using scintillators and SiPMs,
- one CMOS based mini spectrometer module,
- one Wavelength shifting Optical Module-WOM (from Johannes Gutenberg - University of Mainz).

To have a second precise measurement of the Cascadia Basin attenuation length, the STRAW-b idea for measuring the absorption and scattering lengths is implemented by the two LiDARs. This alternative measurement technique adopts short light pulses at 450 nm wavelength, emitted into the seawater, then scattered back and detected.

The light background spectrum measurement is assigned to the *spectrometers*, using PMTs and CMOS sensors to detect and analyse a wide range of light intensity from about 340 to 850 nm. The different adopted techniques are described in details in the following paragraphs.

As can be seen in fig. 4.3, the ten modules are distributed from 120 m to 432 m alongside the bundle of ten Vertical Electrical Optical Cables - VEOCs - that compose the mooring. The VEOCs are hybrid cables composed of two copper wires, used for the power supply, and two single-mode fibers[1] used for communication.

At the beginning of the project, the number of VEOCs was 14: the shortest one was 120 m in length and the longest 432 m, with increasing steps of 24 m. Since for STRAW-b we planned only ten modules, it has been possible to save four cables for testing and spare pieces. In this way, considering the cables missing, the VEOCs result divided into three sections: the first section is from 120 to 168m, the second section is from 240 to 312m, and the third section is from 384 to 432m. Hence, the modules are distributed in each section every 24m with a jump of 72m between two consecutive sections.

The VEOCs are coupled to the mechanical backbone made of steel cable (spiral rope with 19 one wire strands and a diameter of 8.4mm): this is provided with ferrules every 12 m to allow module and spacers mountings (described in depth in the paragraph 4.2.1) and, as for STRAW, to reduce light reflection and to avoid corrosion from salt water, it has been coated with a Galvan zinc-aluminium alloy.

One of the crucial parts of the design has been taking into account the length of the VEOC cables connector, that is around 20 cm (SEACON OPT-G-4-CCP dry-mate connector): the external mounting and the deployment

---

[1] Single Mode optical fibre has a small core diameter: this allows the light to propagate only in one way, strongly limiting the number of internal reflections and attenuations. Hence the signal can travel further without distortion.

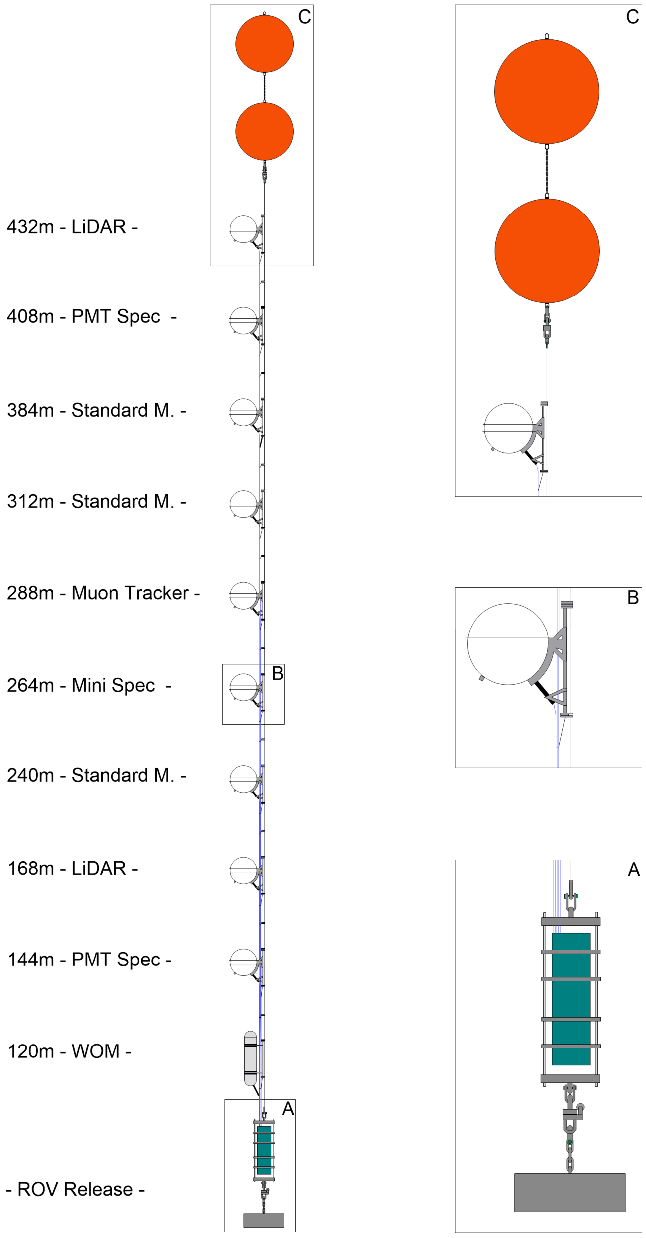

Figure 4.3: Sketch of the STRAW-b mooring: a bundle of 10 VEOCs equipped with modules coupled to the mechanical backbone made of steel cable. On the right of the picture a detailed view of the two buoys system and *mini junction box* with the anchor. Picture courtesy of Christian Spannfellner.

procedure have been tailored around this feature since such a long connector creates a large lever arm [6] and the modules glass sphere can be damaged by mechanical shocks.

In the upper part of the string, the buoyancy system (two 44″ buoys with a combined buoyancy of 622kg, depth rating of 2500m [6]) is connected to the mooring with a swivel so that it can rotate with currents without affecting the string.
The connection between the VEOCs and node is performed through a *mini junction box* developed and built by the ONC team. The *mini junction box* provides power, converting high voltage coming from the node to lower voltages for the mooring (15V, 24V or 48V), and handles the communications with the deployed instruments. Similar to the STRAW anchor, the STRAW-b anchor is made by two train wheels (designed by ONC), weighing approximately 592 kg in water. Differently from STRAW, it is not necessary to have a mooring that can rotate, so the anchor is fixed with a simple chain to the entire structure, as shown in fig. 4.4. The future recovery of the string is in any case guaranteed by the so-called ROV release. The ROV can detach the mooring from the anchor by triggering a mechanical release, while the buoys force brings the mooring to the ocean surface [6].

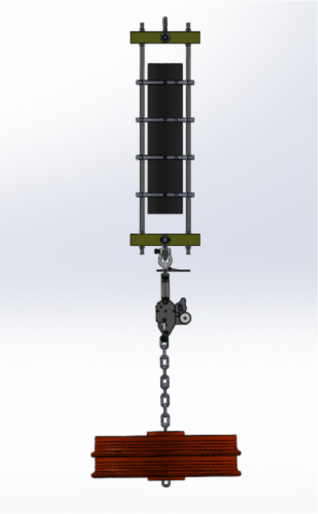

Figure 4.4: Design of the STRAW-b assembly.

4.2 Mechanics, deployment and first inspection

4.2.1 Mechanics

Differently from STRAW, for STRAW-b has not been possible to mount the entire string (cables plus modules) on one winch: the weight and the fragility of the VEOCs optical fibres forced us to find a different solution. So we decided, taking into account also the deployment technique to use (described in detail in paragraph 4.2.2), to separate the components and store the VEOCs plus the modules on a tray and the steel backbone on a which.
This solution turned out to be the safest one, considering the shipment to Canada and the pool test phase before the deployment.
The tray has been designed by Christian Spannfellner (more details on this can be found in his thesis [6]). The principal requirement was to host all the ten modules (including their mountings), the 10 VEOCs and the mini junc-

tion box (coupled to the string once the trey arrived in Canada). In addition, the tray has been designed to guarantee easy access during deployment. The minimum bending radius of the VEOCs optical fibre of $\sim$125mm has also been considered.

The tray has been produced by the TUM Physics Department Central Workshop and assembled by our team: in figures 4.5 and 4.6 are shown the technical drawing and pictures with the VEOCs spooled on it.

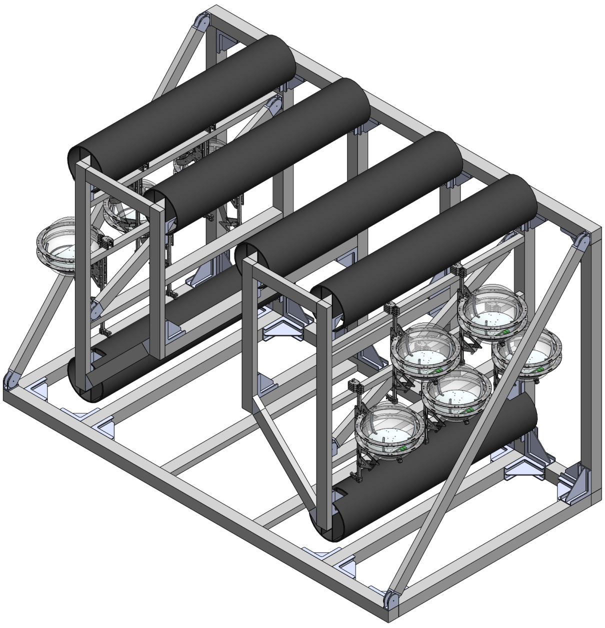

Figure 4.5: Technical drawing of the tray. Courtesy of Christian Spannfellner [6].

Figure 4.6: Picture of the tray with all 10 VEOCs spooled on it. Pictures courtesy of Christian Spannfellner [6]

The winch, instead, was one the two used for the deployment of STRAW: since the STRAW-b steel cable reel was bigger, it has been adapted accordingly using additional cylinders, see fig. 4.7.

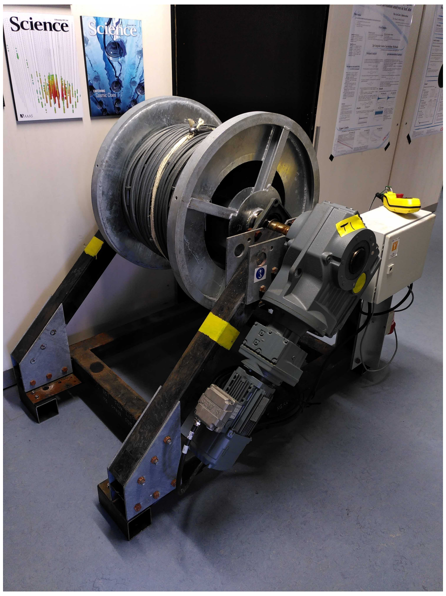

Figure 4.7: Picture of one of the two STRAW winches used for the spooling of STRAWb backbone steel cable. Pictures courtesy of Christian Spannfellner [6]

The qualification for all the components has been performed through specific vibration, shock and pressure tests. The goal was to verify their behaviour in the expected deep-sea conditions and the deployment stress.
A Standard Module and a prototype of the PMT spectrometer module have been tested according to the ISO 13628-6 standard at IABG[2]: *sine vibrations* with an amplitude of 2mm for the frequency range 5-25Hz and afterwards with an acceleration of 5g between 25-150Hz, and *shock vibrations* at 10g for eight times for all axis. Both modules passed the tests.
The pressure tests, instead, have been carried out at Nautilus. Even if the spheres were already rated for high pressure by the manufacturer (Nautilus itself), a second pressure test has been performed to exclude any possible effect of the connector holes. The module chosen for the test was repeatedly cycled to a maximum pressure of 375 bar in a specific pressure chamber [6]. Also, the pressure tests have been successfully passed by the module.

---

[2] Industrieanlagen-Betriebsgesellschaft mbH (IABG)

External module mounting

A fundamental part of the mechanics design has been defining how the modules glass spheres could be mounted firmly next to the steel cable. Hence different prerequisites needed to be satisfied by the module mounting:

- the design should have matched the already present ferrules on the steel cable;
- the field of view of the modules, in the upper part of the spheres, should not have been affected by the mounting shadows;
- the weight of the mountings should have been as light as possible, considering the handling of the modules by the crew during the deployment;
- the remarkable length of the VEOC cables connectors, around 20 cm, could have generated mechanical shocks on the glass spheres if not taken properly into account in the design.

After several iterations, the design chosen for the external module mounting has been the one illustrated in fig. 4.8. Around the sphere, two steel rings located 30mm above and below the equator hold it together with a layer of rubber edge protection (mounted in the final stage of the sphere assembly), squeezed enough to robustly hold the glass. On one side of the rings, a click-in mechanism ensures an easy connection to the ferrules of the steel cable without using any tools. This has been fundamental to have smooth deployment operations.

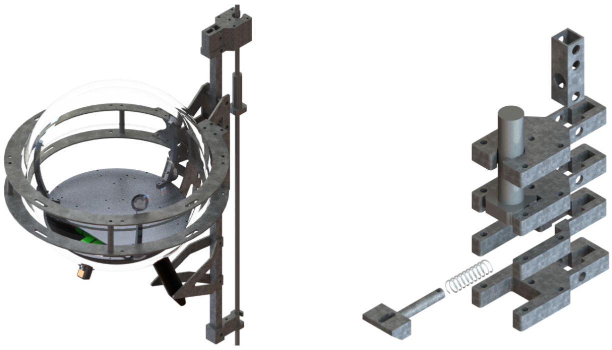

Figure 4.8: Technical drawing of the external mounting for a glass sphere module of STRAWb. Picture courtesy of Christian Spannfellner.

A lot of additional and more detailed information on the external mounting characteristics can be found in the thesis of Christian Spannfellner, as this part was also one of the topics he developed in detail [6].

4.2.2 Deployment and first inspection

Because of the VEOCs optical fibers fragility, the chosen deployment technique followed the *top-down* approach, similar to STRAW deployment (see paragraph 3.2.2). The overall operations complexity for STRAW-b has been greater compared to STRAW one. The reason is that the two structures that composed the string, the VEOCs and the steel cable (described in the paragraph 4.2.1), needed to be merged on the back deck of the vessel before laying the string on the water surface.
The buoys were deployed first and dragged far from the vessel by a *rigid-inflatable boat* (RIB), as in fig. 4.9.

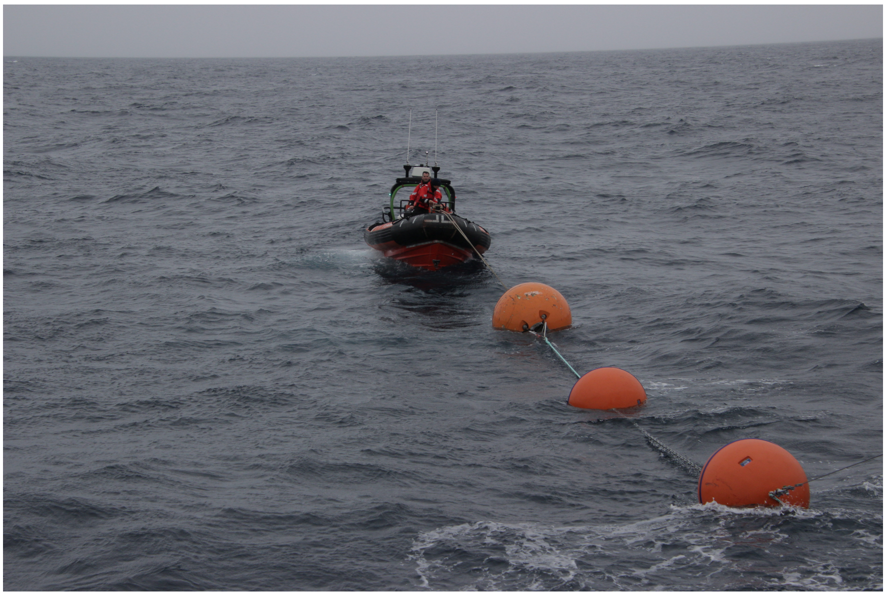

Figure 4.9: First phase of deployment operations: the buoys are dragged far from the ship to have the string well stretched on the sea surface. Credits to Will Glatt and Tammy Gomez (ONC).

Then, the ONC crew members started to couple the VEOCs to the steel cable while attaching the modules to the string (thanks to the click-in mechanism designed on purpose). At the same time, they started deploying the entire string into the water step by step accordingly. The picture in fig. 4.10 caught one of these very delicate steps.
Once the entire mooring was stretched on the sea surface, the anchor was lowered in the water by a heavy-lift line. When the mooring reached the vertical position, the anchor was disconnected by an acoustic release [6]. Then, the heavy-lift-line was connected to the buoys allowing the string to descend in a controlled way up to the seabed (speed $\sim$0.3m/s).

The visual inspection of the string and the connection to the junction box

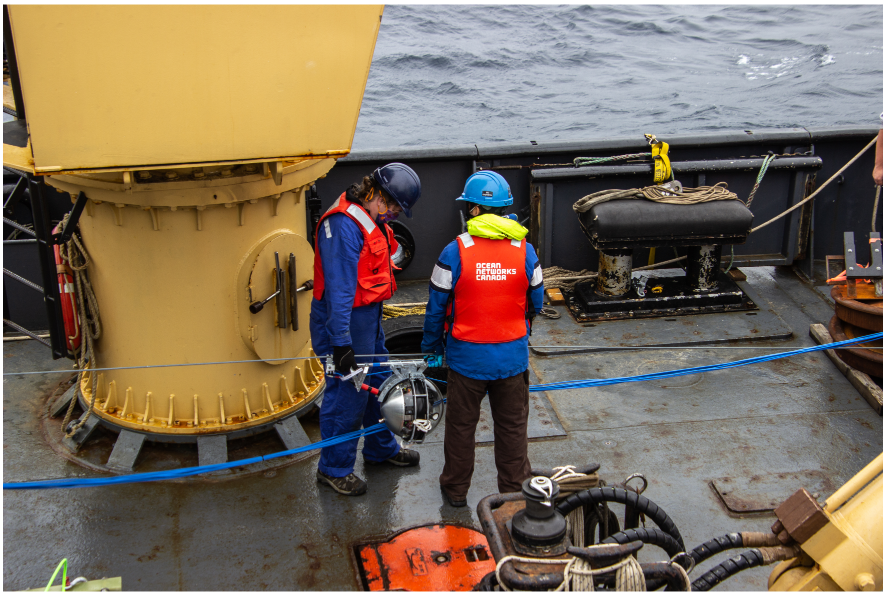

Figure 4.10: Picture taken during deployment operation: the crew members are connecting the module to the steel cable. Credits to Will Glatt and Tammy Gomez (ONC).

node were performed some days after the deployment, because of bad weather conditions. Firstly, to check if the modules showed some visible damage (potentially occurred during the descent), the ROV camera performed a very close visual inspection of the entire string. Some pictures are showed in fig. 4.11. After this stage, the ROV connected the string to the main junction box and the string was powered up.

All the modules were perfectly functioning except for the Standard Module at 2273m depth (384m on the VEOCs - see fig. 4.3) for which has not been possible switch on the electronics. The reasons are still under investigation, probably are linked to a broken connector at MJB.

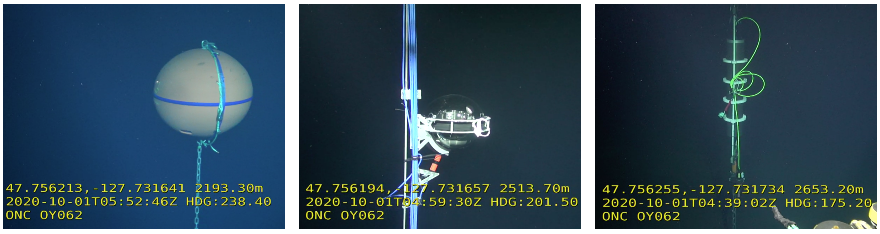

Figure 4.11: Pictures of STRAW-b from the ROV visual inspection after the deployment.

4.3 STRAW-b modules

The STRAW-b mooring hosts in total 10 modules that have been designed, assembled and tested by the TUM team. Three of them are defined as *Standard Modules* and seven of them as *Specialised Modules*, born for the implementation of completely different functions.
A detailed description will follow.

4.3.1 Standard Modules

The *Standard Modules* were born with the idea of being the "generalized modules", used as testing ground for components and electronics for the future P-ONE. Moreover, their electronics and internal modular mechanical substructure act like the base to which couple the Specialised Modules equipment and their electronic boards. Hence, the Specialised Modules can be considered like Standard Modules with a consistent upgrade.
Their principal function is to provide constant monitoring of pressure, temperature and humidity. In addition, they are used to check the positions of all the modules, using magnetic field sensors and accelerometers.

In view of the future P-ONE mooring design, as all other modules, the Standard Modules are integrated into a 13$''$ glass pressure housing produced by Nautilus [66] (optically enhanced borosilicate glass N-BK7 with a transmissivity $>$95% in the range between 350 nm and 600 nm).
To provide enough space for the Specialised Modules equipment, the readout electronics and the internal mountings needed to fit a minimum space inside the sphere. In the technical drawings in fig. 4.12 are shown the main parts:

- an aluminium bowl attached to one glass hemisphere by optical gel is used as a base (and for heat dissipation);
- a laser-cut aluminium plate, attached to the aluminium bowl, hosts the electronics that is mounted upside-down;
- three strives whose shape follows the radius of the sphere, keep in place the entire mechanical structure and the other half of the sphere thanks to the presence of suction cups at the end.

Such a glass sphere is closed and sealed by rubber edge protection (terostat) and adhesive tapes. On one side of the sphere, the presence of a vacuum port allows setting a very low internal pressure ($\sim$0.3 bar), beneficial for the seal tightness. Moreover, removing air and humidity in this way help to prevent the damage of electronic boards. Next to the vacuum port, there is the penetrator for the VEOC connector coupling.

The readout electronics of the Standard Module has been designed as a

Figure 4.12: Design of the STRAW-b Standard Module internal mechanics. The complete mechanical substructure with enclosed readout electronics is located 75mm below the sphere equator. Pictures courtesy of Christian Spannfellner.

customization of the STRAW sDOMs electronics, described in paragraph 3.4.

This system is based just on the *digital* and the *ethernet* parts, while the *analog* one is implemented only in the specialized modules, acting as front-end board for the different photosensors.

Similar to the sDOM electronics, also in the Standard Module electronics the *digital part* is composed by the standard Trigger Read-out Board (TRB3sc) [63], that implements the whole DAQ system with the *central trigger system* (CTS) and the *time-to digital converter* (TDC) in one FPGA.

Differently, the *ethernet part* is composed by an Odroid C2 computer and a new board called *Phobos* that establishes the connection between the Odroid and the TRB3sc. The Phobos hosts switchable power (DC/DC) converters, digital-to-analog converters, and analog-to-digital converters. Furthermore, on this board are implemented some environmental sensors and a monitoring system for the power consumption of voltage converters.

An additional board, named *Octopussy*, is responsible for converting the optical signals coming from the VEOCs into an ethernet format.

Besides, a dedicated system of redundancies is implemented to minimize

the effect of potential failures due to data transmission overload.
A picture of the boards assembly on the aluminium plate is shown in fig. 4.13, while a block diagram of the electronics for the Standard Module is shown in fig. 4.14.

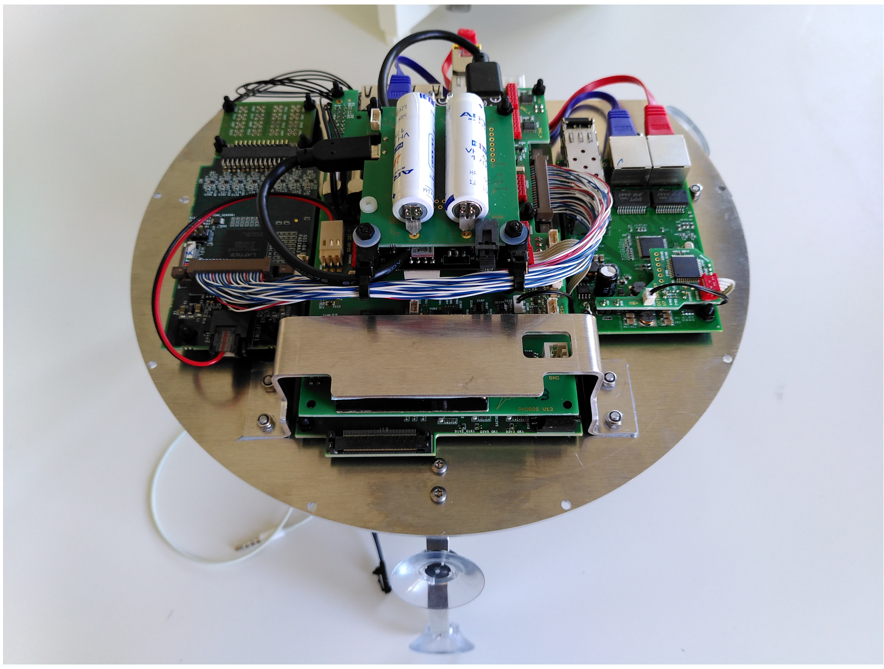

Figure 4.13: Assembly of the Standard Module electronics on the aluminum plate.

To have the possibility of checking the functionalities of the sensors and to add more measurements to the attenuation length, the electronics of some modules (muon tracker, both LiDARs and both PMT-spectrometers) has been provided with blue, white and UV LEDs looking downwards. Finally, all modules have been equipped with a battery-powered data logger (Uboot), aimed at monitoring the acceleration and the orientation of the full system during the deployment operations.
The entire readout electronics has been designed by Michael Böhmer (ZTL-TUM) in close collaboration with GSI in Darmstadt.

4.3.2 Specialised Modules

As already anticipated, the Specialised Modules were born to enrich the measurements obtained by STRAW, aiming at a full characterisation of the

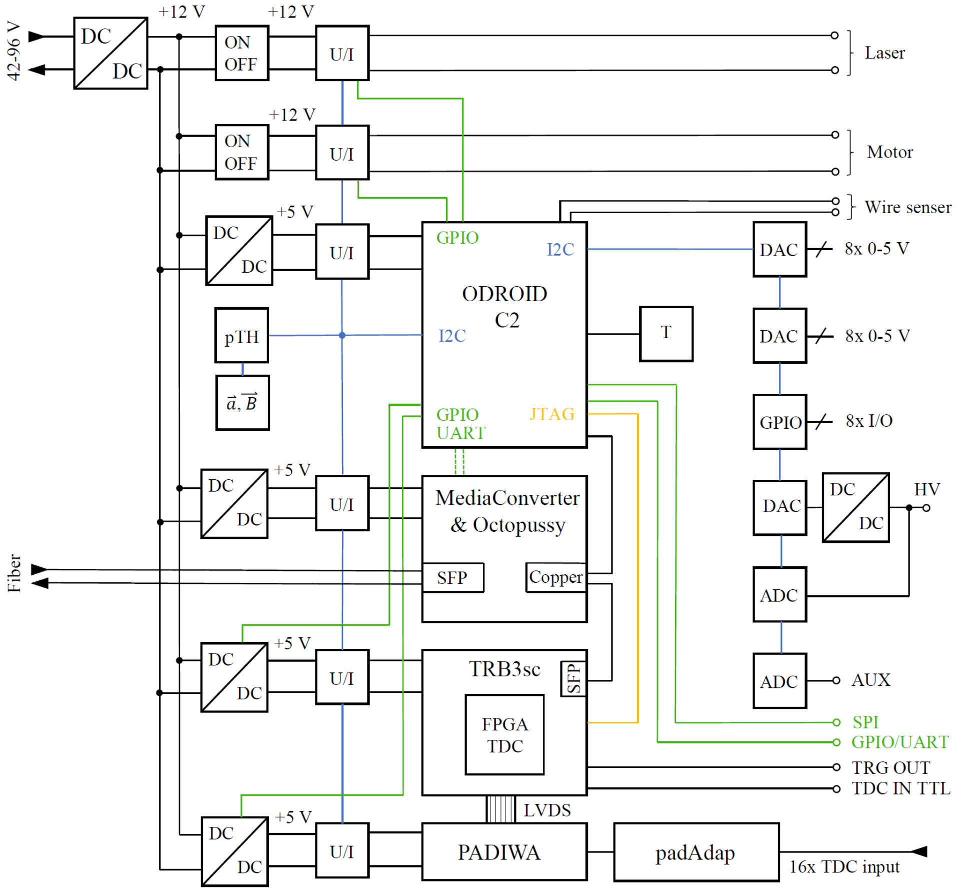

Figure 4.14: Block diagram of the electronics for the Standard Module. Picture courtesy of Christian Spannfellner.

optical properties and the light background of the Cascadia Basin site water.

One of the goals consists in new attenuation length measurements, discriminating between scattering and absorption lengths. The second one is the measurement of bioluminescence emission spectra, since in the past experiments, including STRAW, only the intensity of light background has been monitored.

Most of the Specialised Modules perform delicate optical measurements. Therefore, we decided to optimize the transmittance of light using optical enhanced glass upper hemispheres.

The LiDAR Module

The two LiDAR (Light Detection and Ranging) modules aim at measuring the attenuation length, complementing STRAW measurements. Besides their principal goal, they can even register, like all the other modules, parameters and status information like the Standard Modules.

This alternative approach for attenuation length measure makes use of short 450nm light pulses of $\sim$10ns, emitted from a pulsed laser diode beam (ThorLabs, NPL45B). The optical receiving system detects the back-scattered light: a lens with a narrow-band filter for the laser wavelength focuses the light into a μPMT (Hamamatsu, H12406), which measures the light intensity as a function of time.

The optical assembly is mounted on a motorized gimbal that allows the LiDAR to scan the entire $\sim 2\pi$ sr upper hemisphere. Thanks to a self-calibration system, the laser light intensity can be monitored by a silicon photodiode, while the laser wavelength is constantly calibrated with a mini spectrometer device (the same type as mounted in the Minispectrometer Module, paragraph 4.4).

Moreover, since the two LiDAR modules host two ultra-bright, downward-pointing *Lucifer* LED boards (broad-spectrum white LED and UV LED), it is possible to calibrate the two PMT spectrometer modules placed directly below them. The LEDs emission range matches perfectly the detection range of PMTs.

In fig. 4.15 is shown a picture of one assembled LiDAR module with its technical drawing for the internal mounting.

The PMT-spectrometer Module

With STRAW modules, and in general with any other digital optical neutrino telescope module so far, it has been possible to detect and measure only the background light intensity but not the light spectrum. With the two STRAW-b PMT spectrometer modules, instead, the main goal is to characterize the bioluminescence background light spectrum.

Each module hosts twelve PMTs coupled to focusing lenses (ThorLabs N-BK7 Plano-Convex Lenses with AR Coating: 350-700nm) and different wave-

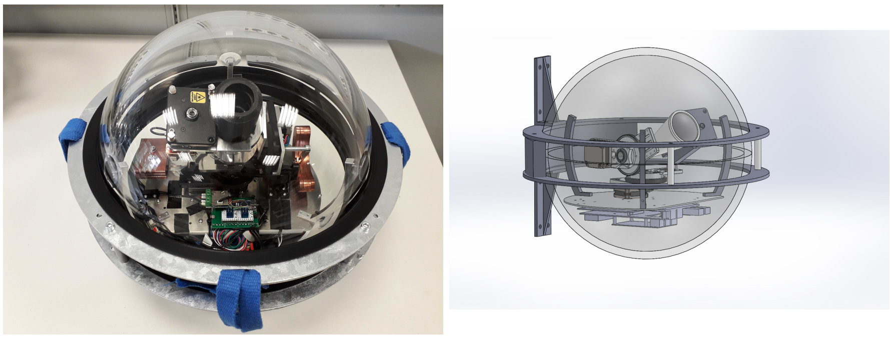

Figure 4.15: **Left**: Frontal picture of one of the two LiDAR modules before shipping them to Canada. **Right**: Technical drawing of the internal LiDAR module assembly. Courtesy of Laszlo Papp.

length filters (Edmund Optics Hard Coated OD 4.0 Bandpass Filter from 350 to 550nm, nominal FWHM from 10 to 50nm) to detect light according to the expected bioluminescence emissions [67], see paragraph 5.1.5.

Two different PMTs have been adopted: R1924A and R1925A, both produced by Hamamatsu. The R1924A has a greater quantum efficiency at short wavelengths: for this reason, it has been coupled to short-wavelength optical filters. The R1925A instead has been coupled to longer wavelengths optical filters.

The internal module PMTs support structure has been designed by Kilian Holzapfel and 3D printed with an Ultimaker3: it consists of four equal substructures, each hosting three PMTs, three lenses and three filters. This structure aligns the PMTs to the same field-of-view taking into account differences due to their arrangement and refraction [6].

To take pictures of bright bioluminescence events or bioluminescence organisms approaching the modules, a compact astronomy camera (ZWO Kamera ASI294MC Color, 4/3″, 19.1mm x 13.0mm, ~11M pixel), connected to the Odroid by USB 3.0 port, has been installed at the centre of the PMT support structure.

In fig. 4.16 is shown a picture of one of the final assembled PMT spectrometer module and one of its technical drawings. Details on the PMT spectrometer module design, tests of all the components and assembly has been described by Li Ruohan in her master thesis [68].

The Muon Tracker Module

One of the fundamental reasons for building a neutrino telescope at big depth underwater is to exploit the water mass as a veto for atmospheric muon flux. A sufficient depth can highly reduce this source of background, discriminating, in particular, those muons that are mis-reconstructed as up-going.

The muon flux in the deep ocean has been well studied in the last years

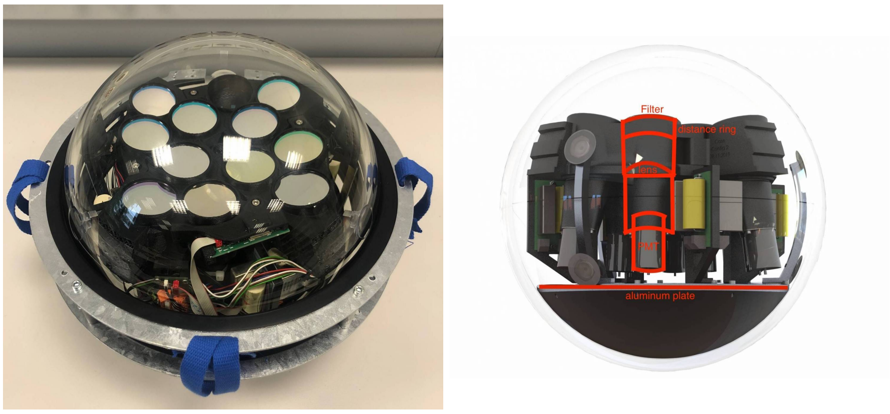

Figure 4.16: **Left**: Frontal picture of one of the two PMT spectrometer modules before shipping them to Canada. **Right**: Technical drawing of the internal 3D support structure designed by Kilian Holzapfel.

by different underwater experiments. The STRAW-b Muon Tracker aims to confirm these measurements in the deep Pacific Ocean.
The module uses two scintillator planes (BC-404, Saint Gobain) that generate photons when a passing muon deposits some of its energy interacting with the material. The emitted light is then detected by Silicon Photomultipliers (SiPMs) arrays (PM3315-WB-B0, Ketek).
The scintillators are mounted inside two housing boxes (held at 10 cm distance by threaded bars) composed by a Teflon frame (allowing a matrix of 2x2 scintillator tiles) with an outer thick aluminium layer: a reflective foil, placed between the scintillators and the aluminium layer, combined with the Teflon diffusion effect, assures that most of the light reaches the photosensors.
Each SiPM array consists of 9 SiPMs, directly coupled by optical gel to the

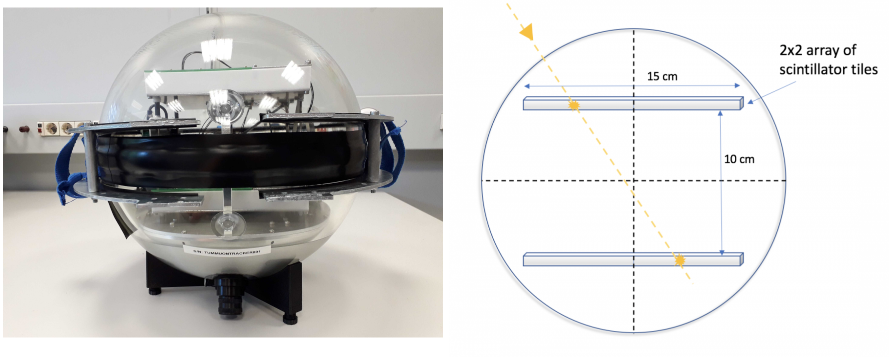

Figure 4.17: **Left**: Picture of Muon Tracker Module completely assembled. **Right**: Technical sketch of the working principle for muon detection.

scintillator surfaces, thanks to cut-out windows on the upper and lower opposite corners of the aluminium plates.
Since other charged particles can deposit energy into the scintillators and consequently generate unwanted signals, only time coincident signals in the two different scintillator planes are counted as muon events. This is sufficient to discriminate between background radiation and muons.
In the fig. 4.17 it's shown a picture of the Muon Tracker in the final configuration and a technical drawing representing its working principle.
More details about the development and the design of this module can be found in the thesis of Eva Laura Winter [69].

The Wavelength Shifting Optical Module (WOM)

The Wavelength shifting Optical Module (WOM) has been developed for the IceCube Upgrade by the Johannes Gutenberg University of Mainz, Germany.
Typically, the spheres adopted in neutrino telescopes are opaque to the UV radiation, as the glass cuts out the wavelengths <330nm. The goal of the WOM is to detect UV photons, thanks to its external housing made of quartz, that is transparent to these wavelengths. In this way, unexplored deep-sea background light wavelengths can be detected.
The external quartz cylindrical tube high-pressure resistant housing (Nautilus) hosts a smaller cylinder, coated with a wavelength shifting optical paint. In this way, the incident UV photons get absorbed and re-emitted in the visible range. This radiation can be easily detected by two PMTs (Hamamatsu R14689 3.5″ bialkali), coupled to the internal cylinder with an optical glue (NOA61). The space between the inner tube and the outer one is filled with a material with a proper refractive index (hydrogel, n=1.33).
This working principle is represented in fig. 4.19 while in fig. 4.18 there is a picture of the assembled module.

Figure 4.18: Picture of the WOM: the detector is illuminated by UV light to show the fluorescence of the wavelength shifter. Courtesy of JGU Mainz group.

The Minispectrometer Module

The realization of the Minispectrometer Module has been another significant part of my PhD project.

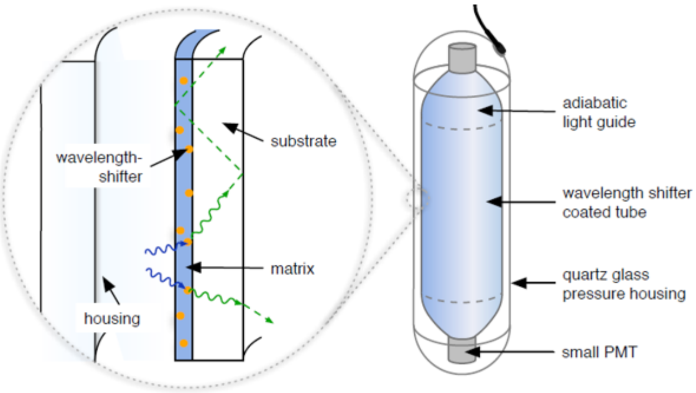

Figure 4.19: Sketch of the WOM working principle. Courtesy of JGU Mainz group.

My work covered all the stages of the development process: design, prototyping, integration, calibration and test. All these steps will be extensively described in the next paragraph 4.4.

4.4 The Minispectrometer module

The idea of building a module that could measure the spectrum of deep-sea light background was born immediately after the visual inspection of STRAW moorings, one month after their deployment. The check, indeed, revealed the presence of several *Pyrosomes* entangled into the strings cables (as described in detail in paragraph 5.8).
Thanks to the STRAW experiment, it has been possible to collect long-term information about bioluminescence emission rates (paragraph 5). So far, no information is available from literature about bioluminescence emission spectra measured in-situ. Generally, the light emission of deep-sea organisms has been measured in the laboratory [70], quite far from their original environment. This could, in principle, influence their light emission.
An optical module able to measure the light spectrum can add new discriminating constraints in the background analysis and provide useful information about the bioluminescent burst emission mechanisms.

STRAW-b hosts two different modules for light spectrum measurements: the PMT-spectrometer Module (already described) and the so-called *Minispectrometer Module*. Both modules are able to detect light and analyse wavelengths, but their different sensitivity makes their measurements complementary. Indeed, the PMT is sensitive to single photons and has a linear response up to a couple of hundreds of photons before saturating. On the other side, as described in the following paragraphs, the minispectrometer device has a higher dynamic range. For this reason, the goal of the PMT-spectrometer Module is to detect faint diffused light, while the Minispectrometer Module is focused on detecting bioluminescence bursts.

4.4.1 The light sensors

The idea behind the working principle of the minispectrometer module is represented in the sketch in fig. 4.20. The light emitted by a deep-sea organism in the vicinity of the module is transmitted through the glass sphere, where it finds a detector able of separating individual narrow bands of colour.

Following this idea, after an extensive investigation phase, I decided to build the module using a combination of commercial devices, in order to have a high reliability over time.

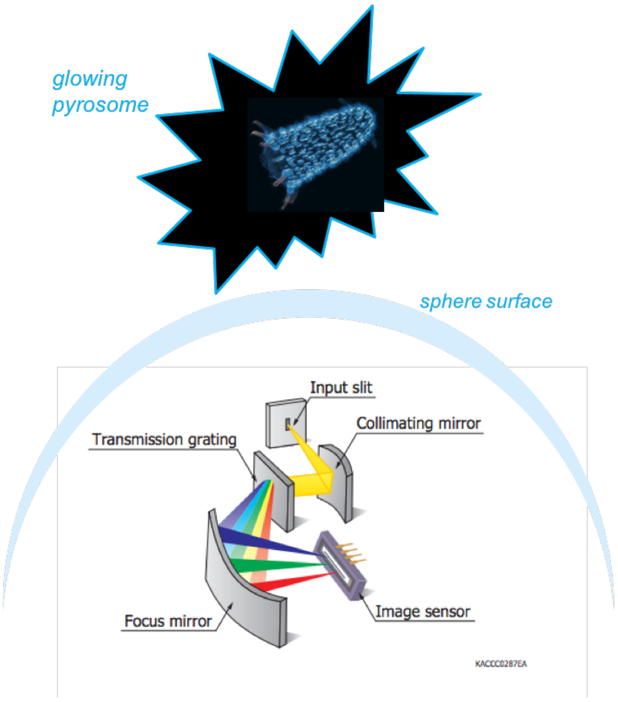

Figure 4.20: Sketch of a minispectrometer working principle.

After a long investigation, the chosen device has been the Hamamatsu minispectrometer C12880MA, fig. 4.21: very compact (size: 20.1 x 12.5 x 10.1mm, weight: 5g) and hermetic for high reliability against humidity. It is equipped with a high-sensitivity CMOS linear image sensor, composed of 288 pixels. The spectral range response goes from 340 to 850 nm, with a spectral resolution of 15 nm. Each device is pre-calibrated by the manufacturer. The absolute wavelength λ is related to the pixel number p by the following fifth-order polynomial

$$\lambda = A_0 + B_1 p + B_2 p^2 + B_3 p^3 + B_4 p^4 + B_5 p^5. \tag{4.1}$$

The light is collected through a 50 x 500 μm input slit with a numerical aperture of NA= 0.22. For this reason, no optical fibre is needed. An alternative solution (discarded for this application) could be represented by the Hamamatsu C12880MA-10 device, mounting an SMA connector for optical fibre coupling. The internal configuration is represented in the sketch in fig. 4.22: besides a CMOS image sensor chip, the C12880MA uses a reflective concave blazed grating formed by nanoimprint. The Hamamatsu evaluation board C13016, connectable directly via USB to a PC and provided with a dedicated software, makes this device ready to be tested and used. The integration time can be set in the range between 11μs and 1s. The digitized output signal vs wavelength is expressed in ADC counts, as shown in the software window caption in fig. 4.23. The manufacturer does not provide any calculation factor for converting the ADC counts into the input light levels. Therefore, a detection sensitivity study has been performed during the test phase. In particular, the low light level regime has been characterised.

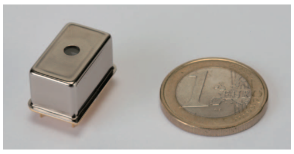

Figure 4.21: Picture of Hamamatsu minispectrometer C12880MA.

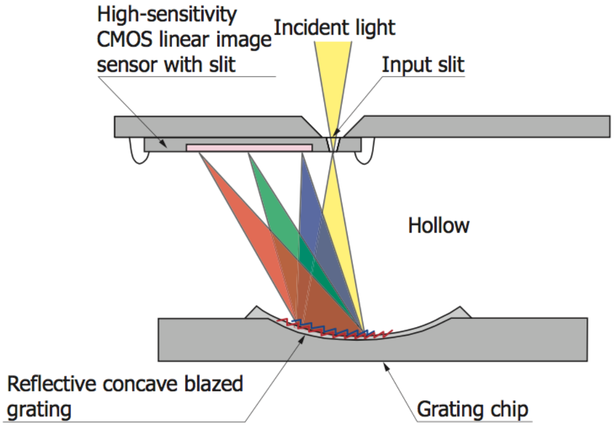

Figure 4.22: Sketch of the internal configuration and working principle of the Hamamatsu C12880MA minispectrometer.

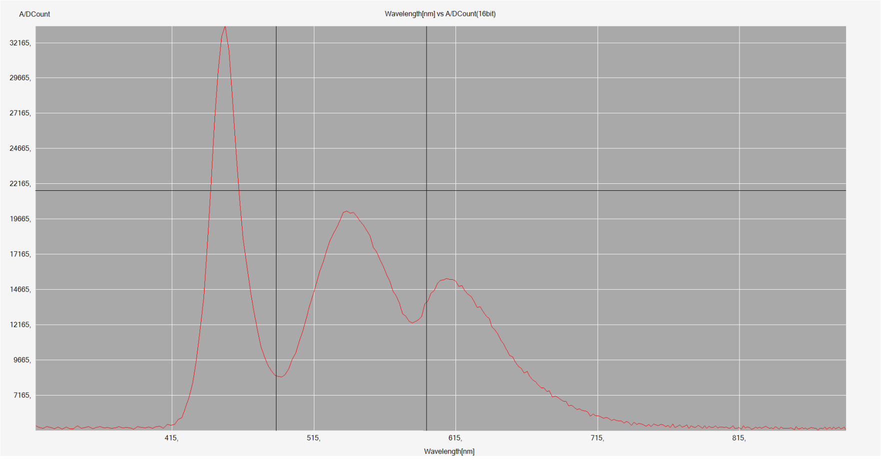

Figure 4.23: Example of measurement: cold white lamp light detected by a minispectrometer device and displayed in real time thanks to the evaluation software.

4.4.2 Selection phase tests

As described in the previous section, Hamamatsu can provide two minispectrometers of the C12880MA type: one with an SMA connector that allows an optical fibre, called C12880MA-10, and another without, called C12880MA (see fig. 4.24).

During the selection phase of the candidate spectrometers, I tested both solutions in order to study any differences in light collection efficiency and detection. In addition, the mounting design and the optical fibre coupling with the 13″ glass sphere that will host the Minispectrometer Module have been evaluated. For the final choice, also stability during deployment has been considered.

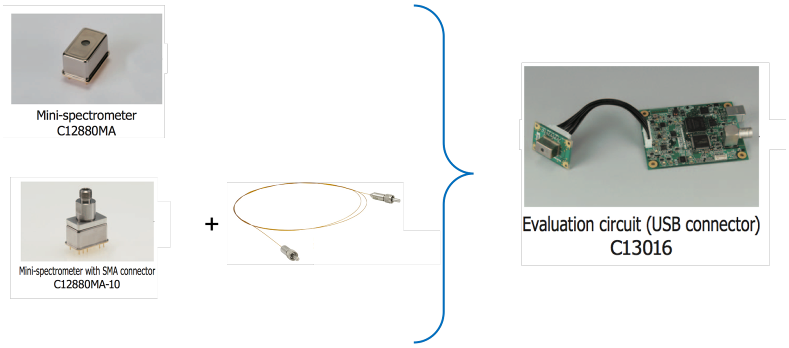

Figure 4.24: Picture of the two Hamamatsu minispectrometer considered in this study.

In order to choose the best solution, I started with testing the response of the two devices at different distances from a light source, for different light intensities and different wavelengths.
As a light source, I used the LED matrix from the POCAM module, coupled to its PTFE sphere, having an isotropic light emission. In particular, the LEDs used have been the UV 365±8 nm, the blue 465±7 nm and the orange 605±6nm, as described in paragraph 3.3.
Each LED has been flashed at 10 kHz and powered at different HV to modulate the light emission:

- the 365 nm LED at 22.5 V
- the 465 nm LED at 7.5 V, 8V, 9V, 10V
- the 605 nm LED at 6V, 9V, 20V

For each *LED-HV* light configuration, the investigated distances from the light source have been: next to the sphere, at 5cm, at 10cm, at 15cm and 20 cm from it.
The tests have been performed in a dark box, at room temperature, by aligning the centre of the PTFE sphere source with the C12880MA spectrometer input slit centre, and in the second test phase with the centre of the optical fibre coupled to the C12880MA-10, as shown in fig. 4.25.
Thanks to the Hamamatsu software, the data-taking has been straightforward. It allowed first to set, for each spectrometer, the conversion parameters for the right calibration of the pixels in wavelengths and, second, to set the integration time (that for these tests has been fixed at 1 s).

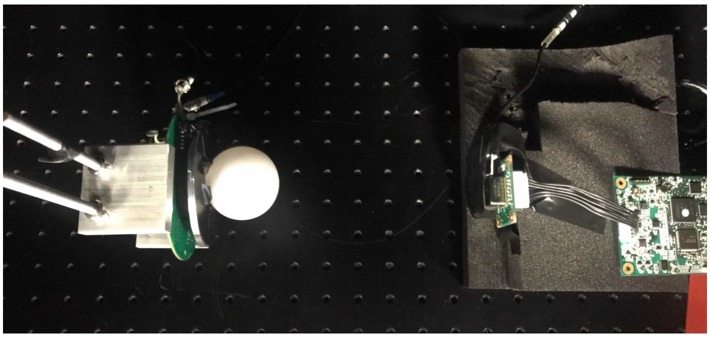

Figure 4.25: Setup used for testing light detection of the C12880MA and the C12880MA-10. The POCAM integrating sphere coupled with the LED matrix, is used as a light source. The C12880MA minispectrometer and the optical fibre of C12880MA-10 are aligned. Picture courtesy of Nikhita Keera.

For each measurement, two *.csv* files have been saved. One contains a *dark spectrum*, represented by the ADC counts measured by each of the 288 pixels in the dark run. The other contains the *light spectrum*, with the ADC counts proportional to the light detected.
These data have been used for the dark subtraction implemented in later

stages of the analysis.
An example of the analysed data is shown in fig.4.26. In the upper part, there is the dark spectrum. In the centre, the light spectrum (without the dark subtraction). In the lower part, there is the final light spectrum after the dark subtraction. Since LEDs are moderately narrow band emitters with an approximately gaussian spectral shape, the light spectrum detected is exactly a gaussian distribution.

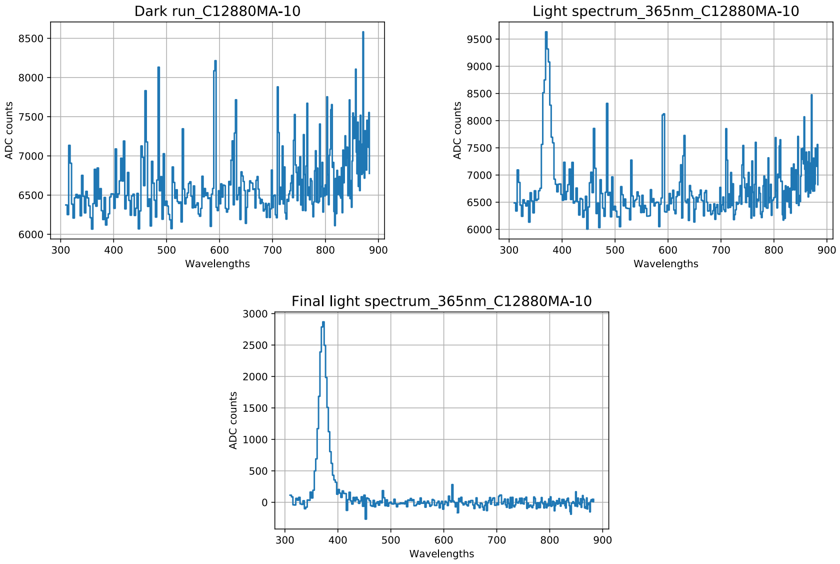

Figure 4.26: Example of data collected by one spectrometer. In this case, the light source used has been the LED 365 nm from the POCAM. The spectrometer under investigation was the C12880MA-10, with an integration time of 1s.

Following the approach described above, I collected all the data files, for both minispectrometers, taken in every mentioned layout of light.
In particular, after the dark subtraction, I considered the *total amount of light detected* as the integral of the ADC counts and the *resolution* as the FWHM of the gaussian distribution.
For each *LED-HV-distance* configuration, I plotted both spectrometers results (in fuction of the distances) on the same graph, as in fig. 4.27, 4.28 and 4.29.

It is not immediate to determine the best sensitivity configuration: for short light source-spectrometer distances, the C12880MA spectrometer appears to be slightly more efficient than the fibre C12880MA-10 spectrometer. Anyway, at longer distances, the fibre C12880MA-10 spectrom-

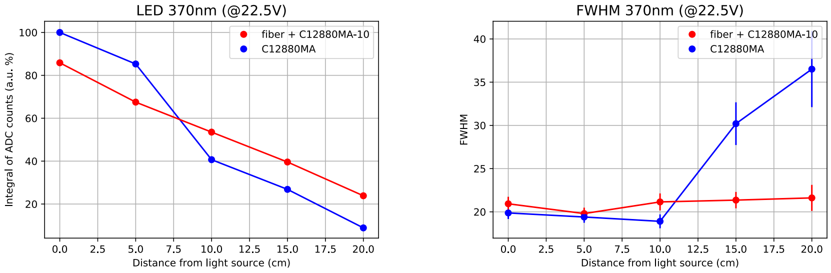

Figure 4.27: Example for the LED at 370nm powered at 22.5V. **Left**: Light spectrum ADC counts versus distances. The error bars are too small to be visible in the plot. **Right**: FWHM of each ADC gaussian distribution represented in the plot on the left.

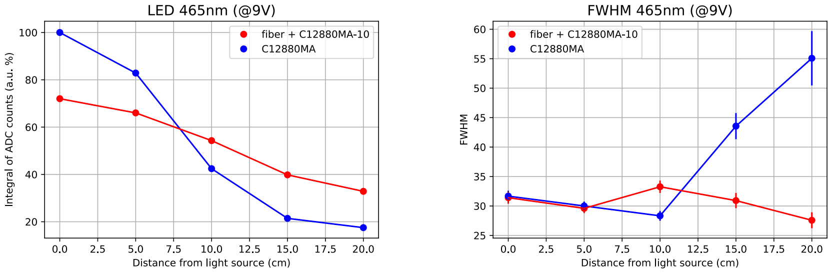

Figure 4.28: Example for the LED at 465nm powered at 9V. **Left**: Light spectrum ADC counts versus distances. The error bars are too small to be visible in the plot. **Right**: FWHM of each ADC gaussian distribution represented in the plot on the left.

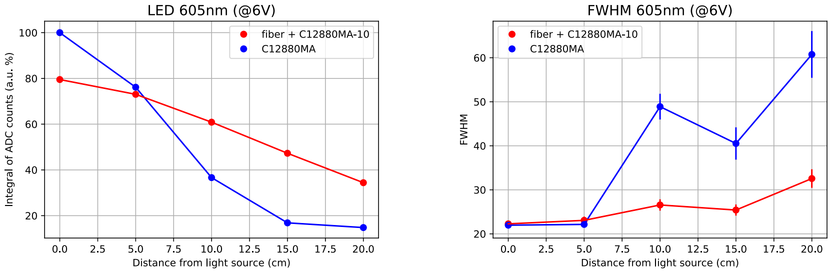

Figure 4.29: Example for the LED at 605nm powered at 6V. **Left**: Light spectrum ADC counts versus distances. The error bars are too small to be visible in the plot. **Right**: FWHM of each ADC gaussian distribution represented in the plot on the left.

eter collects more light with a better resolution, despite the intrinsic attenuation and insertion loss. It must be considered, however, that the distance from the light source affects the photon incident angle and, consequently, the detection of the devices. At lower distances, the incident angles are wide and the collection efficiency of the bare C12880MA slit turns out to be

higher. On the contrary, increasing the distances, the fibre C12880MA-10 is more efficient. The inversion point in the plots on the left can be strictly connected to this aspect.
Therefore, I performed additional tests, fixing the position of both spectrometers with respect to the light source at 15 cm. This value has been chosen considering the dimension of the glass housing. In particular, it corresponds to the minimum distance of the sensors from a deep-sea bioluminescent organism. In this way, the incident angle on both devices was fixed: the only free variable was the light intensity.
Since the maximum attenuation length in water is in the range of 420-470 nm [71], I focused this test on the LED 465nm, powered from 7.5V to 20 V in steps of 1V. To monitor the POCAM light emission, I used a photodiode as a reference.
In fig. 4.30 becomes clear that in the same configuration of LED-HV at a mean distance from both sensors, the fiber+C12880MA-10 solution is more efficient; moreover, for low light level, its resolution is up to 40% better compared to the C12880MA bare spectrometer.

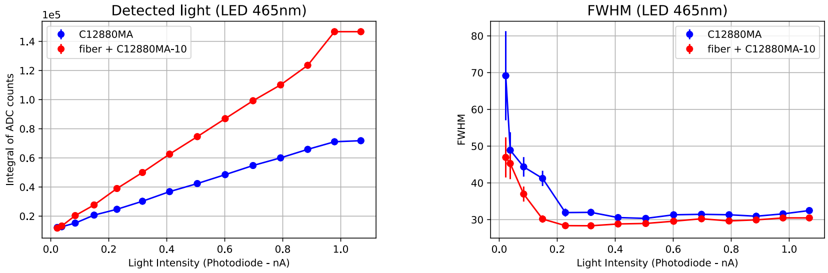

Figure 4.30: Detection test at 15 cm from the light source (POCAM LED 465nm). **Left**: Spectrometers light spectrum ADC counts versus photodiode current. The error bars are too small to be visible in the plot. **Right**: FWHM of each ADC gaussian distribution represented in the plot on the left.

At this point, which spectrometer is more suitable for STRAW-b purposes?
Even with the same field of view (NA), the bare spectrometer C12880MA appears to have a wider angular detection efficiency range with respect to the fibre one, as expected. The collection efficiency of the fibre one turns out to be higher at smaller incident angles (at longer distances from the source), with a better resolution all over the investigated range.
Even if the fiber+C12880MA-10 seems to have better overall characteristics, robustness and mechanical stability played a decisive role in the final decision. Budget constraints and mechanical stability led to the decision to opt for the most stable solution, the bare minispectrometer C12880MA, and to think of a mechanical structure that would bring the minispectrometers as close as possible to glass (as described in the paragraph 4.4.3.

4.4.3 Electronics and internal mounting

For the design of the Minispectrometer Module, two aspects have been considered: the coverage of a broad field of view with different minispectrometers, mounting them as close as possible to the sphere glass surface, and the electronics ability to host a fixed number of components.

The Minispectrometer Module *electronics* includes five mini-readout board, a board with multiplexer functions and the common electronics as in the other modules (PHOBOS board, TRB3sc board, Octopus board, DATA LOGGER), all customised by Michael Böhmer (ZTL-TUM).
In order to add several minispectrometers plus a camera and handle them properly, the SPI multiplexer board named "Bridgette" acts as an intermediary between the mini-boards and the common electronics part. The Bridgette board could implement only six SPI ports. For this reason, the multiplicity of the minispectrometers was limited to five.
The five Hamamatsu minispectrometers are coupled to mini-readout boards, see fig. 4.31, designed on purpose since it was not possible to use the manufacturer electronics because of different OS compatibility: STRAW-b has Linux-based electronics, while the Hamamatsu PCB is compatible only with Windows machines.
The main components of the mini-board are: +5V power for the minispectrometer, a DC/DC converter, a JTAG+FPGA, a SPI, an ADC and a temperature sensor. The FPGA generates the entire board necessary signals and allows to set a very long integration time for the CMOS sensor in case of reduced dark current by low temperature. The collected data from the minispectrometer are first digitized and stored in the FPGA and then forwarded to the SPI port.

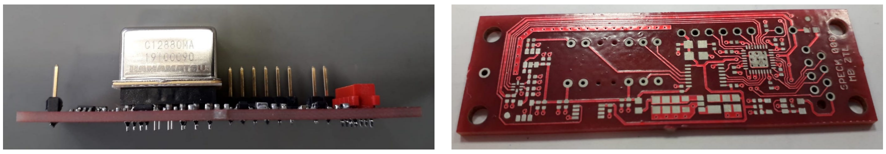

Figure 4.31: Picture of the customised prototype mini-readout board for the Hamamatsu minispectrometer, designed by Michael Böhmer. **Left**:side view. **Right**: top view.

The Minispectrometer Module electronics has two SPI communication interfaces, that are used for data-taking and status reading. The software used at this scope is the *mctl* (master control) software, developed on purpose by the TUM team and written in object-oriented Python, that simplifies the data acquisition process and makes it more user-friendly [68]. The calibration values for the pixels/wavelengths conversion (for each mounted device) have been included in the *mctl* software version for the Minispectrometer Module, to have consistent data output.
The data file output is in HDF5 format and contains the readout data for all

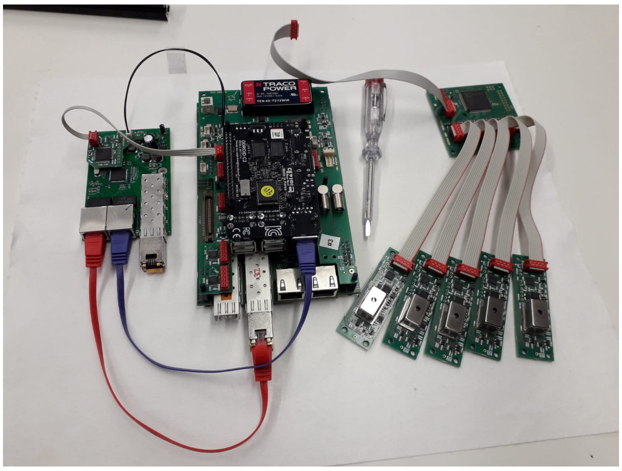

Figure 4.32: Final Minispectrometer Module electronics assembly. The 5 Hamamatsu devices are coupled to the five mini-readout boards, connected to the Bridgette board. During the module mounting, the Bridgette has been connected to the TRB3sc board through a hole drilled in the aluminium plate that hosts the entire common electronics, see paragraph 4.3.1.

five minispectrometers for each measurement. The complete electronics with mounted devices is represented in fig. 4.32.

The Minispectrometer Module *internal mounting* has been designed by Laszlo Papp, combining mechanical stability and minimal distance of the spectrometers from the glass.

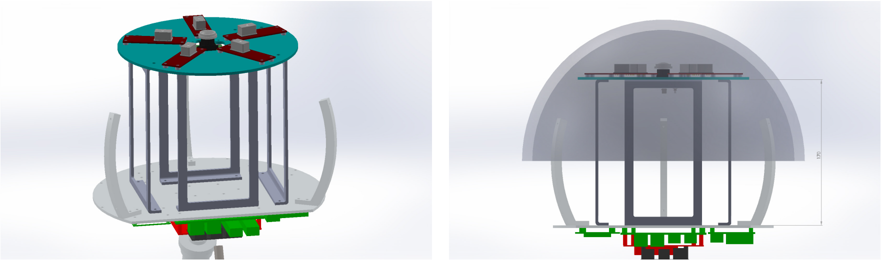

Figure 4.33: Technical drawings of the Minispectrometer Module internal mechanics. Courtesy of Laszlo Papp.

The holding structure is composed of one aluminium plate (20 cm diameter) and four bent aluminium rectangular frames of 17 cm height (see fig. 4.33). The frames are screwed to both the lower cooling plate, which hosts the common electronics, and the upper aluminium plate, hosting the five minispectrometers with their mini-readout boards and the camera. The camera and the slits of the spectrometers are aligned at the same distance from a potential light source. The final assembly of the internal mounting with the sensors is represented in fig. 4.34.

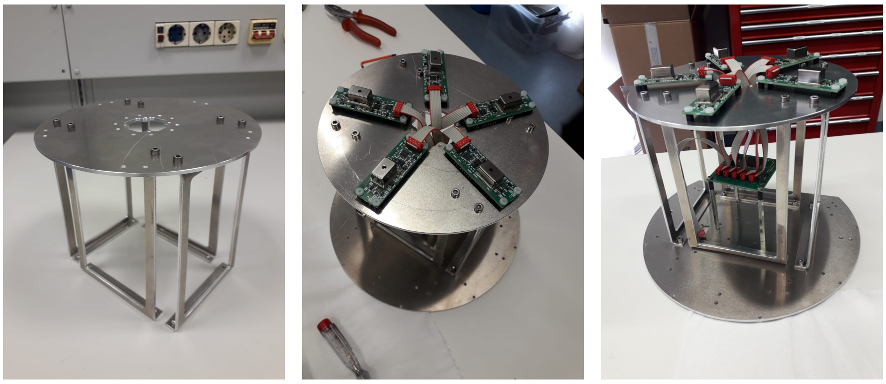

Figure 4.34: Final assembly of the Minispectrometer Module internal mounting. On the right picture is visible that the "Bridgette" board is fixed between the two aluminum plates with four spacers screwed on the bottom plate.

4.4.4 Dark calibration tests

The final configuration of the Minispectrometer Module is shown in fig. 4.35.

As the radiation coming from the decay of the ^{40}K present in the glass can add an extra offset to the dark counts level (caused by internal heat) of the minispectrometers, I tested the entire module in the dark controlled temperature chamber in order to characterize it in different dark configurations and collect all the data. This measurement allows identifying the right dark subtraction for the future offline analysis.

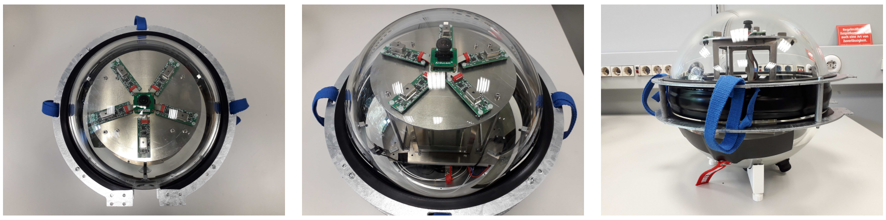

Figure 4.35: Top and side view of the Minispectrometer Module final assembly.

The temperatures tested have been from 0°C to 35°C in steps of 5°C. For each temperature, different integration times have been set: 0.1s, 0.5s, 1s, 5s, 10s, 30s, 60s, 90s, 120s. It is not possible to predict in which light conditions the module will work once deployed and if it will be necessary to set different integration times accordingly. For this reason, it turns out to be beneficial to have a wide range of dark configuration data collected.

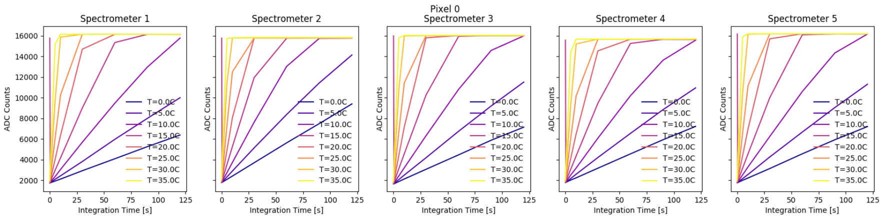

Figure 4.36: Example of dark response for pixel number 0 (of all minispectrometers) in function of integration time windows and external module temperatures.

In the plot in fig. 4.36, for each minispectrometer, is represented an example of the dark response of pixel number 0: on the y-axis there are the ADC counts, on the x-axis there are the different integration time windows; each line represents the different temperatures. The trends confirm a good linearity in response at low external temperatures and over the entire range of integration times. This information is available for all 288 pixels of each minispectrometer.

Choosing one external temperature and one integration time, an example of the dark spectrum for the entire module is shown in fig. 4.37. Ideally, after a deep-sea run, these are the dark levels to subtract in order to look for evidence in the detected light spectrum.

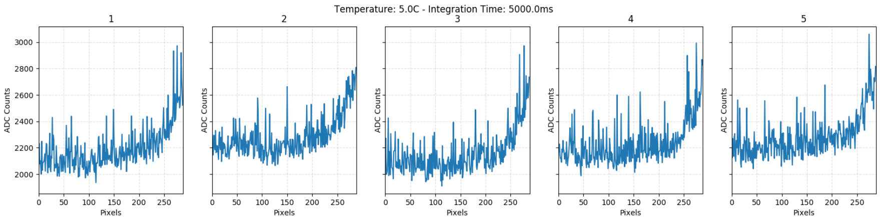

Figure 4.37: Example of dark spectrum for calibration: the external temperature is 5°C and the integration time is 5s.

During this calibration phase, the internal temperature (measured by sensors mounted on the mini readout board of each minispectrometer) was $\sim$9°C higher than the external one. Therefore, for the correct dark subtraction in the offline analysis, the proper calibration data file must be selected comparing the internal temperature during tests and the one measured during the deep-sea data-taking.

4.4.5 Last functional tests

After the final assembly and before shipping to Canada, the entire module has been subjected to the last functional tests.

This step has also been the right occasion to draw up the *Minispectrometer functional test procedure*, needed to the Canadian team responsible

for testing again the functionalities of every module once delivered at ONC. The five minispectrometers and the camera have been tested in the dark box using the POCAM integrating sphere coupled to the LED matrix.
In fig. 4.38 is shown how the output file containing all five minispectrometer data can be represented. In particular, this plot corresponds to one of the tests performed with a POCAM LED (the 465 nm one). In fig. 4.39 are shown, instead, some pictures taken with the camera: the different POCAM LEDs illuminating the entire integrating sphere can simulate quite well possible deep-sea bright light sources.
In this framework, the readout software has also been tested one last time to check for any left bugs.

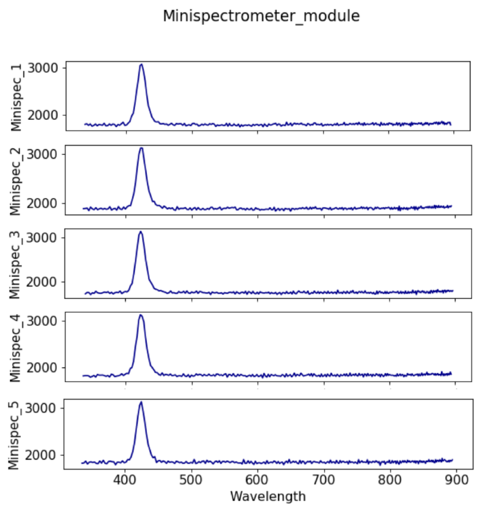

Figure 4.38: Minispectrometers data taken during the last fuctional test phase with the POCAM. Here is represented the emission of LED 465nm. On the y-axis there are the ADC registered by the sensors while on the x-axis there are the wavelengths.

4.4.6 First Minispectrometer Module data

Some days after the deployment (see paragraph 4.2.2), the entire string was powered up. Some basics tests were performed to check the functionalities of all the modules and to exclude any possible damage during the descent to the seafloor.
The Minispectrometer Module was perfectly functioning. In addition, during the visual inspection phase, I exploited the ROV light to perform the first deep-sea measurements.
In fig. 4.40 it is shown the spectrum of the ROV light detected by the module.

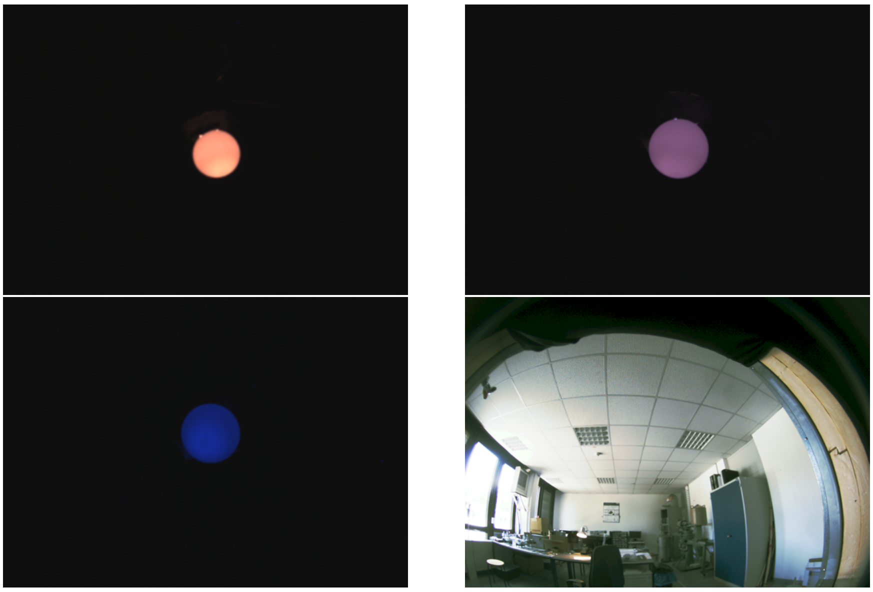

Figure 4.39: Picture taken with the camera of the Minispectrometer Module. Different LEDs of the POCAM are visible. In the bottom right, the picture has been taken from the inside of the dark box to our laboratory room in Garching.

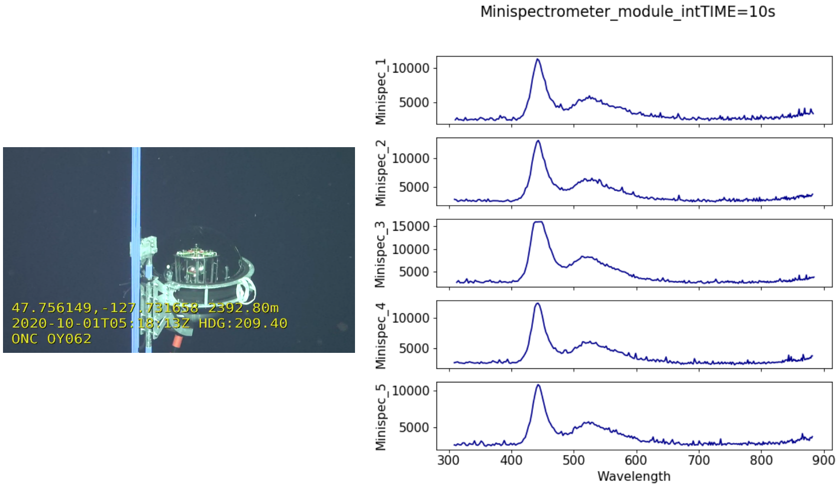

Figure 4.40: **Left**: Picture of the Minispectrometer Module illuminated by the ROV light, taken during the visual inspection. **Right**: Spectrum of the ROV light measured within 10 s integration time windows. It is pretty clear the beginning of the saturation for the spectrometer number 3, that detects more light with respect to the other because was the most exposed to light.

The integration time of the five minispectrometers and the time window between two following measurements are variable parameters. For this reason, the data taking can be adapted to the environmental conditions. An initial investigation phase (still ongoing) can help to evaluate the right working point to set for the sensors.
In fig. 4.41 is shown an example of one deep-sea measurement taken using an integration time window of 60 s. Apparently in the first plot no particular excess is visible in the spectrum, if compared to the calibration dark data. Applying then the right dark subtraction (using the corresponding internal temperature calibration dark file from the ones collected previously in the laboratory), a variation of the signal over dark can be seen in the minispectrometer number 5, fig. 4.42.

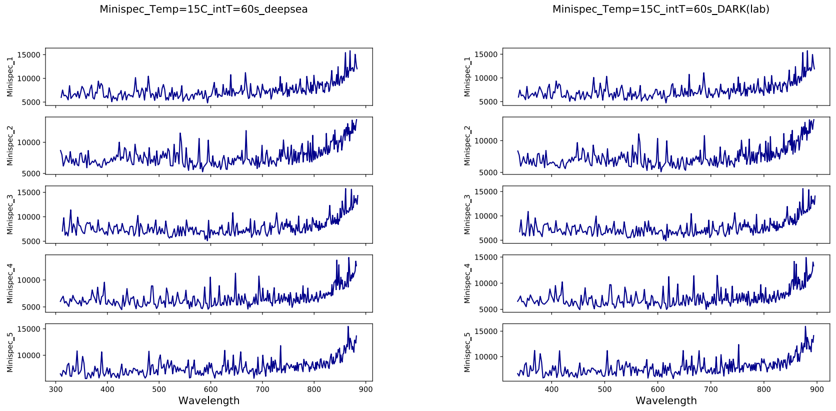

Figure 4.41: **Left:** Example of deep-sea measurement with the Minispectrometer Module, using 60 s integration time window. **Right**: Dark calibration data to subtract for the data illustrated in the plot on the left.

In the region around 550 nm, several consecutive pixels showed a 10% variation over dark. It is unlikely that this is only a dark variation. Therefore, it cannot be excluded that this can be a very faint event. The data-taking is constantly ongoing and systematic studies on this are going to follow.

4.5 STRAW and STRAW-b monitoring

Thanks to the Ocean Networks Canada web platform, it is possible to constantly monitor the STRAW and STRAW-b modules.
The data search page "Oceans 2.0" is publicly accessible and can be found at the address *https://data.oceannetworks.ca/DataSearch*.
For the moment, this page can be used to download only the data of the environmental sensors present in the modules. It is not yet possible to have

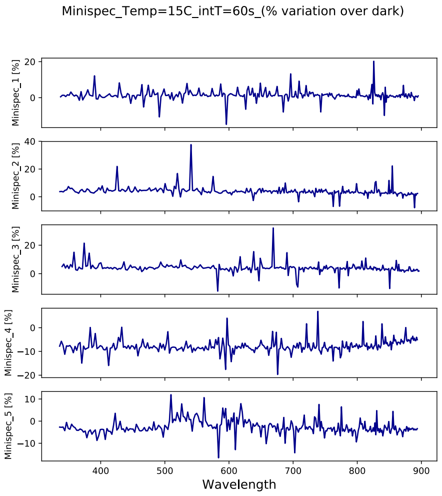

Figure 4.42: Percentage variation over dark spectrum, referred to the previous two plots in 4.41.

access to PMTs or spectrometers data because the integration of the light sensors is still ongoing. Anyway, this feature is already in the pipeline.

> “ *Sí come nell’apprension de’ numeri, come si comincia a passar quelle migliaia di milioni, l’immaginazion si confonde né può più formar concetto, cosí avvenga ancora nell’apprender grandezze e distanze immense.* ”
>
> Galileo Galilei,
> "Dialogo sopra i due massimi sistemi", 1632

Chapter 5

Cascadia Basin site characterisation: STRAW data analysis

Cascadia Basin has been identified as a suitable site for the installation of a future neutrino telescope. This heavily sedimented abyssal plain region, at 2660 m b.s.l., is equipped with Ocean Networks Canada's underwater infrastructure. Thanks to this existing and well-maintained infrastructure, P-ONE can profit from fundamental requirements for mooring lines installation: adequate depth to completely shield the sunlight, closeness to the coast for smooth deployment and solid communication from offshore to the shore station, low values of deep water currents.
At the end of 2018, the first pathfinder - STRAW - has started the site characterisation, measuring the optical properties of the water and monitoring the light background.
In this chapter, we describe the preliminary STRAW data analysis: the first measurement of Cascadia Basin water *attenuation length*, the first monitoring of bioluminescence background intensities and their correlation with underwater currents.
STRAW long-term monitoring also allowed the investigation of the sDOMs photon detection efficiency reduction caused by the biofouling and sedimentation effects.

5.1 Water optical properties and background sources

In deep underwater neutrino telescopes, the background due to the massive low energy component of downgoing atmospheric muons is filtered

out by the huge amount of water.
Other physical phenomena that generate photons in the typical spectral sensitivity range of the PMTs (300-650 nm for STRAW PMT, see paragraph 3.4) contribute to the background, and for them the water cannot act like a veto:

- the environmental radioactivity associated to the ^{40}K decay (water salinity)
- the bioluminescence.

The study of the optical properties of the water and, in parallel, the monitoring of the light background turn out to be fundamental since these two features represent the natural constraints for the future neutrino telescope design.
For example (see paragraph 5.1.1) the *absorption length* largely determines the geometrical layout of the optical modules needed for the detection, while the *scattering length* constraints the angular resolution of the telescope. The optical background resulting from ^{40}K (see paragraph 5.1.4) and bioluminescence (see paragraph 5.1.5) instead affects trigger rates and track reconstruction, while high and lasting bioluminescence blooms can induce a dead time in the data acquisition.

5.1.1 Light transmission in water: absorption and scattering lengths

The detection efficiency of an underwater neutrino telescope depends strictly on the properties of the site and in particular on the light propagation trough the sea water.
A description on the optical properties of the water and their overall context can be resumed as follows [72].
According to the Maxwell's equations of the electromagnetic wave propagation in a medium, both the *scattering* and the *absorption* of light can be related to the properties of the water via its electrical permittivity[1] $\boldsymbol{\epsilon}$, magnetic permeability[2] $\boldsymbol{\mu}$, and electrical conductivity[3] $\boldsymbol{\sigma}$.
Water doesn't have notable magnetic properties, and consequently the permeability $\boldsymbol{\mu}$ can be approximated as that of vacuum (at all frequencies): $\boldsymbol{\mu} = \boldsymbol{\mu_0}$ where $\boldsymbol{\mu_0} = \boldsymbol{4\pi}\times 10^{\boldsymbol{-7}}$ NA$^{\boldsymbol{-2}}$.
Instead, the permittivity $\boldsymbol{\epsilon}$ and the electrical conductivity $\boldsymbol{\sigma}$ depend not only on the frequency of the electromagnetic wave that propagates in the water, but also on the water temperature, pressure, and salinity.

---

[1] It is a measure of the electric polarizability of a dielectric. A material with high permittivity polarizes more in response to an applied electric field than a material with low permittivity, thereby storing more energy in the material.

[2] It is the measure of the resistance of a material against the formation of a magnetic field.

[3] It represents a material's ability to conduct electric current.

In general, the overall effect of ϵ, μ and σ can be expressed with the *complex index of refraction* $m = n - ik$, where n and k are the optical "constants" of water, even though they depend strongly on wavelengths ($n(\lambda)$ and $k(\lambda)$):

$$m^2 = \mu\epsilon c^2 - \frac{i2\pi\mu\sigma c^2}{\nu} = (n - ik)^2 \tag{5.1}$$

where $c = (\epsilon_0\mu_0)^{-1/2}$ is the speed of light in vacuum.

The real part of the complex index of refraction, $n(\lambda)$, is related to the scattering: if it were truly a constant, there would be no scattering, but even in absolutely pure water, thermal fluctuations of molecules occur inducing scattering processes and $n(\lambda)$ variations. Consequently $n(\lambda)$ is connected also to the temperature, pressure and salinity: it decreases with increasing wavelength or temperature, and increases with increasing salinity or pressure, see fig.5.1.

Scattering processes can occur during the interaction of photons with water molecules and dissolved salt (Rayleigh scattering [4]) or with the organic and inorganic particulate (Mie scattering [5]): the dominant feature of these scattering processes is that only the direction of the light changes, not its wavelength (in the sea water the Raman effect indeed can be neglected because it is more rare). The imaginary part $k(\lambda)$, instead, is related to the spectral absorption coefficient $a(\lambda)$ according to the following equation:

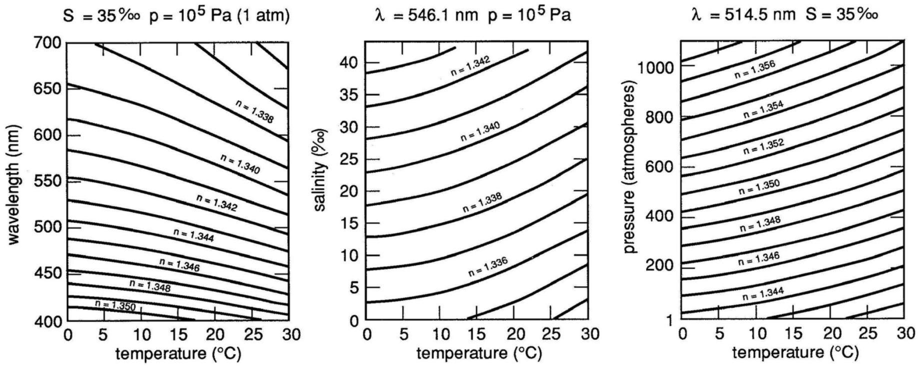

Figure 5.1: Real index of refraction of water for selected values of pressure, temperature, and salinity [72].

$$a(\lambda) = \frac{4\pi k(\lambda)}{\lambda} \tag{5.2}$$

---

[4] It is the elastic scattering of light or other electromagnetic radiation by particles that have a diameter much smaller than the wavelength of incident radiation.

[5] It is the elastic scattering of light or other electromagnetic radiation by particles that have a diameter similar to or larger than the wavelength of the incident radiation

In fig.5.2, the behaviour of the absorption coefficient $a(\lambda)$ vs. wavelengths is shown: it decreases by over nine orders of magnitude between the near ultraviolet and the visible, and then rises again in the near infrared. In the visible band around blue wavelengths, photons don't have enough energy to interact with water molecules and the absorption coefficient $a(\lambda)$ is at the lowest value (around 420 nm). Therefore, these wavelengths are able to propagate easily through the sea water. At lower wavelengths, towards the ultraviolet spectral region, photons start to have enough energy to interact with water and consequently $a(\lambda)$ increases quickly; at even smaller wavelengths other phenomena, like Compton scattering[6], occur. In this case, the water density becomes the main parameter to deal with, differently from its molecular structure considered so far.

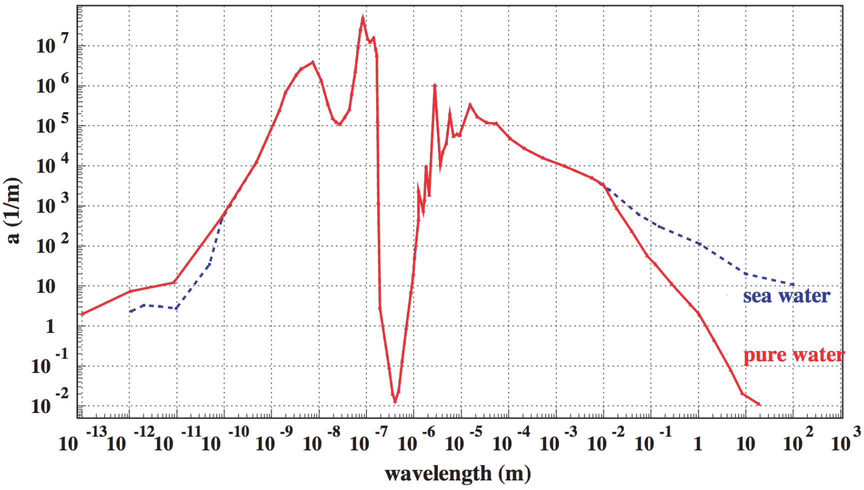

Figure 5.2: Spectral absorption coefficient of pure water (solid line) and of pure sea water (dotted line) as a function of wavelength [72].

The same happens on the other side of the visible band, towards infrared wavelengths. Here, the energy of the photons is high enough to excite the vibrational and rotational modes of the water molecules. This makes the absorption coefficient increase again, except from the very long wavelengths where the photons are not energetic enough to continue this process.

Hence, to properly describe the transparency of the sea water in terms of absorption and scattering, two quantities are monitored:

- the *absorption length* $L_a(\lambda) = 1/a(\lambda)$: defined as the distance $L_a(\lambda)$ in the dielectric after which the initial light intensity is reduced by a factor $1/e \sim 0.37$, due to absorption effects;

---

[6] It is an inelastic scattering between a photon and a charged particle: the wavelength of the scattered photon is different from that of the incident radiation.

- the *scattering length* $L_b(\lambda) = 1/b(\lambda)$: defined as the average distance between 2 consecutive scatters, with the initial light intensity reduced by a factor $1/e$ due to diffusion effects.

In some cases it is more convenient to consider a third quantity that takes into account both processes: the *total attenuation length*, defined as

$$\frac{1}{L_c(\lambda)} = \frac{1}{L_a(\lambda)} + \frac{1}{L_b(\lambda)} \tag{5.3}$$

with $c(\lambda) = a(\lambda) + b(\lambda)$ as the *total attenuation coefficient*.

For the preliminary phase of STRAW feasibility study for the future P-ONE neutrino telescope, we have measured the total *attenuation length* $L_c(\lambda)$.

5.1.2 STRAW measure of the Attenuation Length

According to the literature and previous studies of other similar experiments like DUMAND, ANTARES, KM3NeT and GVD Baikal [73] [74] [75] [76] [50], the expected values for the *attenuation length* in water at different wavelengths, vary between 20 m and 90 m, therefore the geometry of STRAW has been designed to cover this range, see fig.5.3.

The idea is to compare what is detected by an sDOM with respect to what is emitted by a POCAM, and extract the value of $L_c(\lambda)$. Based on the detector design, the attenuation length can be related to the number of detected photons at a certain distance r with the following equation 5.4:

$$N(r) = \frac{N_0}{4\pi r^2} \exp\left(-\frac{r}{L_c(\lambda)}\right) A_{\text{det}} \tag{5.4}$$

where N_0 is the number of initially emitted photons (from the POCAM) and A_{det} is the detector area, in this case the sDOM glass surface.

The sDOMs constantly record the arrival times of all photon hits and, as they are included in the STRAW timing system (see paragraph 3.4), their data are synchronised to the same clock. On the other side, the POCAMs are not synchronized and do not emit a trigger for the readout. Therefore, the adopted strategy used to identify POCAM flashes is based on the

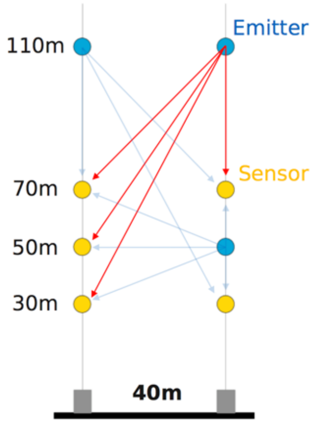

Figure 5.3: Sketch of the two STRAW moorings: the emitters represented by blue dots are the POCAMs, while the receivers in yellow are the sDOMs.

analysis of the time distribution of two consecutive sDOM events, see the Δt histogram in fig. 5.4.

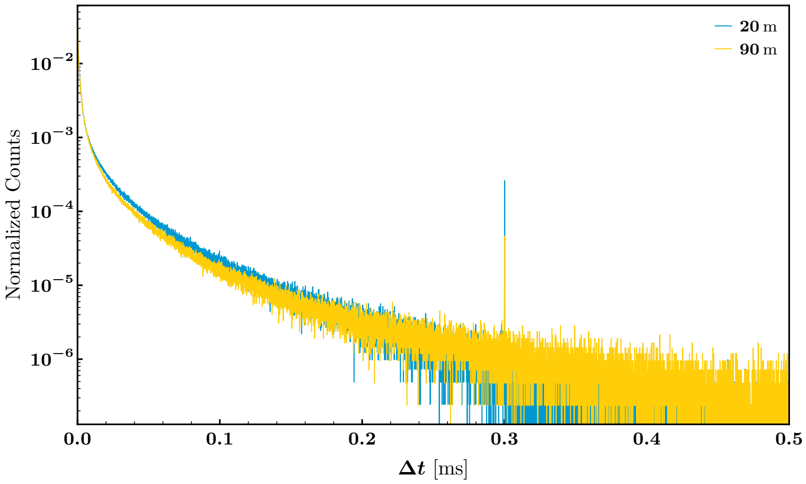

Figure 5.4: STRAW first light: time distribution for 2 consecutive events detected by an sDOM. The peak represents the 465 nm LED POCAM flashes at 3.33 kHz. In blue the events coming from a POCAM at 20 m from the considered sDOM, and in yellow the ones coming from a POCAM situated at 90 m from it. Picture courtesy of Felix Henningsen [51].

The POCAMs emit light with a defined frequency of a few kHz (fixed at the beginning of the data-taking) and at a known distance from the sDOMs. In order to investigate on the quantity of POCAM flashes revealed by an sDOM, a fixed PMT time window, set according to the inverse of the POCAM light emission frequency, is considered. In the example in fig. 5.5 the chosen POCAM frequency is 5 kHz and the PMT time window is 5000 ns, a submultiple of 200000 ns.

Folding thousands of these time windows, the number of counts registered by the PMT every 5 ns (bin) is collected to build an histogram: a pileup of events clearly identifies POCAM flashes, since they reach the PMT mostly at the same moment over a flat background due to the PMT dark noise, radioactivity and bioluminescence.
After the estimation of the total POCAM emitted light flashes in a defined time interval, the attenuation length $L_c(\lambda)$ is calculated using a model that considers it as a free parameter, while the design of the two moorings, the sDOM geometry, its detection and angular efficiencies are taken as constraints [77].

The first preliminary results of the *attenuation length* collected with the four POCAM Kapustinsky driven LEDs are promising and are listed below:

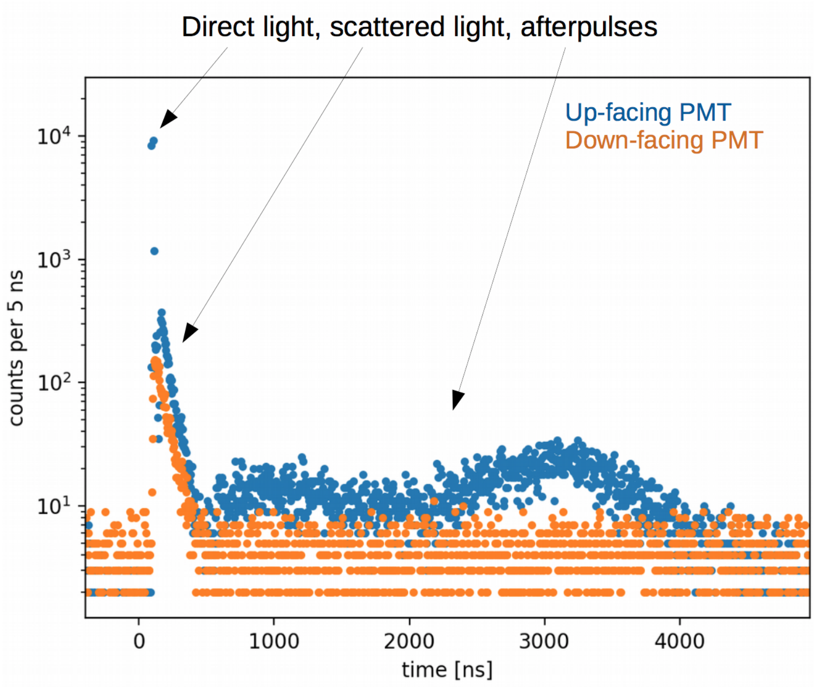

Figure 5.5: Histogram of the photon arrival times on an sDOM. The number of counts registered by the PMTs every 5 ns are distributing as follows: the POCAM flashes are accumulating around the same bins, as they reach the PMTs mostly at the same moment; the PMT facing the POCAM detects direct light, while the PMT facing the opposite side detects only scattered photons. The phasogram also shows the afterpulsing distribution of the PMTs, between 0.5 and 4 us after the direct peak. Picture courtesy of Dr Christian Fruck [77].

- L_c(365 nm): 9.9 m +/- 0.4 m (stat.) +/- 1.0 m (sys.)
- L_c(405 nm): 15.6 m +/- 0.7 m (stat.) +/- 3.0 m (sys.)
- L_c(465 nm): 31.0 m +/- 1.0 m (stat.) +/- 6.0 m (sys.)
- L_c(600 nm): 5.0 m +/- 0.5 m (stat.) +/- 2.0 m (sys.)

The preliminary measurements of the STRAW attenuation length, compared to the values for the clearest water [71] and to the values measured at the KM3NeT site, are shown in fig. 5.6 .

5.1.3 Deep water environmental parameters: temperature, salinity and water current

Oceanic waters are classified according to their salinity and temperature, both contributing to their density. The same site can contain warm water

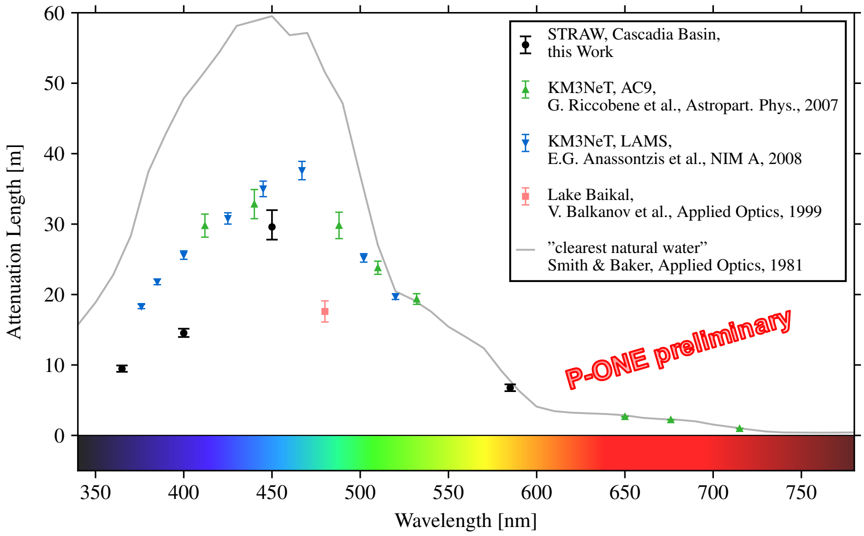

Figure 5.6: Attenuation length vs. wavelength. The wavelengths tested are relative to the POCAM LED matrix ones. Also, measurements from various other neutrino telescope sites and the results from a study of attenuation lengths in the clearest ocean waters are shown for comparison. Plot courtesy of Dr Christian Fruck, TUM.

or cold and more dense water in different regions or even at different water column depths.

The working environmental conditions of a deep-sea neutrino telescope need to be accurately monitored, since they can impact on the properties of the data.

As described in the paragraph 5.1.1, temperature, pressure and salinity affect the real part of the complex index of refraction $n(\lambda)$, playing an important role in the diffusion of the light in the deep-sea.

These environmental macroscopic parameters are generally not constant in time, therefore a costant ***in situ*** monitoring is fundamental.

In particular, the **sea temperature**, has a major effect on all the electronic components and on the PMTs performance [64]. Measurements in Cascadia Basin, at 2654 m depth, taken using a CTD (Conductivity Temperature Depth) device coupled to the ONC permanent infrastructure, show that the water temperature is highly constant over long periods, ranging between 1.74 ° C and 1.8 ° C, see fig. 5.7: this provides a stable working environment for the STRAW equipment.

Once measured the temperature and the conductivity with the CTD, the value of the **salinity** can be extrapolated, fig. 5.8. This parameter is related to the amount of salt dissolved into the water, whose main compounds are sodium chloride, magnesium sulfate, potassium nitrate and sodium bicarbonate, which dissolve into ions. Therefore the salinity is strictly connected

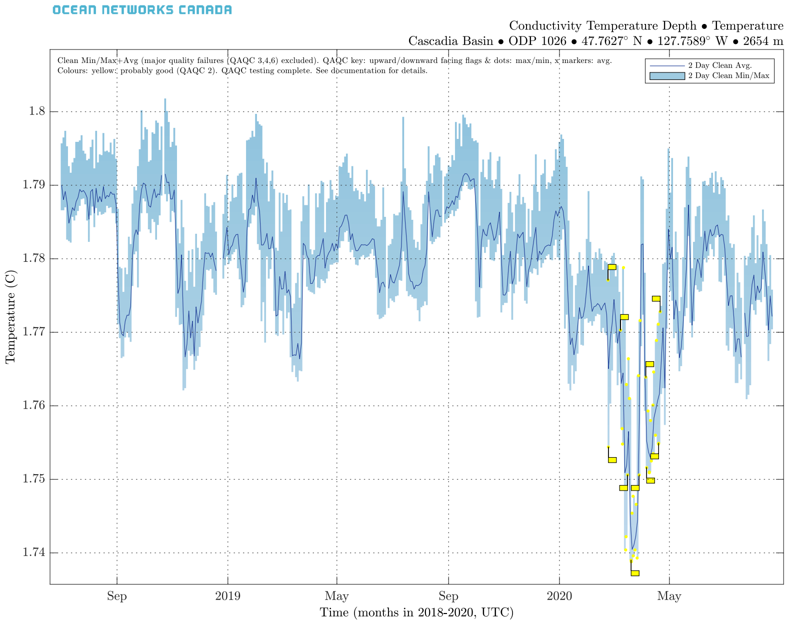

Figure 5.7: Monitoring of the temperature in Cascadia Basin over 2 years from 2018 to 2020, at 2654 m depth using a CTD. This plot has been generated using to the ONC Data Search web platform [78].

to the natural radioactive isotope of ^{40}K whose decay represents one of the main contributes to the optical background (see paragraph 5.1.4).

During September 2015, June 2017 and July 2018 several dedicated marine campaigns have been performed by ONC at the Cascadia Basin site in order to determine the vertical profiles of the environmental parameters mentioned above. These measurements reveal how their values distribute along the water column (how homogeneous) and support the identification of potential seasonal dependencies due to different distributions in the organic and inorganic matter.
The plots in fig. 5.9, that I obtained analysing the data provided by Dr. Fabio De Leo (ONC), shows the vertical profiles for temperature and salinity up to 1200 m depth for the 3 campaigns: both parameters exhibit no significant variation over the investigated timescale and depth, confirming the excellent physical properties of the water.

In an underwater neutrino telescope, the detection devices are installed on vertical mooring lines subjected to displacement due to **water currents**. Information on a long term monitoring of deep water currents is therefore necessary to define the mechanical structure of the telescope, that is designed in order to resist to a certain range of drag forces. In addition,

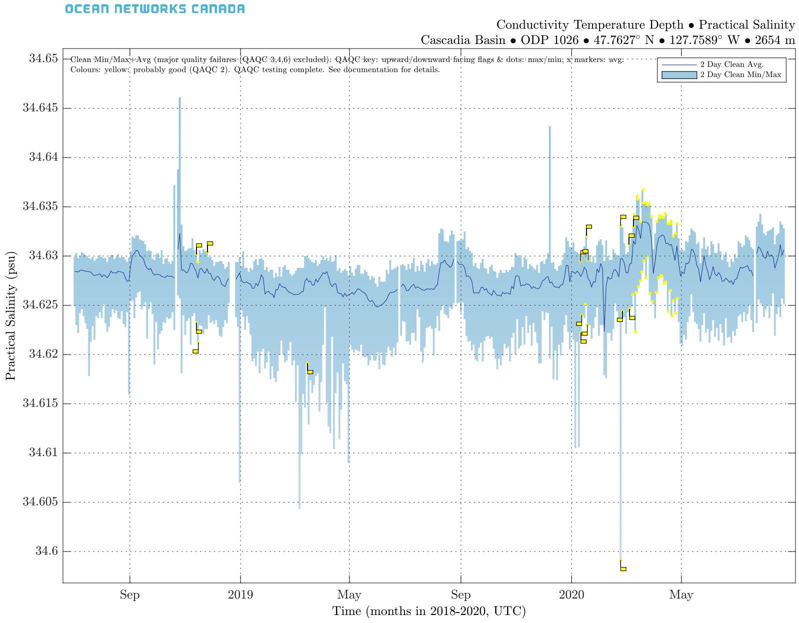

Figure 5.8: Monitoring of the salinity expressed in psu (*Practical Salinity Unit*: 1psu is equal to 1 g of salt per litre of water) in Cascadia Basin over 2 years from 2018 to 2020, at 2654 m depth using a CTD. This plot has been generated using to the ONC Data Search web platform [78].

as will be widely described in the following paragraphs, since the currents are partly responsible for the bioluminescence activity, a monitoring is also helpful to constrain the optical background around the telescope.

In Cascadia Basin, a *current meter* installed 4 km from the STRAW monitors the water currents at the seafloor level. In order to have an estimate of the current values during STRAW activity time window, I analysed the data provided by ONC Data Search web platform for this device, for the period from January 2018 to February 2020. As shown in fig. 5.10, the water current values (at a depth around 2654 m) are ranging from 0.5 mm/s to 13.5 cm/s, with a maximum of the distribution around 3 cm/s: STRAW moorings have been designed in order to withstand such water currents.

5.1.4 Environmental radioactivity

Sea water contains some level of natural environmental radioactivity that, if energetic enough, emit Cherenkov light producing a visible background. The main contribution to the light background in sea water is related to the presence of ^{40}K, an isotope of the potassium[7] whose relative abundance is

---

[7] An *isotope* is a different form of the same element that contains equal numbers of protons but different numbers of neutrons in its nucleus.

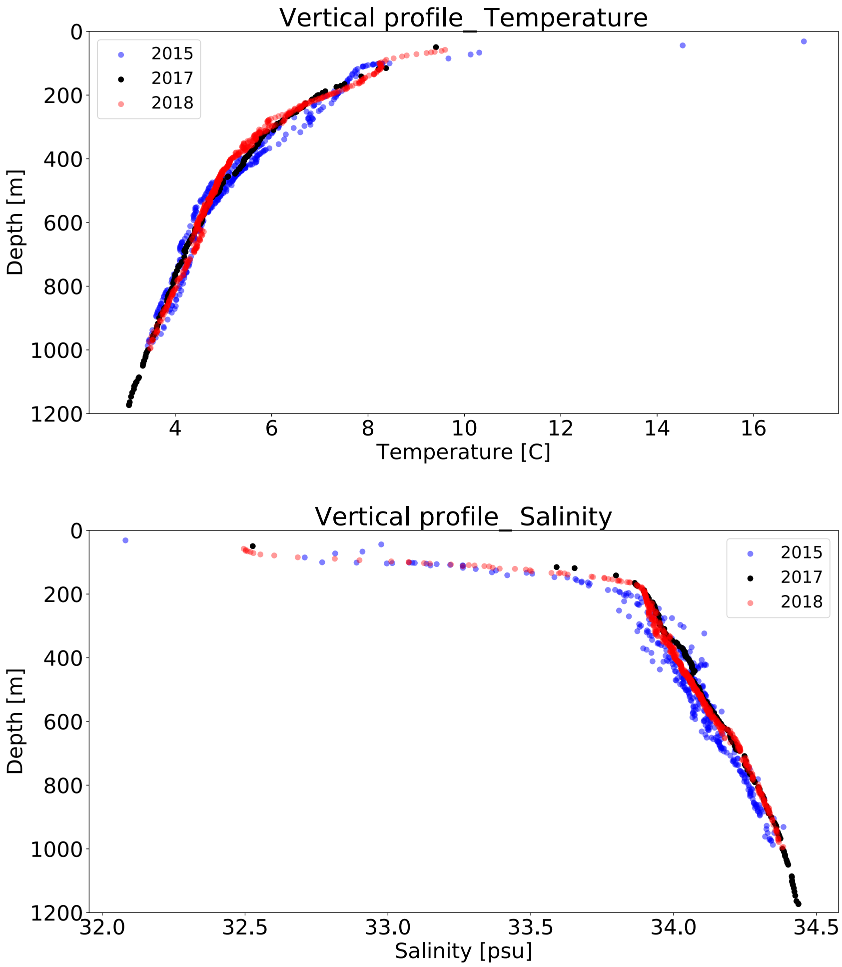

Figure 5.9: Vertical profiles -for the first 1200 m of the water column- of temperature and salinity at Cascadia Basin site, measured in September 2015, June 2017 and July by an Ocean Networks Canada marine campaigns [78]. Both parameters don't show particular variations over the investigated timescale and depth.

of 0.012% and half-life is $1.27*10^{9}$ years.
It decays with a B.R. of 89.3% into ^{40}Ca by emitting an electron and with a B.R. of 10.7% into ^{40}Ar by electron capture, emitting an energetic γ ray (photon):

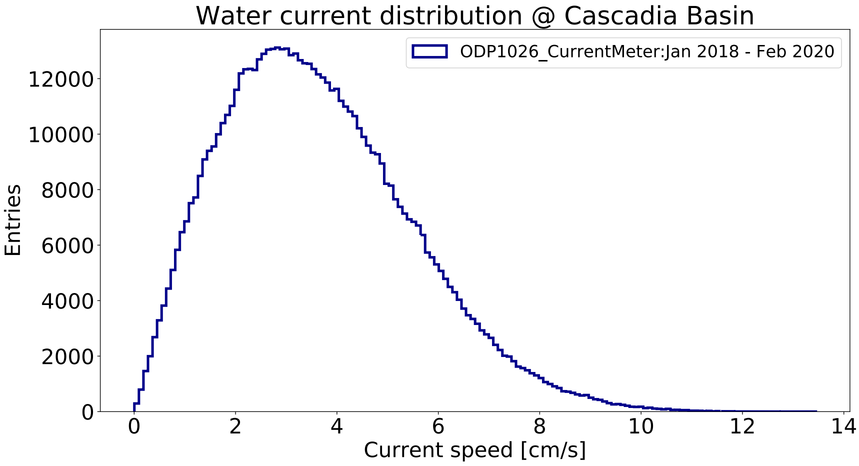

Figure 5.10: Distribution of the deep-sea current measured with a current meter at 2654 m depth in Cascadia Basin. The period considered is from January 2018 to February 2020. The data plotted here have been downloaded from the ONC Data Search web platform [78].

$$\begin{gathered} {}^{40}K \rightarrow {}^{40} Ca + e^- + \bar{\nu}_e \\ {}^{40}K + e^- \rightarrow {}^{40} Ar + \gamma + \nu_e \end{gathered} \tag{5.5}$$

In the β-decay channel the electron produced with a kinetic energy up to 1.3 MeV leads to Cherenkov light emission when traveling in water. In the electron capture channel the produced 1.46 MeV photon generates energetic electrons through Compton scattering which subsequently emit Cherenkov light. These processes occur as above the Cherenkov threshold (E_{th} = 0.26MeV for n_{water} = 1.33) and constitute a low energy background which is visible in the telescopes [79]. This background can be also used for optical modules time calibration.

Preliminary studies with the STRAW experiment (analysis of the PMT rates) determine how the environmental radioactivity affects the optical modules. The continuous monitoring led to the identification of a *base rate* whose value ranges from a minimum of $\sim$ 5 to a maximum of 63 kHz and changes very slowly on a time scale of hours. Since this baseline is generated not only by the photons originated from the potassium decays, but also by the diffuse bioluminescence and by the PMT dark counts, the only contribution of the environmental radioactivity cannot be isolated, see paragraph 5.3. It is possible to verify our understanding of this activity by comparing in situ measurements from STRAW with a Geant4 simulation of the sDOM response to ambient ^{40}K, to appear soon in a P-ONE collaboration paper.

5.1.5 Bioluminescence

The *bioluminescence* is, together with ^{40}K, the other ambient source of background for an underwater neutrino telescope.

This phenomenon consists in the emission of visible light by a living organism as the result of a natural chemical process after mechanic, electric or light stimulation. It is mainly present in the marine environment where several species of pelagic fauna[8] use it for vital functions ranging from communication and defence to reproduction.

Defensive bioluminescence emission has been observed as a consequence of organisms colliding with submerged objects, but in general it is even related to deep ocean environmental parameters like salinity, temperature and water currents (as described in the following paragraphs of this chapter).

Two kind of bioluminescence emissions can be observed [80]:

- **a steady bioluminescence**: related to the presence of luminescent bacteria (unaffected by mechanical stimulation) that emit steady homogeneous diffused light (varying on a time scale of hours or days). It is, in addition to the ^{40}K background, identified in the data by the so called *baseline* contribution, see paragraphs 5.1.4 and 5.3.
- **a bursting bioluminescence**: intensive light bursts that can reach frequencies up to ∼MHz and that can last from a few tenths to a few tens of seconds (as an example in fig. 5.46 is shown one of the bioluminescence events detected by all sDOMs in STRAW; this plot is also reported in a full-page size in the appendix 5.A at the end of this chapter). The bursts are mainly correlated with water currents as small organisms can strongly impact on the sensors, see paragraph 5.4. This phenomenon can be seasonal or it can happen also when water current values are relatively small and other peculiar environmental conditions occur, such as dense water formation events[9] [81].

The amount of light signals associated with the bioluminescence is directly proportional to the presence of fishes and bacteria living in a site. It is helpful, at this scope, to perform deep-sea campaigns in order to measure the

---

[8] The pelagic fauna is made up of species that for the whole life or for a continuous period of it live independently from the bottom and the shores, at the mercy of waves and currents. Typical characteristics of pelagic animals are the transparency of the body and the strong hydration of the tissues that gives it a density almost equal to that of the sea water, a condition favorable to floating.

[9] During late winter, because of cold and persistent wind that cools sea surface, dense deep water formation occurs: when cooled, shallow waters become denser than the deeper waters and start sinking, originating movements of convection with consequently stimulation of bioluminescence events.

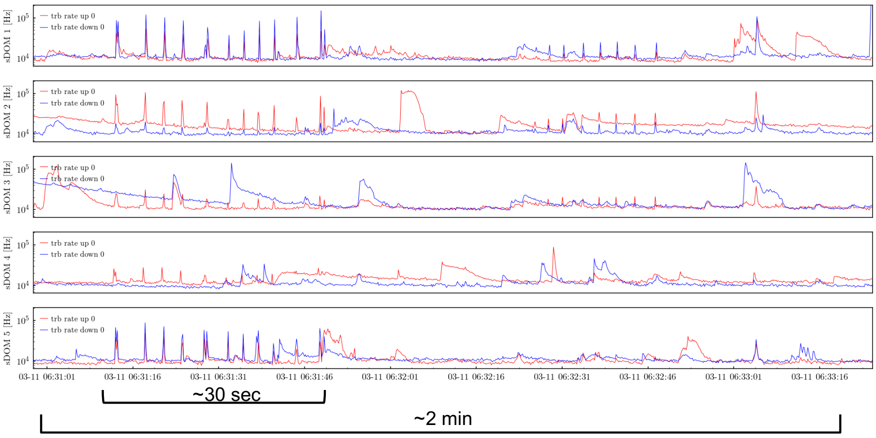

Figure 5.11: Bioluminescence event detected by all five sDOMs in STRAW. Several pulses in a time window of 30 sec can be appreciated. A bigger version of this image is shown in the Appendix at the end of this chapter. All credits for this plot to Dr Christian Fruck, TUM.

density of living organisms along the water column since their presence varies with the depth. In the fig. 5.12 is shown an example of density profile of the bioluminescent organisms in Cascadia Basin for the first 1000 m depth for 3 surveys performed during 2015, 2017 and 2018. New surveys that will monitor until 2660 m depth have been scheduled for September 2020 and the results will be available soon.

From previous studies [70][10] [82][11] on the emission spectrum of deep-sea organisms it is known that the light emission occurs at those wavelengths for which the water has the greatest *absorption length*, see fig. 5.13 and fig. 5.14, and matches perfectly with the detection sensitivity range of photomultipliers (300-650 nm for STRAW PMT, see paragraph 3.4).

So far, only laboratory experiments on "fished" animals have been performed. To study the phenomenon as it is in deep ocean environmental conditions, *in situ* , STRAW-b will measure the bioluminescence activity emission thanks to three spectrometer modules.

---

[10] *From the abstract*: "The emission spectra of 70 bioluminescent marine species were measured with a computer controlled optical multichannel analyzer (OMA). A 350 nm spectral window is simultaneously measured using a linear array of 700 silicon photodiodes, coupled by fiber optics to a microchannel plate image intensifier on which a polychromator generated spectrum is focused. [...]Among unusual spectral features revealed were organisms capable of emitting more than one color [...]."

[11] *From the abstract*: "[...]To investigate the luminescence responsivity of Pyrosoma atlanticum and Pyrosomella verticillata, photic, electrical, and mechanical stimuli were used. Photic stimulation of $1.5 \cdot 10^{\mathbf{9}}$ photons $\cdot$ $s^{\mathbf{-1}} \cdot$ $cm^{\mathbf{-2}}$, at wavelengths between 350 and 600 nm, induced bioluminescence, with the maximum response induced at 475 nm. [...]Repetitive, regular mechanical or electrical stimulation elicited rhythmic flashing characterized by alternating periods of high and low light intensities."

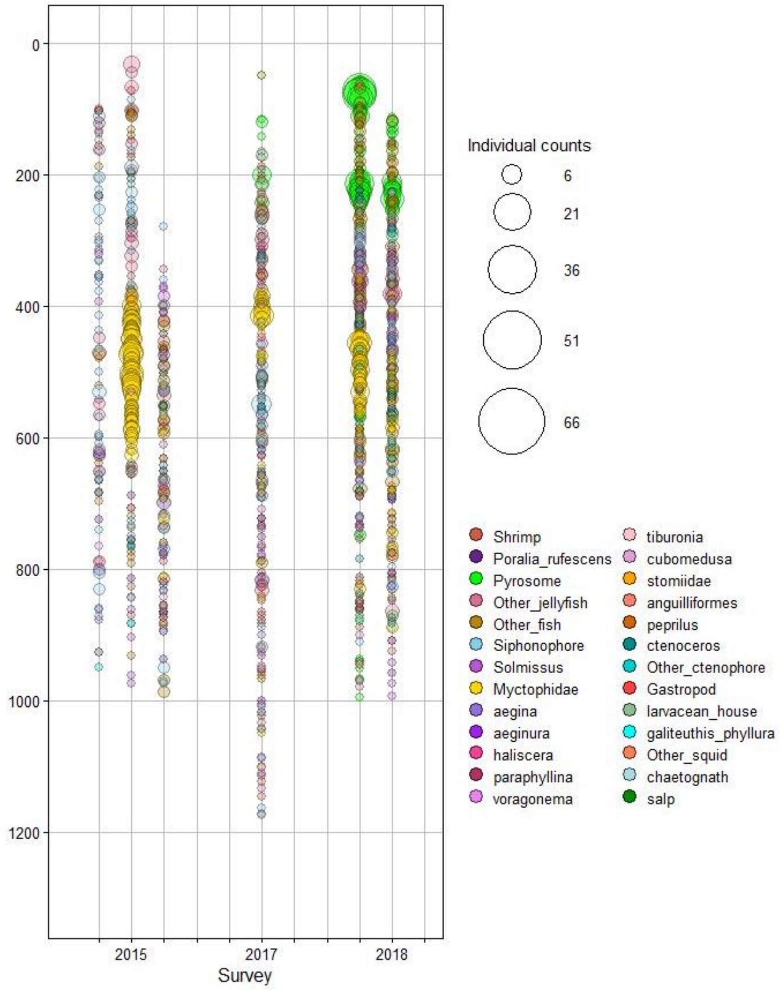

Figure 5.12: Density profile for bioluminescent organisms in Cascadia Basin for the years 2015, 2017 and 2018. All credits for this study to Dr. Fabio De Leo Cabrera - Ocean Networks Canada, University of Victoria, BC - Canada.

5.2 Rates long term monitoring

As reported so far, for a proper design of P-ONE, it is important to understand the long-term behaviour of light background and water optical properties of the chosen site. At this scope, the main goal of the STRAW experiment has been to perform a monitoring of Cascadia Basin site environmental conditions.
The registered rates are the result of PMT dark counts, photons related

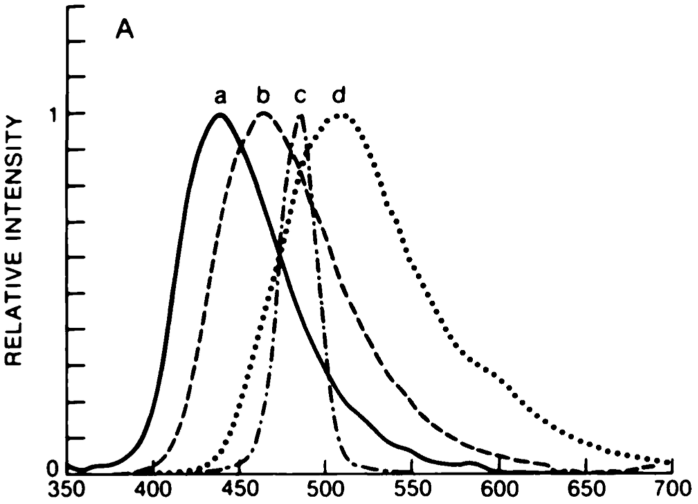

Figure 5.13: An example of some bioluminescence emission spectra for different animals: (a) *Scina cf. rattrayi* λ_{max} = 439 nm, FWHM = 70 nm; (b) *Vargula hilgendorfii* λ_{max} = 465 nm, FWHM = 83 nm; (c) *Argyropelecus affinis* λ_{max} = 487 nm, FWHM = 26 nm; (d) *Cleiodopus gloria-mans* λ_{max} = 506 nm, FWHM = 92 nm [70].

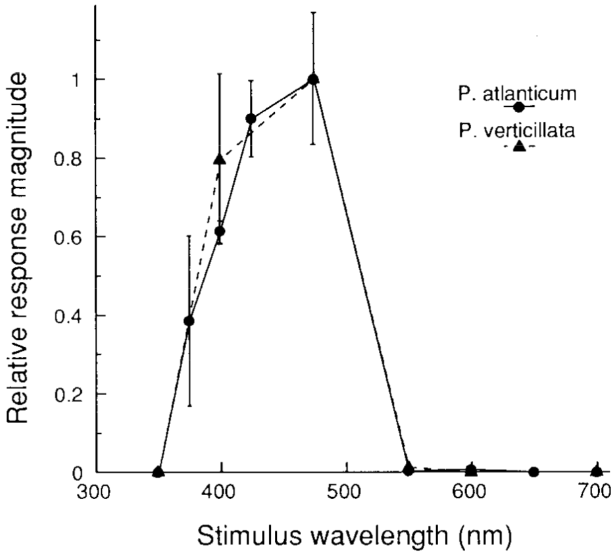

Figure 5.14: Magnitude of the relative response vs light stimulus wavelength. Peak response for both pyrosomes was for a 475 nm light pulse: colonies often produced from 25 to 30 flashes over ∼2h period [82].

to the ^{40}K radioactive decays (the potassium is present not only in the salt

dissolved into the sea water but also in the glass of the optical modules) and contributions from bioluminescence, that can fluctuate over time according to specific circumstances (see paragraphs 5.1.5 and 5.8).
The first focus of my work then has been to analyse the data stream from the 5 sDOMs of STRAW for the entire period of activity so far and try to answer to these questions:

- What is the range of values in which the rates variate?
- Is there any modulation over time? (day/night, seasonal, ...)
- Is there any more intense burst activity period? Is it connected to an increased water current?

In fig. 5.15 there is an example of registered rates in a time window of 10 minutes. As described in paragraph 3.4, the PADIWA board has 4 levels of threshold for the PMT signals sampling and, for this study, only the lowest level "*CH0*" has been considered: this corresponds to 0.5 p.e. threshold for the PMTs so that every single photon detected is taken into account for the monitoring.

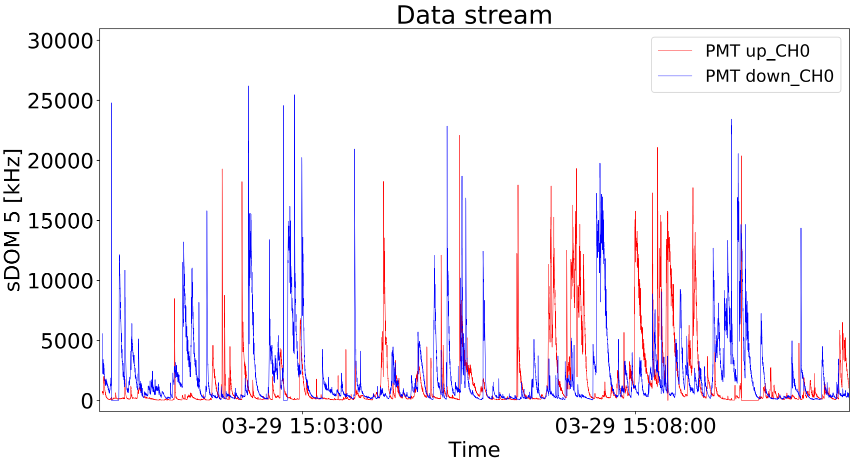

Figure 5.15: Rate registered from the sDOM5 in a time window of 11 minutes. The blue line is representing the PMT facing downward, while the red one is representing the PMT facing upward. No averaging is applied in this data set: the PADIWA is sampling every 0.03 seconds and the detected events are ranging from a few kHz to 25 MHz.

Since the TRB (paragraph 3.4) samples the PMTs signals every 0.03 seconds, to speed up the analysis for very long periods it is useful to average a certain amount of acquisitions that, in turn, corresponds to a certain time window: the overall trend will be not affected by the averaging on a small time scale and the data processing will be quicker.

In the example in fig. 5.47 the data are averaged over 4 hours (this corresponds to 480000 acquisitions collected in this time window), from the end of February 2019 to the end of May 2020. In this time window several periods of higher background level due to a combination of bioluminescence bursts on top of a diffuse bioluminescence baseline have been registered. This plot is also reported in a full-page size in the appendix 5.A at the end of this chapter. In the following paragraphs I will describe my analysis strategy on the identification and quantification of different background components, also according to their correlation with environmental parameters.

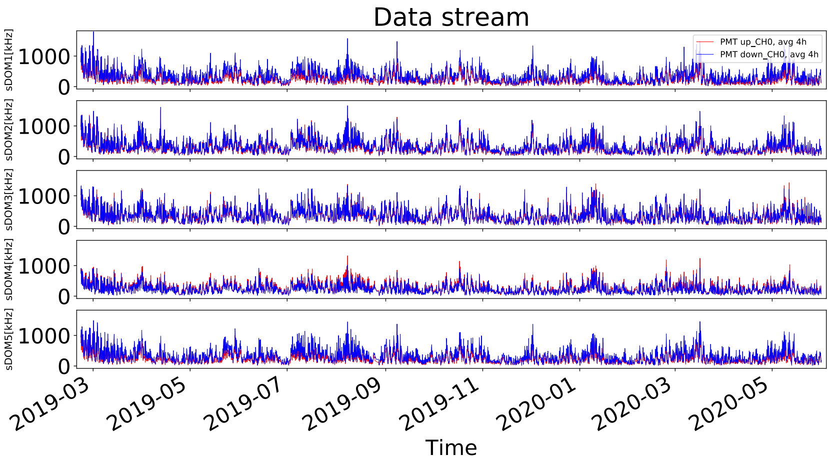

Figure 5.16: Data stream of the 5 sDOMs of STRAW: the data considered are taken from the end of February 2019 to the end of May 2020 and are avaraged every 4 hours. Periods of increased background level combined with higher bioluminescence activity can be seen.

5.3 Baseline analysis

The lowest value of the continuous data stream measured by the optical modules is defined as *baseline*. The baseline represents the contribution to the light background that largely comes from the ^{40}K radioactive decays: since it depends only on the salinity, it is mainly constant.

The contribution of diffuse bioluminescence (not necessarily bursts) can add an extra offset to the baseline during some periods of major bioluminescence activity. Monitoring the possible baseline variations and identifying the different contributions is very fundamental as it helps in subtracting the right background from neutrino-related PMTs signals.

Only for representation purpose, in fig. 5.17 is shown the rate distribution for the PMT$_{up}$ of sDOM5 in a 12 h time window of a random day of February 2019 with no averaging on the data. The range of the considered rates has

been from 0 kHz to 250 kHz (distributed in 1000 bins), in order to cut the very long bursts tail that was not the focus of this analysis.
Three main parts can be identified in the histogram of the rate distribution in fig. 5.17:

- the *pedestal*: the rate value shouldn't be lower than a certain minimum caused by steady bioluminescence and ^{40}K, but this can happen sometimes, likely caused by some module electronics defects.
- the *peak*: is representing the *baseline*, as it is the most frequent value of the registered rates whose contributions are due to ^{40}K and bioluminescence constant activity (also bursts in same cases).
- the *tail*: is representing the light events that happen less frequently, like bursts of bioluminescence.

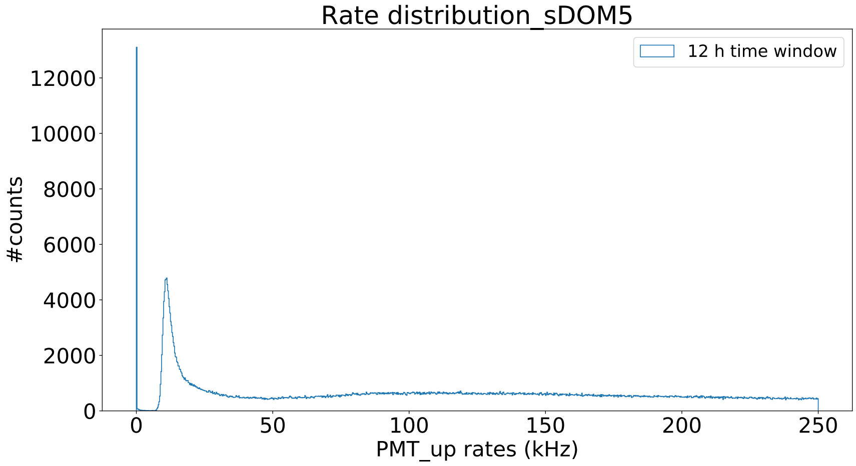

Figure 5.17: Rate distribution for the PMT$_{up}$ of sDOM5 in a 12 h time window (no averaging on the data). The range of the considered rates has been up to 250 kHz (distributed in 1000 bins), in order to cut the very long bursts tail. Three main parts can be identified in the histogram: the *pedestal*, the *peak* and the *tail*.

In fig. 5.18 are plotted the rate distributions (without the pedestals) of 10 consecutive 12 hours time windows (5 days), always for the month of February 2019: some distributions are very different from the others, highlighting how even the diffuse bioluminescence activity can not only shape the rate distribution but can also affect its peak value.

Considering the **peak** of every distribution as mentioned above, we analysed 16 months of STRAW data (February 2019 - May 2020) in 12 hours time windows. The results is what appear in fig. 5.48: generally the trend shows the same periods of increase for all sDOMs. Some exceptions occur and differences even between the two PMTs of the same sDOM can be appreciated: one hypothesis is that probably some bioluminescence bursts

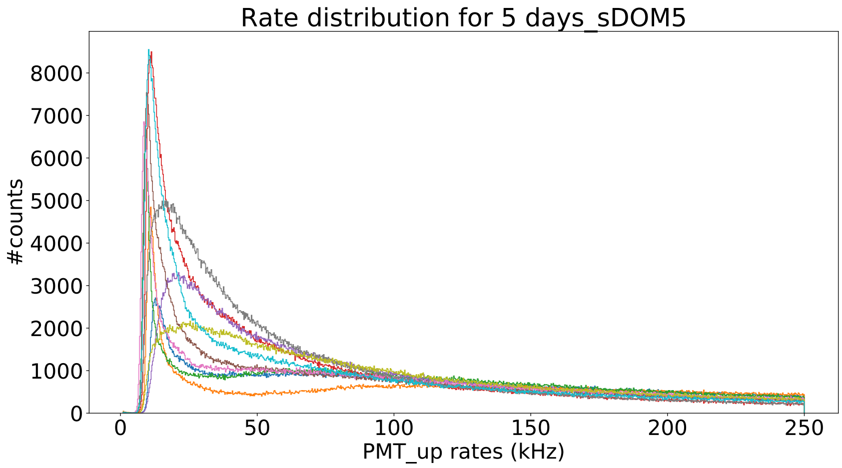

Figure 5.18: Five consecutive random days of February 2019, divided into 12 h time windows with no averaging on the data: the cut has been set at 250 kHz in order to isolate the diffuse component and exclude the bursting regime. Some distributions are very different from the others, highlighting how variable can be the diffuse bioluminescence activity.

are so local and persistent to affect just the baseline of one photodetector. We observed a minimum for the baselines of ~ 5 kHz, caused by PMTs dark counts and ^{40}K dissolved into the sea water and contained into the optical module glass, and a maximum of ~ 63 kHz. This plot is also reported in a full-page size in the appendix 5.A at the end of this chapter.

In the histogram in fig. 5.20, we report the distribution of the observed baselines in the same 16 months period, ranging between 7 and 10 kHz. Since the ^{40}K is most probably stable, the remaining baseline rate is interpreted as diffuse bioluminescence.

5.4 Burst fraction analysis

In this paragraph, we continue the study of the baseline rates searching for increased activities due to bursting events (bioluminescence).
At this scope, I introduce here the quantity *burst fraction*.
The burst fraction is calculated as the number of events higher than a certain threshold, integrated and normalised to the total amount of detected events. Considering that STRAW baseline, as shown in fig. 5.48, ranges from 5 to around 63 kHz and that those specific rate distributions can be quite wide (fig. 5.18) depending on the bioluminescence activity, I have chosen to define the threshold as the rate value corresponding with the beginning of the tail of the distributions, around 200 kHz.
The evolution in time of the burst fraction is shown in fig. 5.49, also re-

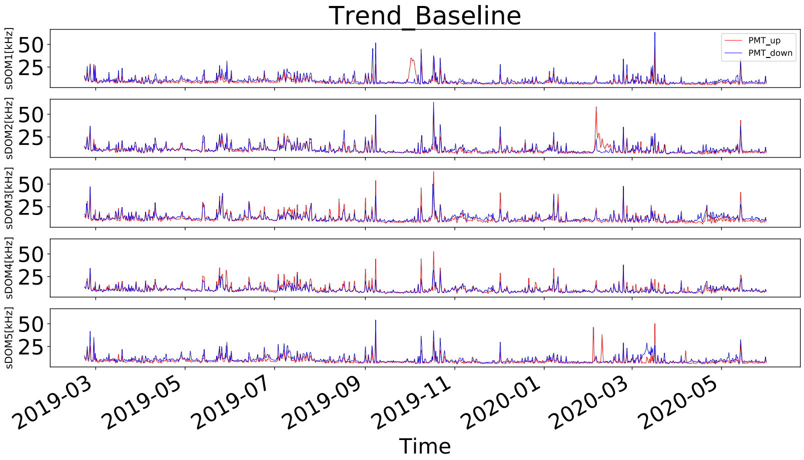

Figure 5.19: Trend over time of the baseline values: generally all sDOMs show the same behaviour. Sometimes exceptions can occur, and even two PMTs of the same sDOM can register different peak values. In the time window from the end of February 2019 to the end of May 2020 the baseline varies between a minimum of ∼5 kHz and a maximum of ∼63 kHz.

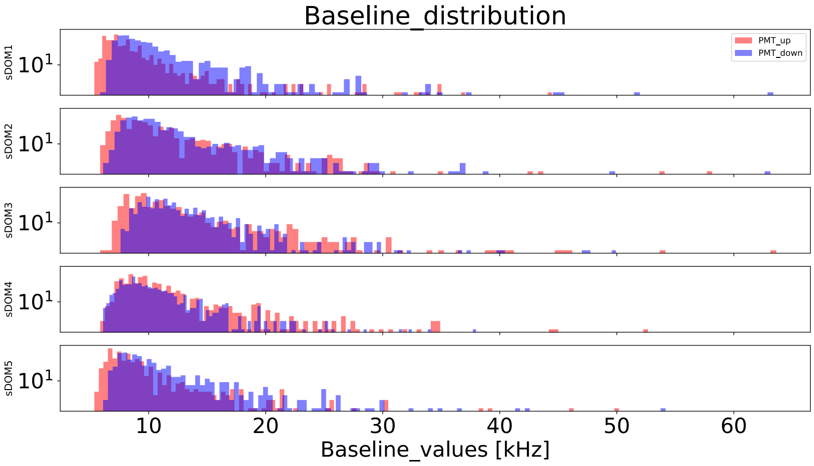

Figure 5.20: Distributions of all the baseline values for the analysed 16 months period: the peaks of these distributions indicate that the most frequent baseline values are ranging between 7 and 10 kHz for every sDOM.

ported in a full-page size in the appendix 5.A at the end of this chapter. If compared with the baseline trend it is possible to estimate the correlation between the two quantities, see the plot in fig. 5.22. In this plot are represented all the couples of points for one PMT of one optical module.

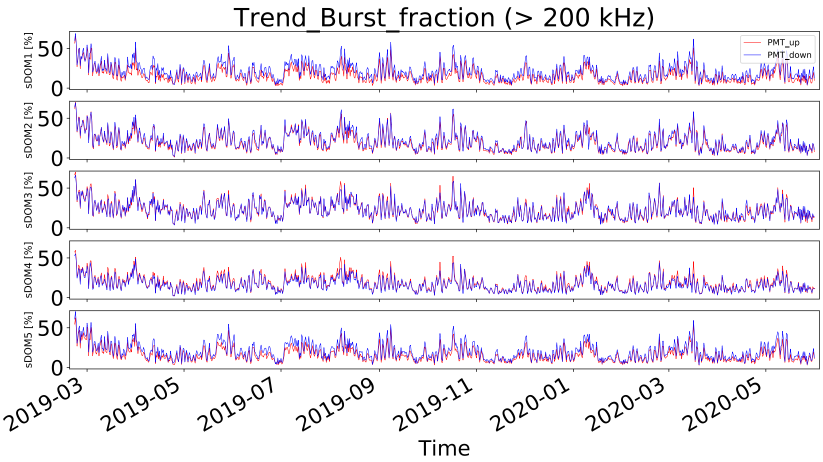

Figure 5.21: Evolution in time of the burst fraction, calculated as all the counted rates greater than 200 kHz.

For the 70% of the events, the corresponding burst fraction is lower than 25%. In such "low bioluminescence activity regime", the average level of the baseline is constant within few percents. For burst fraction values higher

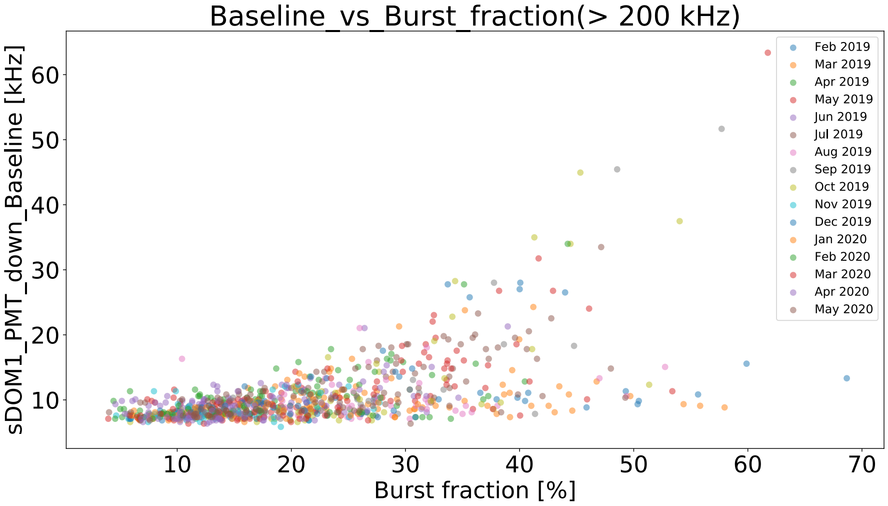

Figure 5.22: The 70% of baselines is uncorrelated with the burst fraction up to 25%: these phenomena are related to different sources of light background. For burst fraction values higher then the 25%, two population of points can be distinguished: low baseline, high burst fraction: uncorrelated; high baseline, high burst fraction: direct correlation of 0.86.

than 25%, we can identify two population of points:

- low baseline ($\leq$ 25 kHz), high burst fraction: no correlation is present. The two quantities do not influence each other, suggesting that these phenomena are related to different sources of light background, i.e. various population of deep-sea organisms.
- high baseline($>$ 25 kHz), high burst fraction: linear correlation with $\boldsymbol{\rho}$ factor of 0.86.

In the last case, deep-sea organisms that generate bursts influence the diffuse bioluminescence when their emission is very high or persistent. The high-burst regime favours a pile-up effect and a consequent increase of the baseline. Then the detected count rate turns out to be higher, and the baseline shows an offset.

5.5 Correlation of baselines and bursts with water current

The water currents produced by the tides are among the primary elements that trigger the bioluminescence activity.

The neutrino telescope submerged structure acts against the water current producing local turbulences. These local turbulences stimulate mechanically the deep-sea organisms that, consequently, emit light [81]. Besides this relatively well-known effect, it is possible to observe a higher level of bioluminescence in a certain period of the year, probably related to dense water formation events. Indeed it can happen that, because of cold and persistent wind that cools sea surface, shallow waters become denser than the deeper waters and start sinking, originating convection movements with consequent stimulation of bioluminescence events.

To monitor how the deepwater currents of Cascadia Basin affect the bioluminescence detected by STRAW, I have taken into account the measurements from the closest Acoustic Doppler Current Profiler - ADCP -, situated at 4 km from the two moorings along with the ONC infrastructure, as shown in fig. 5.23. The ADCP uses the Doppler effect of sound waves scattered back from particles along the water column to measure the deep-sea currents at different depths (dividing ideally the water column into several depth cells called *bins*), fig. 5.24.

The frequency shift of the echo is proportional to the water velocity and the travelling time of sound waves gives an estimate of the distance.

I studied the correlation between the ADCP measurements and STRAW burst fractions in search of a possible (expected) signature of the current water influence on deep-sea organisms light emission. In fig. 5.25 are shown the burst fractions measured by sDOM5 for both PMTs, depth around 2590 m, and the currents detected by the ADCP bin that covers the

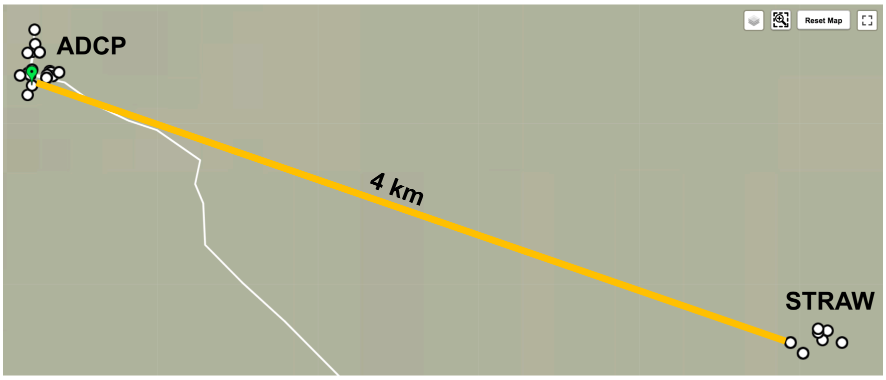

Figure 5.23: Position of the ADCP device with respect to the position of the two STRAW moorings in Cascadia Basin.

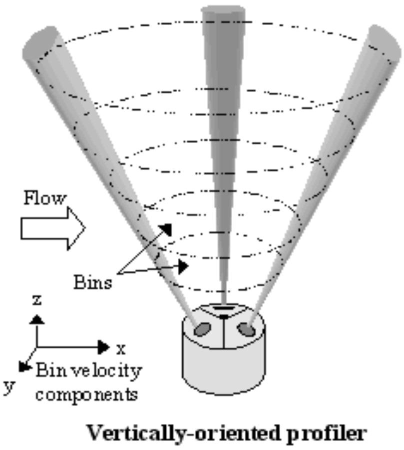

Figure 5.24: Sketch of the Acoustic Doppler Current Profiler working principle: the Doppler effect of sound waves scattered back from particles along the water column is used to measure the deepsea currents at different depths (dividing ideally the water column in several depth cells called *bins*).

same depth (2595.19 ± 4 m, bin size 8 m). The points represent the mean values of currents and rates, averaged over 15 minutes time windows; the entire data-set is one month, March 2019. Despite the ADCP device is situated 4 km far from the STRAW moorings, it is possible to observe a direct correlation between the water current and the burst fraction: the correlation factor ρ for the entire set of data (March 2019) is 0.65, as shown in fig. 5.26. Following the same approach, I have investigated also the correlation between water currents and baselines.

In this case, the obtained correlation is slightly weaker with a ρ factor of

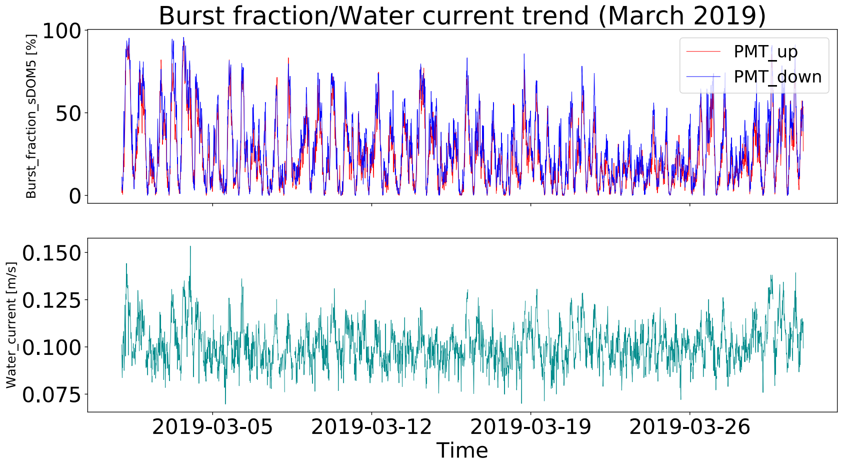

Figure 5.25: **Top**: Burst fractions trend, detected by sDOM5 for both PMTs. **Bottom**: Currents detected by the ADCP bin that covers the same depth as the sDOM5. The points represent the mean values of currents and rates, averaged over 15 minutes time windows; the entire data-set is from March 2019.

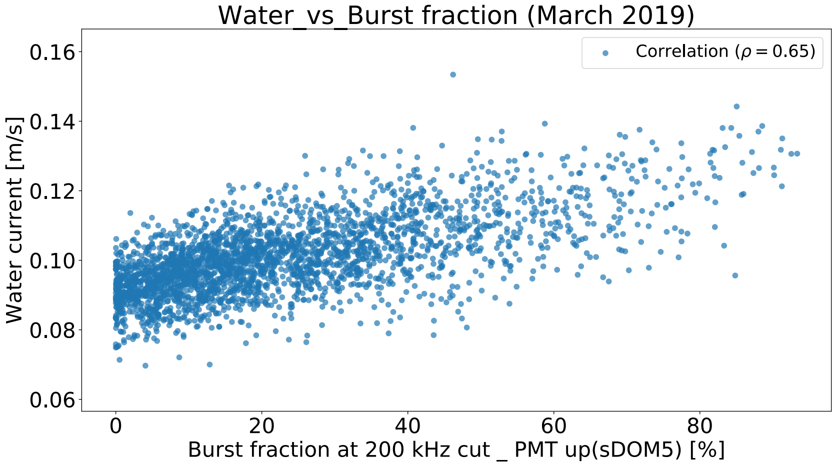

Figure 5.26: Correlation plot between the water current and the burst fraction for March 2019: the correlation factor for this data-set is 0.65.

0.57, see fig. 5.27, but still indicating an association with the currents. Indeed, as seen in fig. 5.22, high level of baselines are associated with high level of burst fraction.

This correlation studies, observed also by other similar experiments [83] [84], could be the starting point for identifying periods of high biolumi-

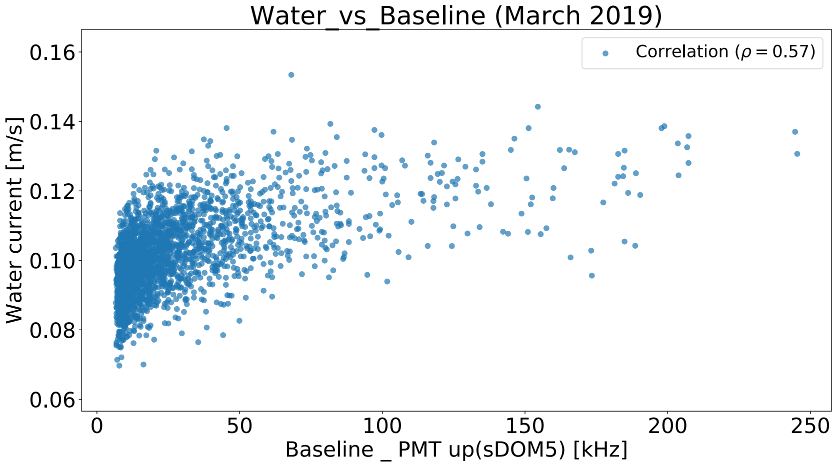

Figure 5.27: Correlation plot between water current and baselines for March 2019: the correlation factor for this data-set is 0.57.

nescence activity taking into account the only monitoring of the currents, in case an ADCP or a current meter is installed next to a mooring. Indeed, the possibility of installing several ADCP devices next to the future P-ONE strings is under investigation as will be one of the fundamental tools.

5.6 Sedimentation and biofouling

The *sedimentation* is an effect due to the downward flux of sediment in the deep-sea that can cover submerged structures. In a neutrino telescope environment such a phenomenon can progressively obscure upwards looking modules.
The *biofouling* (accumulation of layers of biological organisms) is a second effect that naturally occurs on any surface in water and that can also increase the sediment capture.
Since a neutrino telescope is designed in order to taking data for years, it is crucial to monitor the impact that these two phenomena have on the optical modules surfaces.
The effect of *sedimentation* and *biofouling* on the modules of a neutrino telescope has been largely investigated also by the ANTARES experiment: for a long period, the evolution of the light transmission through the glass surface of the deployed modules has been studied, drawing the conclusion that the accumulation of light-absorbing material is only significant for upwards surfaces [85]. Furthermore, when the water currents is strong can happen that the sedimentation and biofouling layer is partially washed off,

increasing the light transmittance [80].

Following the above mentioned studies I have analysed the modules rates trying to identify in STRAW detector the sedimentation effect. The strategy used has been to quantify the detected rate difference between the $\text{PMT}_{\boldsymbol{up}}$ and the $\text{PMT}_{\boldsymbol{down}}$ with respect to the $\text{PMT}_{\boldsymbol{up}}$ for every sDOM, making the assumption that the sedimentation is not affecting (or affecting in a very neglectable way) the downward looking PMT; thus calculating the following *ratio*:

$$\frac{\boldsymbol{(ratePMT_{up} - ratePMT_{down})}}{\boldsymbol{ratePMT_{up}}} \tag{5.6}$$

In principle, on average, both PMTs of an sDOM should detect the same amount of signals (even during bioluminescence activity) but, if the sedimentation and the biofouling is affecting the PMT looking upward, the ratio trend has a negative slope. To study the overall effect of the phenomenon, I have considered the 16 months data-set used so far. Also in this case, the data set is sampled every 12 hours to smooth as much as possible local and short-time dependent variations between PMT rates. The result is shown in fig. 5.50. This plot is also reported in a full-page size in the appendix 5.A at the end of this chapter.

The red lines are the fitted lines, whose slopes are indicative of the sedimentation effect. Since the slopes are negative, this represents a decrease in the detection efficiency of the upward-looking PMT with respect to the downward-looking one.

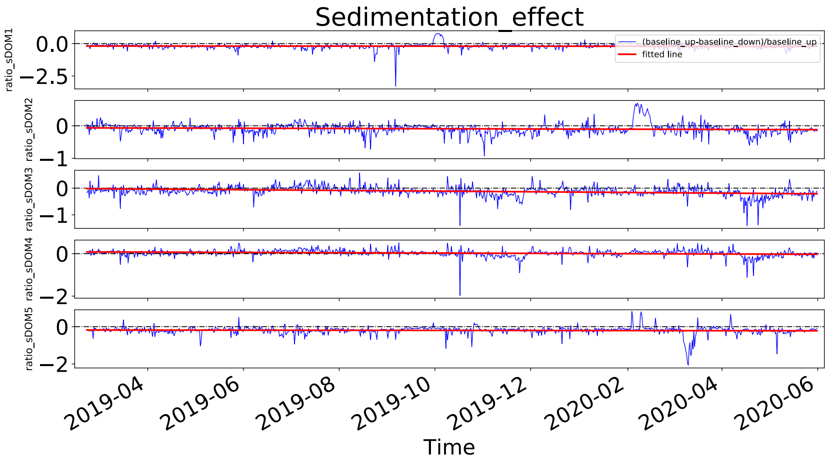

Figure 5.28: Ratio trend for all the sDOMs. The negative slopes of the fitted lines (in red) represent a decrease in the detection efficiency.

If no sedimentation would have affected the optical modules, the red line would have been parallel to the x-axes.

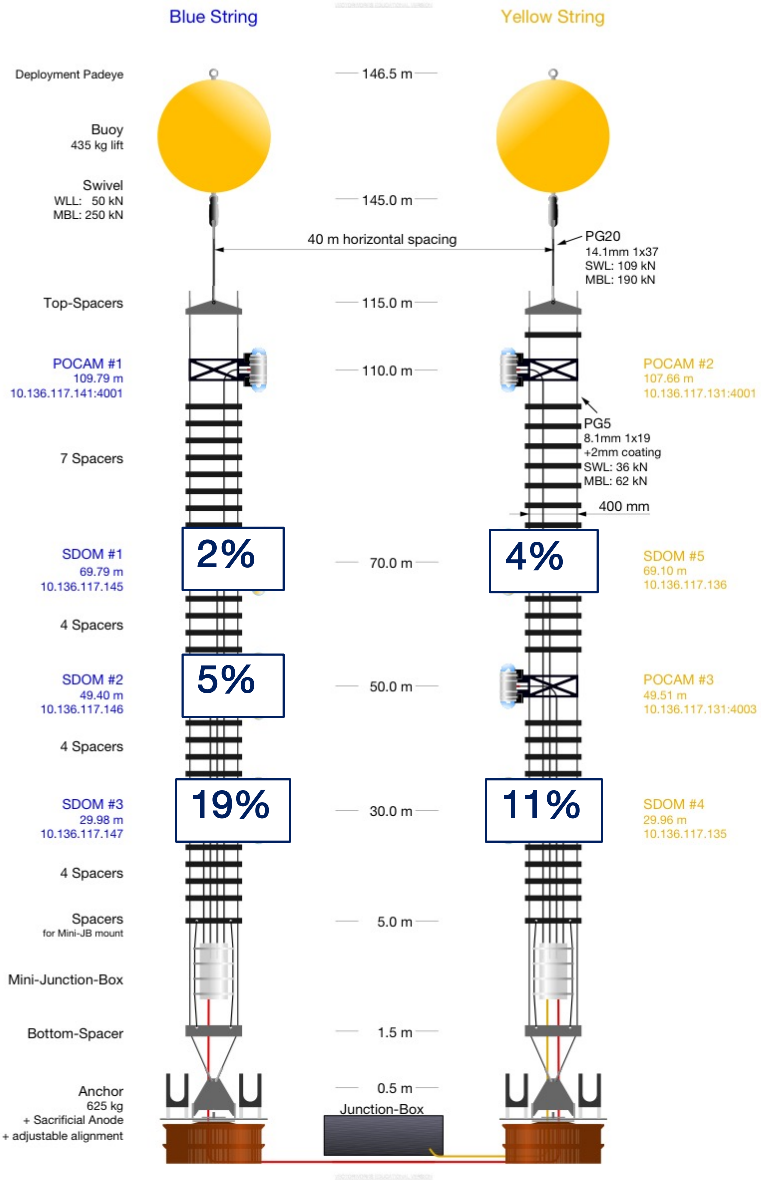

Figure 5.29: Sketch of the STRAW moorings indicating the percentage total loss in signal detection per module for the investigated period of 16 months: ∼ 2% for the sDOM1, ∼ 5% for the sDOM2, ∼ 19% for the sDOM3, ∼ 11% for the sDOM4 and ∼ 4% for the sDOM5.

The total loss in signal detection per module for the investigated time window is calculated as follows:

$$\boldsymbol{r_f - r_i = m(t_f - t_i)} \tag{5.7}$$

where $\boldsymbol{r_{f/i}}$ is the ratio of the PMTs up and down rates as expressed above, $\boldsymbol{m}$ is the slope of the fit line and $\boldsymbol{t_{f/i}}$ is the time. The values obtained and expressed in percentage are of $\sim$ 2% for the sDOM1, $\sim$ 5% for the sDOM2, $\sim$ 19% for the sDOM3, $\sim$ 11% for the sDOM4 and $\sim$ 4% for the sDOM5. From the sketch shown in fig. 5.29 and in fig. 5.30, it can be seen that the sedimentation effect increases at higher depth. We can not draw final conclusions about this potential correlation because the depth is not the only parameter that influences the sedimentation on the modules.

In September 2020, prior the deployment of STRAWb, the ROV inspected the STRAW lines, in water since 2 and half years. The ROV camera took pictures of all sDOMs, see fig. 5.31 and fig. 5.32, revealing the presence of both biofouling and sediment on the glass hemispheres.

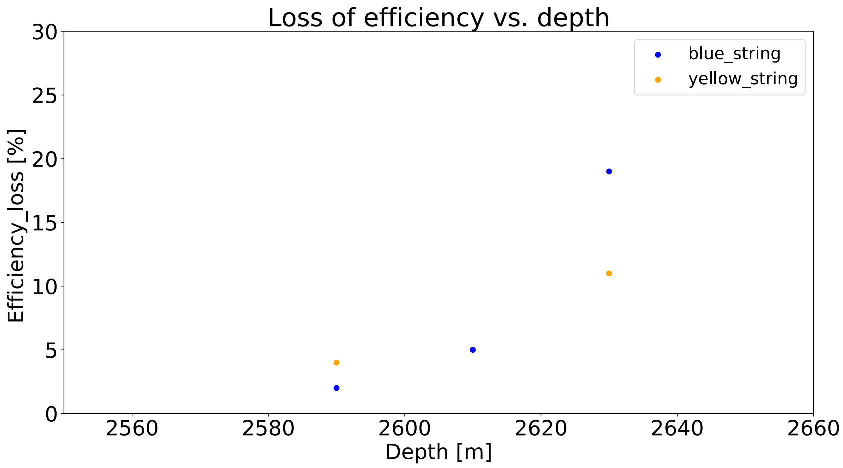

Figure 5.30: Percentage efficiency losses vs. depth for the 5 sDOMs of the blue string and the yellow string.

We have studied the sedimentation on STRAW modules. The observed effect did not alter the optics of the detector massively. These losses were minimal and expected and might not play a dominant role in P-ONE. We will continue to monitor this effect over time as it will be beneficial for future design and detection efficiency simulation. We will also investigate the possibility of detector maintenance in the future.

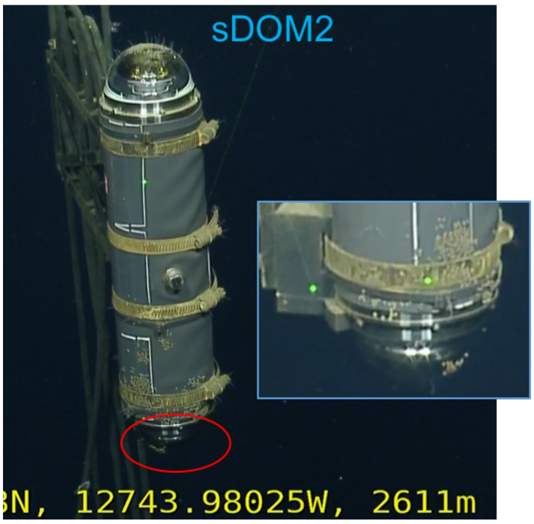

Figure 5.31: Picture of the sDOM2 taken during the inspection of STRAW moorings in September 2020: the presence of both biofouling and sediment on the glass hemispheres is visible.

Figure 5.32: Picture of the sDOM3 taken during the inspection of STRAW moorings in September 2020: the presence of both biofouling and sediment on the glass hemispheres is visible.

5.7 Rates periodicity study

An interesting aspect of the observed data is how they behave in time. The goal of this analysis is to find periodicities in the data stream and, if any, to relate them with environmental parameters like water current, temperature and salinity.
As widely described in previous paragraphs, the bioluminescence is strictly

connected with water currents and tides. These latter are associated to sea convection events, generated by wind drifts (caused by the Coriolis force, as a result of the rotation of the Earth).

The deep-sea convection plays a major role in renewing the deep waters: in this way the biological activity increases (higher bioluminescence emission) as the deep-sea ecosystem is feeded with new nutrients, oxygen and new organisms.

These water movements can influence not only the speed of the currents but also the water temperature. For this reason some periodicities in the bioluminescence events are expected and, in this framework, changes in water current, temperature and salinity can be considered as warning signs for the increased bioluminescence activity.

For the identification of periodicities in detected signals, it is helpful to analyse the data in their frequency domain.

The *frequency domain* is the analytic space in which signals are expressed in terms of frequency, rather than in terms of time: as a time domain function shows changes over time, a frequency domain function shows how that function is distributing over the different frequency bands.

It is possible to convert a time domain function *x(t)* into a frequency domain function *X(ω)* using the Fourier Transform 5.8 or tools derived from it.

$$\boldsymbol{X(\omega) = \int_{-\infty}^{+\infty} x(t)\mathrm{e}^{-i2\pi\omega t}\, dt} \tag{5.8}$$

Using the Eulero formula 5.9, it is easily deducible that the Fourier Transform decomposes a time domain function in a sum of sinusoidal functions with different frequencies, amplitudes and phases.

$$\boldsymbol{e^{-i2\pi\omega t} = cos(2\pi\omega t) - isen(2\pi\omega t)} \tag{5.9}$$

For many data analysis applications, Fourier Transform methods are widely effective and produce good results, but for a better frequency resolution other more advanced methods of spectral estimation are used [86].

For example, if the total energy of a signal is finite, in order to describe how this energy is distributed over frequencies, one can define the *Energy Spectral Density* (ESD).

Starting from the definition of the signal energy in 5.10, for the Parseval's theorem[12] it can be re-written using the identity expressed in 5.11, where *X(ω)* is the Fourier Transform of *x(t)*; the integrand $\boldsymbol{|X(\omega)|^2}$ then can be interpreted as the density function that describes the energy per frequency unit.

$$\boldsymbol{E = \int_{-\infty}^{+\infty} |x(t)|^2\, dt} \tag{5.10}$$

---

[12] Parseval's Theorem: The sum (or integral) of the square of a function is equal to the sum (or integral) of the square of its Fourier Transform.

$$\int_{-\infty}^{+\infty} |x(t)|^2 \, dt = \int_{-\infty}^{+\infty} |X(\omega)|^2 \, d\omega \tag{5.11}$$

Hence the ESD can be defined as in the equation 5.12:

$$S_E(\omega) = |X(\omega)|^2 \tag{5.12}$$

Following one of the properties of the *Cross-Correlation*[13], the *Energy Spectral Density* in 5.12 turns out to be the Fourier Transform of the auto-correlation function of x(t), see 5.13 (where the auto-correlation is defined the cross-correlation of a function with itself).

$$\mathcal{F}\{x(t) * x(-t)^*\} = X(\omega) \cdot X^*(\omega) = |X(\omega)|^2 \tag{5.13}$$

Similar to as described above, if a signal has a finite power over an interval of time T, then one can define also the *Power Spectral Density* (PSD) as in 5.14:

$$S_P(\omega) = \frac{1}{T} |X_T(\omega)|^2 \tag{5.14}$$

and for an infinite time this expression becomes as the following 5.15:

$$S_P(\omega) = \lim_{T \to +\infty} \frac{1}{T} |X_T(\omega)|^2 \tag{5.15}$$

interpreted as the spectral energy distribution per unit time.
The PSD measures the relative importance of possible frequency values that might explain the oscillation pattern of the observed data: it describes very well how recurrent is a certain frequency component in the *X(ω)* overall function and, besides potential repetitive patterns, also random structures are shown. The classical method for Power Spectral Density computation is based on a tool called *Periodogram*.
In all real cases, signal processing is applied to sampled and finite version *x[n]* of the real signal *x(t)*: for this reason, instead of the above mentioned Fourier Transform, it is necessary to consider the Discrete Fourier Transform of the sample *x[n]*, as in 5.16.

$$X_d(\omega) = \sum_{n=0}^{N-1} x[n] \mathrm{e}^{-i2\pi\omega n} \tag{5.16}$$

In this case, the Periodogram of a *x[n]* sample is 5.17:

$$S_x(\omega) = \frac{1}{N} \left| \sum_{n=0}^{N-1} x[n] \mathrm{e}^{-i2\pi\omega n} \right|^2 = \frac{1}{N} |X_d(\omega)|^2 \tag{5.17}$$

---

[13] The Cross-Correlation expresses a measure of the similarity of two functions with respect to the displacement of one relative to the other.

5.7.1 The Periodogram on STRAW data: yearly data-set

As a first step towards frequency spectrum identification, I applied the Periodogram tool to the STRAW data.
To search for periodicities over different time scales the approach has been twofold and two data-set have been considered:

- almost two years of data (18 months),
- each month.

In this first step of the analysis, the Periodogram has been applied to a data set of 18 months, from February 2019 to July 2020. Consistently as described in paragraphs 5.3 and 5.4, the modulations are present simultaneously on each sDOM. Plotting such a Periodogram for one sDOM in fig. 5.33, the y-axis represents the relative magnitude of the data pattern, while the x-axis represents the frequency range.

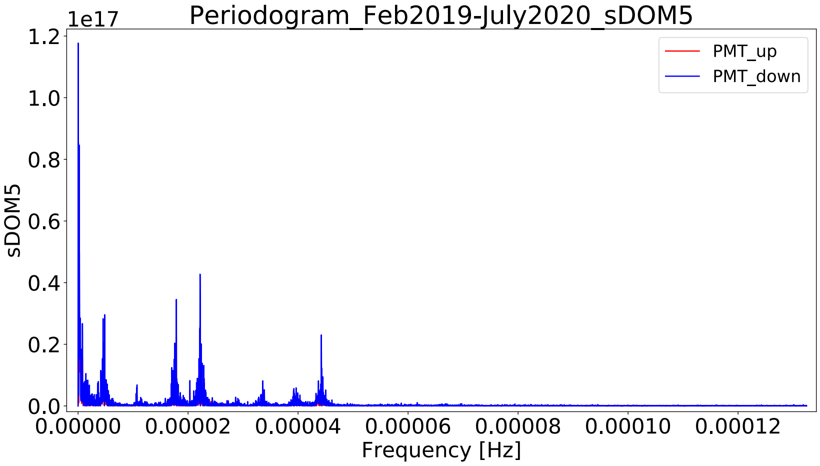

Figure 5.33: Periodogram of the STRAW 18 months data sample for the sDOM5.

The relative magnitudes analysis identifies the following periodicities over more than one year and half time window, see figures 5.34, 5.35, 5.36 and 5.37:

- 4227 h (∼6 months)
- 1400 h (∼2 months)
- 1148 h (∼1,6 months)
- 667 h (∼28 days)

- 551 h (∼23 days)
- 468 h (∼19,5 days)
- 393 h (∼16,4 days)
- 350 h (∼14,5 days)
- 60 h
- 26 h
- 24 h
- 15.6 h
- 12.4 h
- 8 h
- 7 h
- 6.2 h

The data have been averaged over 1 hour and, consequently, the minimum appreciable periodicity is not less than 2 hours and the maximum one corresponds to the maximum value of the time sample (527 days).

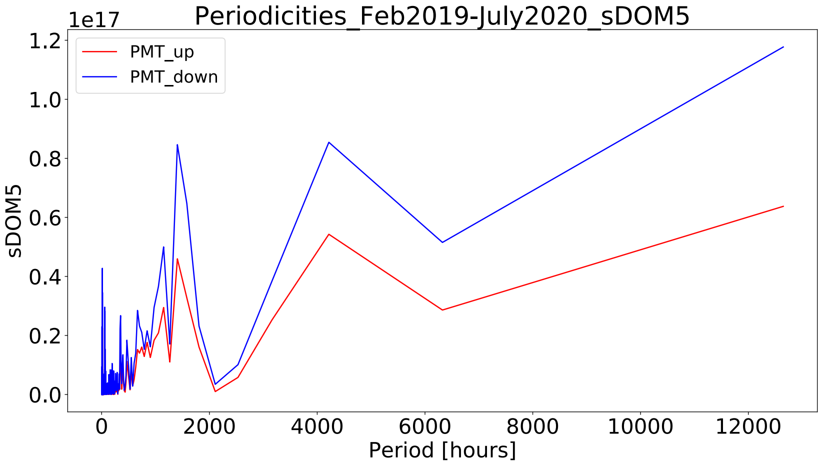

Figure 5.34: Periodicities of the entire data-set for the sDOM5: here are visible the periodicities of 4227 h (∼6 months), 1400 h (∼2 months), 1148 h (∼1,6 months), 667 h (∼28 days).

The Power Spectral Density that comes out from this analysis, represents the light background oscillations that, for the reasons mentioned in the previous sections, must be correlated with water current behaviours.

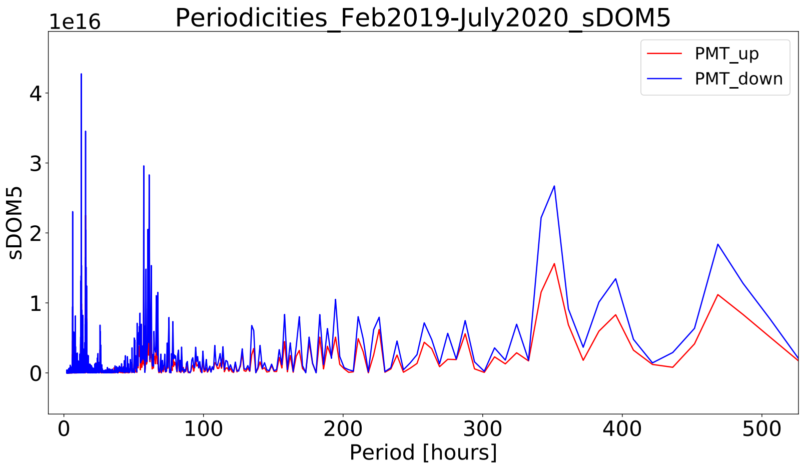

Figure 5.35: Zoom of the previous plot up to 500 h: other periodicities are appreciable as 468 h (∼19,5 days), 393 h (∼16,4 days) and 350 h (∼14,5 days).

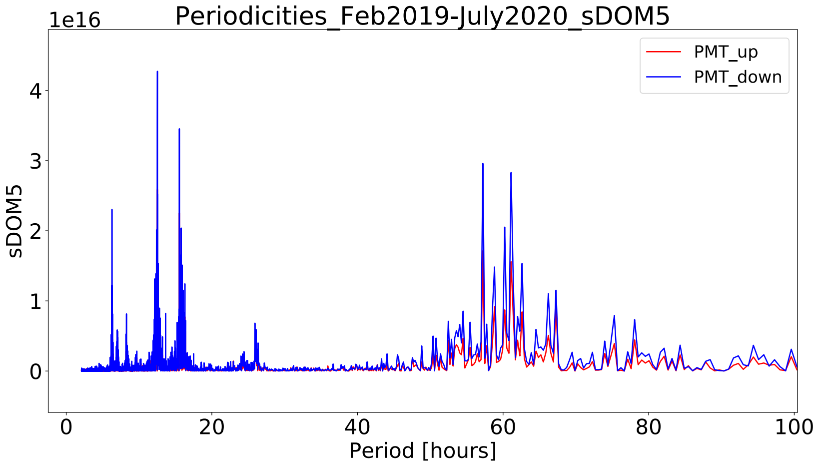

Figure 5.36: Zoom over the periods range up to 100 h: around 60 h there are several events.

Taking into account precious suggestions from Dr Steven Mihaly (ONC), I collected all the most inherent information on Cascadia Basin tides and deep water current, and tried to draw conclusions about some of the periodicities found:

- the current in Cascadia Basin can be influenced by warm water fluxes that come out from subseafloor, modify the water density structure

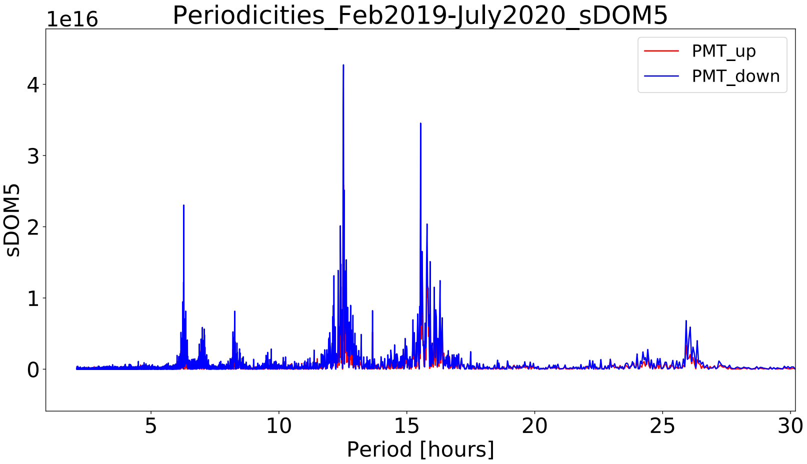

Figure 5.37: Zoom up to 30 h: these periodicities are representing those events that occur during *one day* with different frequencies as 26 h, 24 h, 15.6 h, 12.4 h, 8 h, 7 h, 6.2 h.

and lead to deep subsea currents;

- the *high frequency* variability in the periodogram can be associated with local turbulences caused by small currents while the *low frequency* variability can be associate with the passage of deep eddies (both phenomena make the microorganisms impact on STRAW strings thus generating bioluminescence);

- the expected dominant periodicities in currents are at ∼12 h (*semidiurnal tide*), at ∼24 h (*diurnal tide*) and at the local inertial frequency of ∼16 h: STRAW data shows periodicities very close to these values and their harmonics, even if with very variable magnitudes. For example, STRAW 24 h periodicity magnitude is very low if compared to one of the semidiurnal tides at 12 h (the 6.2 h periodicity can be interpreted as its first harmonic such as 8 h periodicity can be the first harmonic of the local inertial frequency that in STRAW appears around 15.6 h).

- other expected periodicities are also fortnightly (15 days), monthly, semi-annual and annual tidal variability: in the yearly STRAW data-set fortnightly and monthly variability are identified respectively at ∼14,5 days and ∼28 days. The semi-annual periodicity appears exactly at 6 months. Surprisingly, no annual periodicity has been found: more investigations on this will follow considering longer periods.

5.7.2 The Periodogram on STRAW data: monthly data-set

After the research of periodicities over a very long time scale, the focus of this second phase of the analysis has been not only the periodicities research over smaller time scale but also the identification of a potential seasonal pattern as each month can add a different contribution to the data periodicity.
The data stream has been fragmented in months, as shown in fig. 5.38, thus generating smaller data-sets on which the Periodogram algorithm has been applied.
Choosing one PMT of the sDOM5 as a reference and overlapping the results from all 18 months, fig. 5.39, it can be appreciated that the monthly periodicities that appear are not exactly the same in each month and even when a particular periodicity is identified in more months, it can show variations in its magnitude. The figures 5.40, 5.41 and 5.42 display the periodicity distribution during an ideally time window of more than one day (30 hours), for the entire considered data-set.

Looking closely only two periodicities appear constantly in all months: 6 hours and 12 hours, where the first one has to be considered as the first harmonic of the second one (semidiurnal tide). The periodicity of $\sim$16 hours for example seems to disappear completely during summer 2019, even if it represents the local inertial frequency of Cascadia Basin.
The reasons for these differences need a properly investigation, as this is a very peculiar multidisciplinary topic that involves, besides physics, oceanography and marine biology. Still the goal of monitoring the light background periodicity over time is fundamental in order to know exactly at which time of the day/month/year a higher light background in the detected events is expected.

5.7.3 Environmental parameters periodicity: hint for the global warming?

For the third and last step of this study I started to focus the attention back to the environmental parameters considering, beside the water current already mentioned in the paragraph 5.5, the oxygen dissolved into the water and the temperature.
Years of constant observation showed that as the Earth atmosphere is warming up, the same is happening with the oceans: waters can be impacted by persistent climate trends. From a study of the Institute of Ocean Sciences [87], has been seen that Pacific Ocean waters up to at least 1000 m depth have been warming and losing oxygen in the last 50 years. This process has a negative impact on marine ecosystem since life in the ocean requires oxygen to support flora and fauna metabolism.
Thus, as the oxygen levels are decreasing and the water temperature is

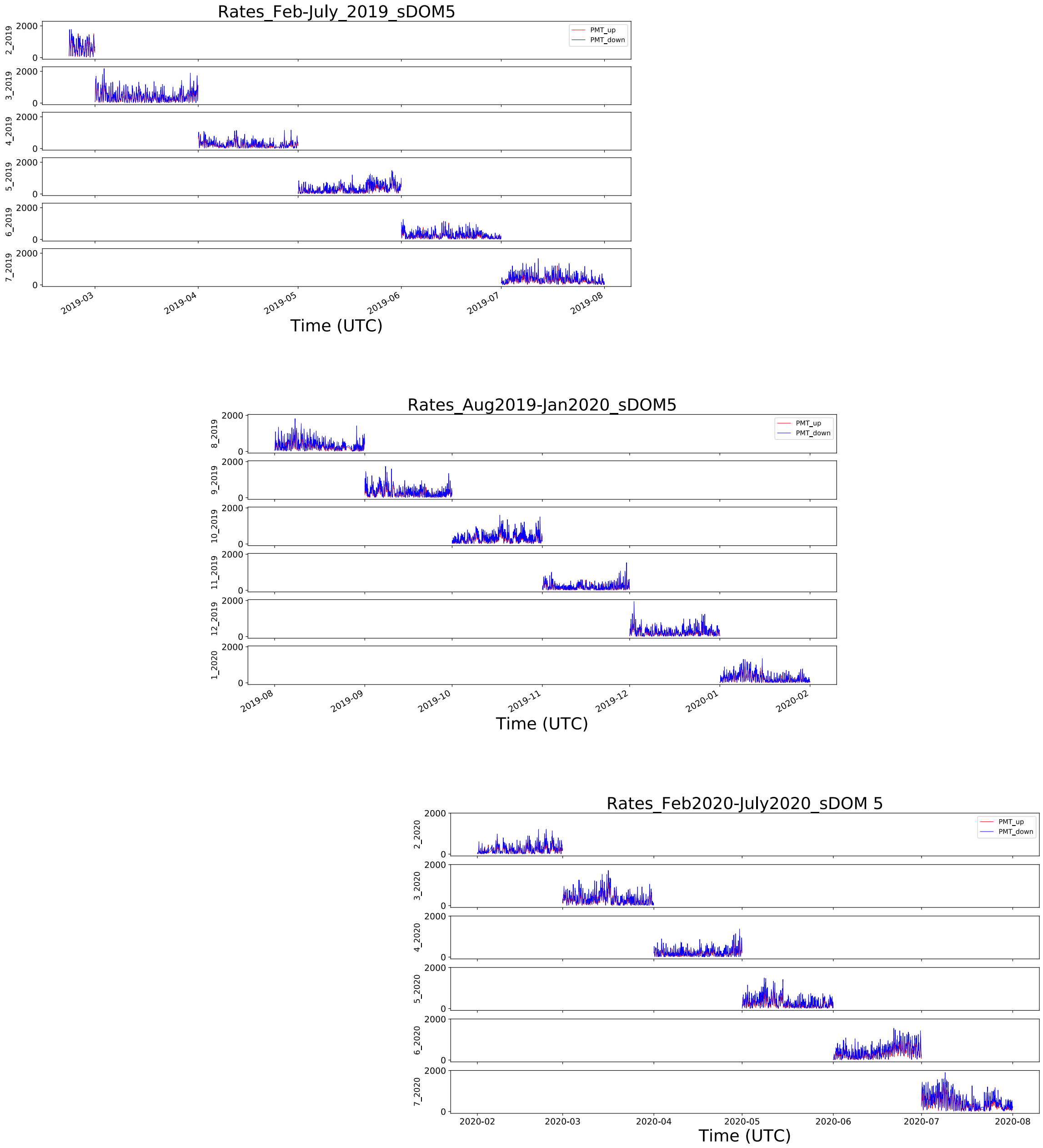

Figure 5.38: The Periodogram has been applied on smaller data-set of one month each in order to identify different contributions to the periodicity.

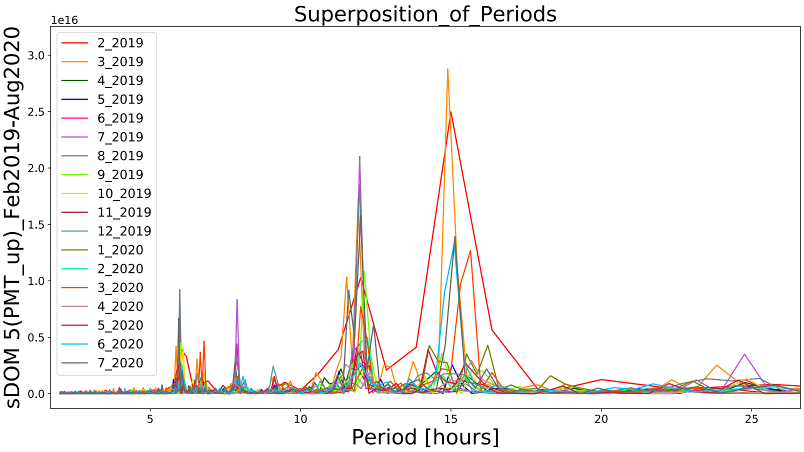

Figure 5.39: Superposition of periodicities belonging to different 18 months for one PMT of the sDOM5 (zoomed up to 30h period). Monthly periodicities are not exactly the same in each month, showing also variations in their magnitudes.

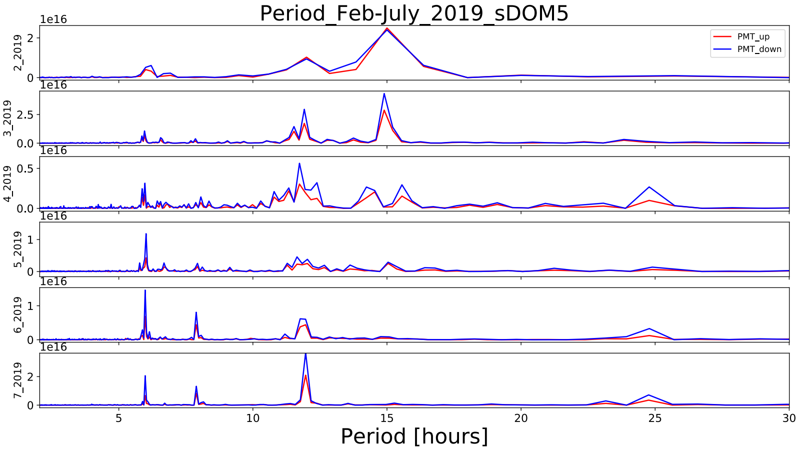

Figure 5.40: Periodicity for the sDOM5 from February 2019 to July 2019 (zoom on 30 hours period).

increasing, could the monitoring of variations in the deep-sea bioluminescence background trace this signature?
How the light background could be influenced by this process?
In view of this I started to collect information about heat waves in Cascadia Basin that could have potentially influenced STRAW rates. This study is still in a very embryonic stage, but I illustrate here a potential strategy for

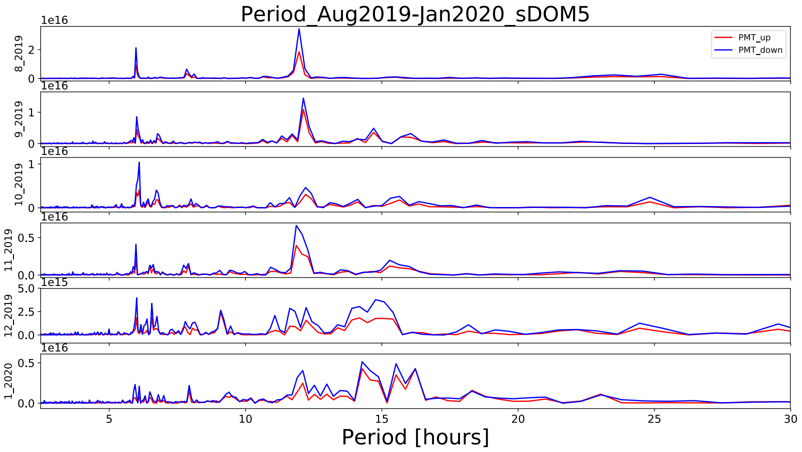

Figure 5.41: Periodicity for the sDOM5 from August 2019 to January 2020 (zoom on 30 hours period).

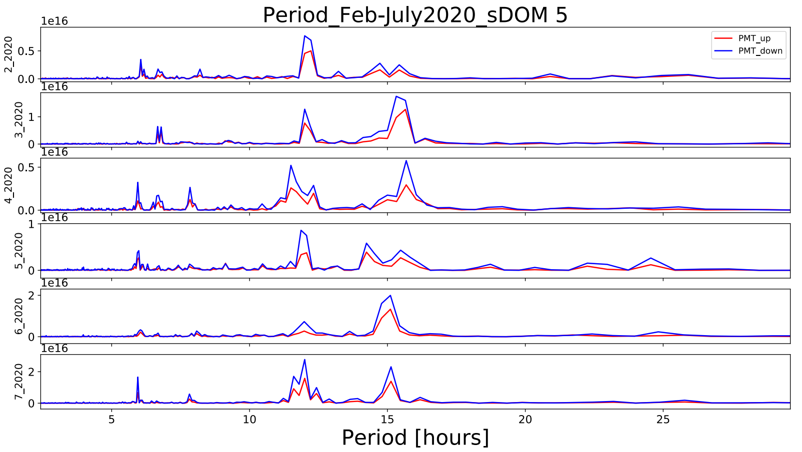

Figure 5.42: Periodicity for the sDOM5 from February 2020 to July 2020 (zoom on 30 hours period).

a future investigation.
The idea is that since water currents can affect deep ocean temperatures, one can expect that an investigation on the deep eddies and tides periodicities (besides showing a strict connection to the background light detected signals periodicity) can show corresponding periodicities in the temperature trend; also it could be possible to find the same periodicities in the trend of the oxygen dissolved into the water.

It is well known that, the trend of the temperature and the oxygen are completely simmetric to each other (anticorrelated): one explanation can be that high temperature stimulates metabolic functions of deep-sea organisms that consume more oxygen. In fig. 5.43 I took as an example one month of data (averaged over 15 minutes), March 2019, for one sDOM in order to compare the trends of rates, water current, temperature and oxygen.

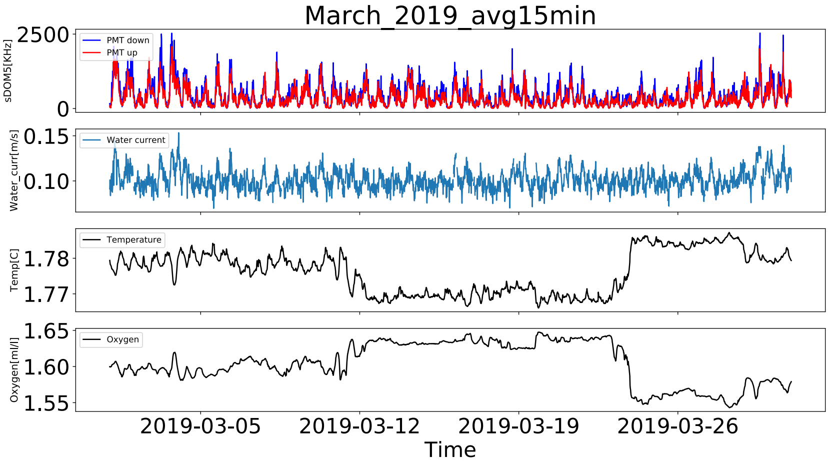

Figure 5.43: Example of March 2019 data stream (averaged over 15 minutes) for one sDOM. Trends of detected rates, water current, temperature and oxygen can be compared.

Applying the Periodogram algorithm to these quantities, see fig. 5.44, the main periodicities found confirmed of course the correlation between water current and STRAW rates, as already discussed in paragraph 5.5.

From the plot is appreciable that water masses movements influence the bioluminescence activity and the temperature for some periodicities; the rest of the periodicities that appear in the temperature plot should depend on other (for the moment unknown) parameters. The corresponding periodicities in the oxygen trend are not matching perfectly with the temperature ones: this can be attributed to the very small data sample taken into account and for the moment no conclusion can be drown from this.
In the next future more studies will follow.
In a multidisciplinary framework then, a deep-sea neutrino telescope permanently connected to the shore can provide synergetic opportunities for continuous long term deep-sea parameters observations, global warming effects and climate change.

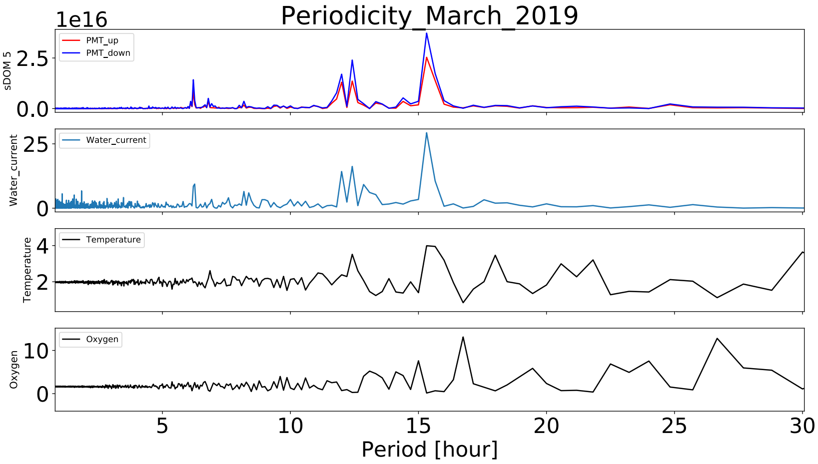

Figure 5.44: Periodicities found for March 2019 on the same sDOM as in 5.43. Water current is correlated not only with STRAW rates but also with temperatures (at least for some periodicity). More investigations on the oxygen periodicities are needed.

5.8 Sightings of Pyrosomes in STRAW

Pyrosomes are colonial tunicates usually living in shallow water in warm seas whose size ranges from less than one centimetre to several metres in length. Their name comes from the Greek *pyro* which means "fire" and *soma* which means "body", strictly referred to their property of emitting light.

For the past 30 years, pyrosomes have been found in waters off southern California but during spring and summer 2016, they have started to be collected also off shore Vancouver Island [88]. In spring and summer 2017, it was registered an anomalous bloom of pyrosomes with very high presence of large colonies from California to Alaska, along the NE Pacific. The causes of all this are under investigation, most probably they are related to the marine heat wave of 2014-2015 and to the El Niño during 2016: pyrosomes could have found an environment which provided enough warm temperatures and food for their reproduction.

More observations during November 2017 suggested that environmental conditions could have been favourable for another bloom in the summer of 2018, in coincidence with STRAW deployment.

In July 2018, one month after the deployment, the ONC team performed the survey of the 2 STRAW moorings. Thanks to the picture from the ROV it has been possible to see how the pyrosomes can entangle in the strings cables, see fig 5.45.

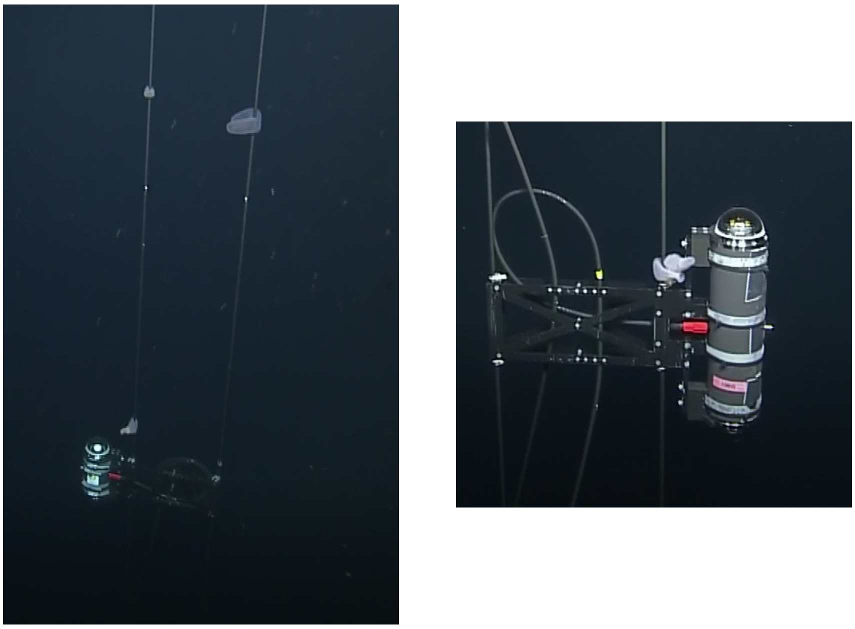

Figure 5.45: Pyrosomes entangled in the STRAW mooring lines. Pictures taken during the July 2018 ONC survey.

5.A Appendix

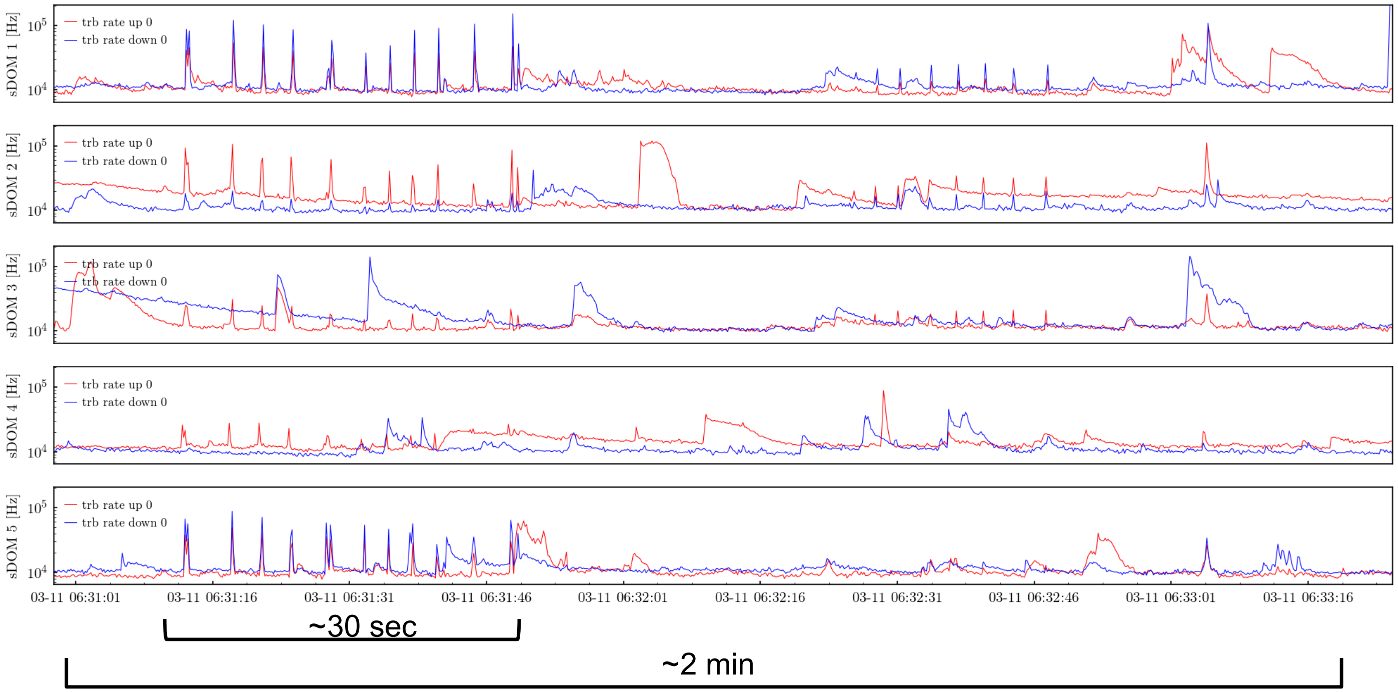

Figure 5.46: Bioluminescence event detected by all five sDOMs in STRAW. Several pulses in a time window of 30 sec can be appreciated. All credits for this plot to Dr Christian Fruck, TUM.

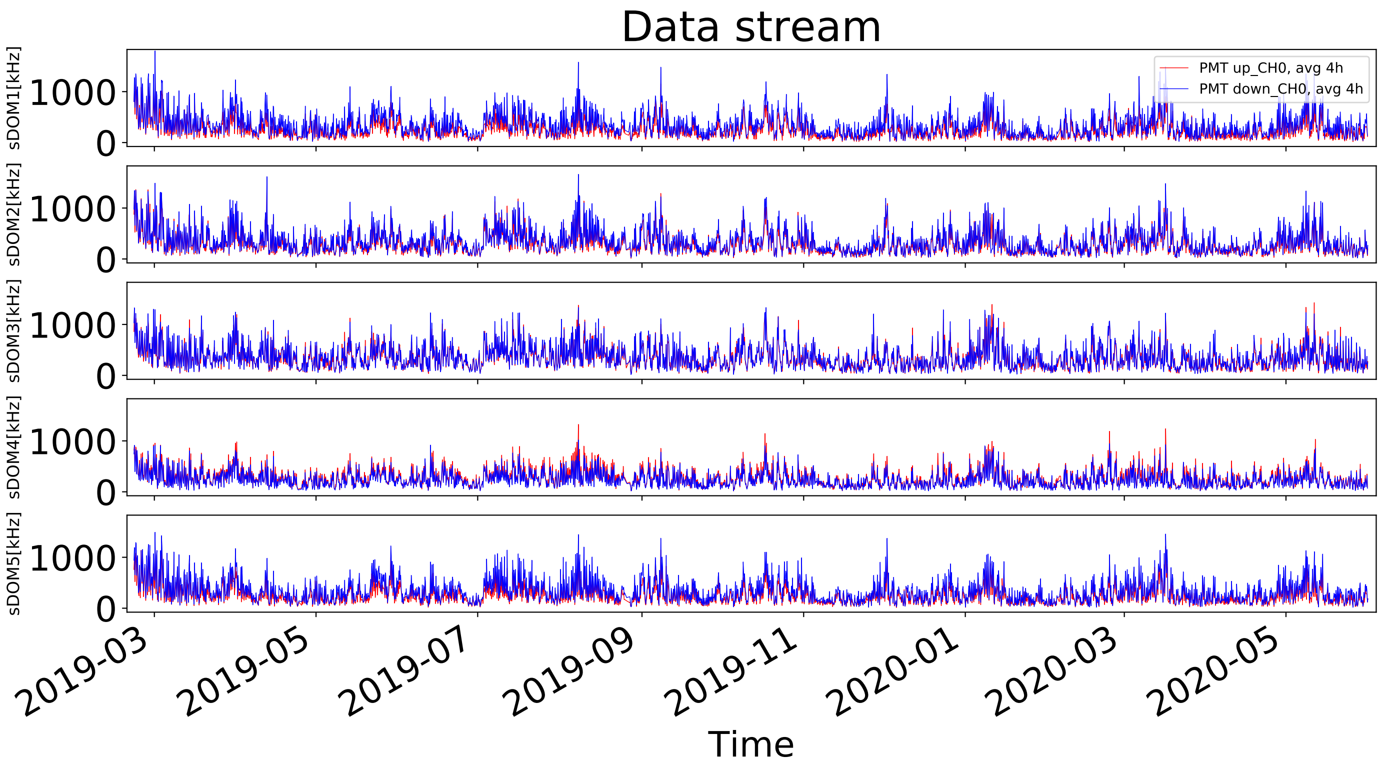

Figure 5.47: Data stream of the 5 sDOMs of STRAW: the data considered are taken from the end of February 2019 to the end of May 2020 and are avaraged every 4 hours. Periods of increased background level combined with higher bioluminescence activity can be seen.

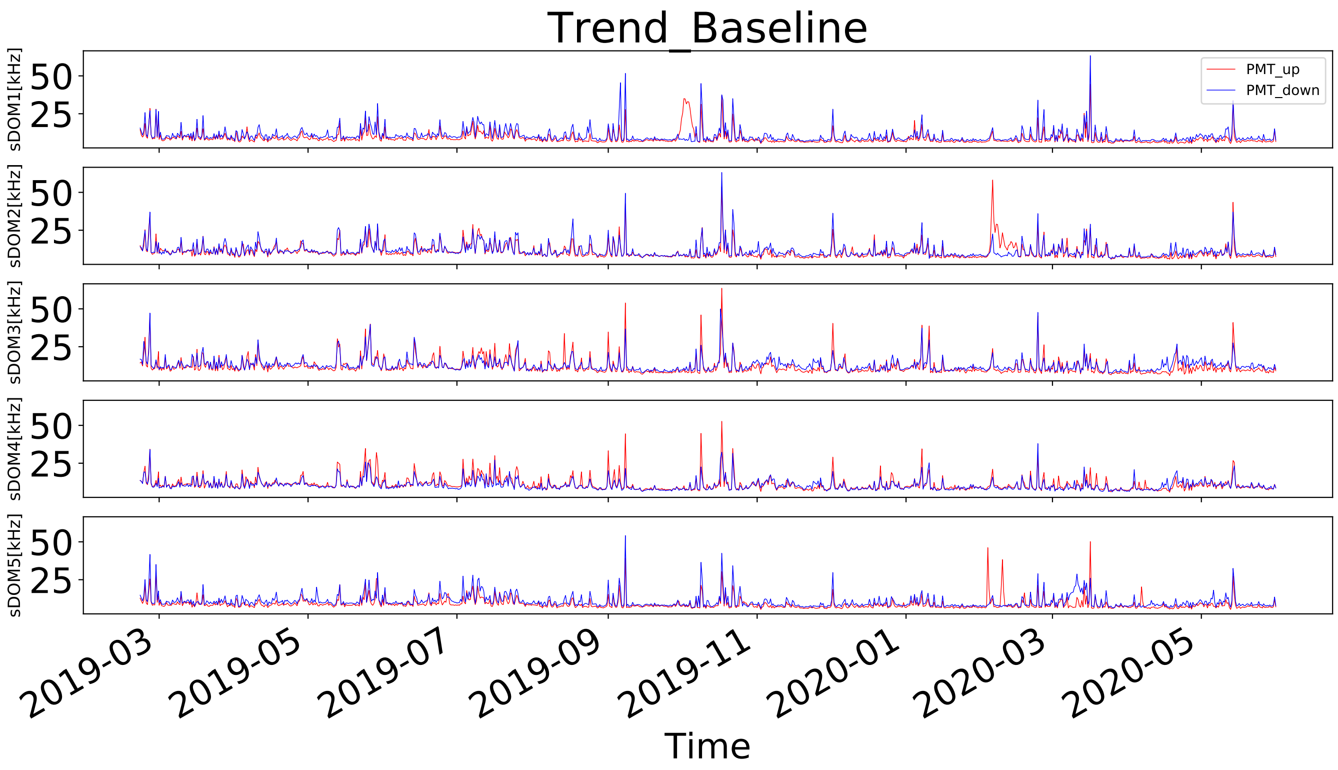

Figure 5.48: Trend over time of the baseline values: generally all sDOMs show the same behaviour. Sometimes exceptions can occur, and even two PMTs of the same sDOM can register different peak values.
In the time window from the end of February 2019 to the end of May 2020 the baseline varies between a minimum of ∼5 kHz and a maximum of ∼63 kHz.

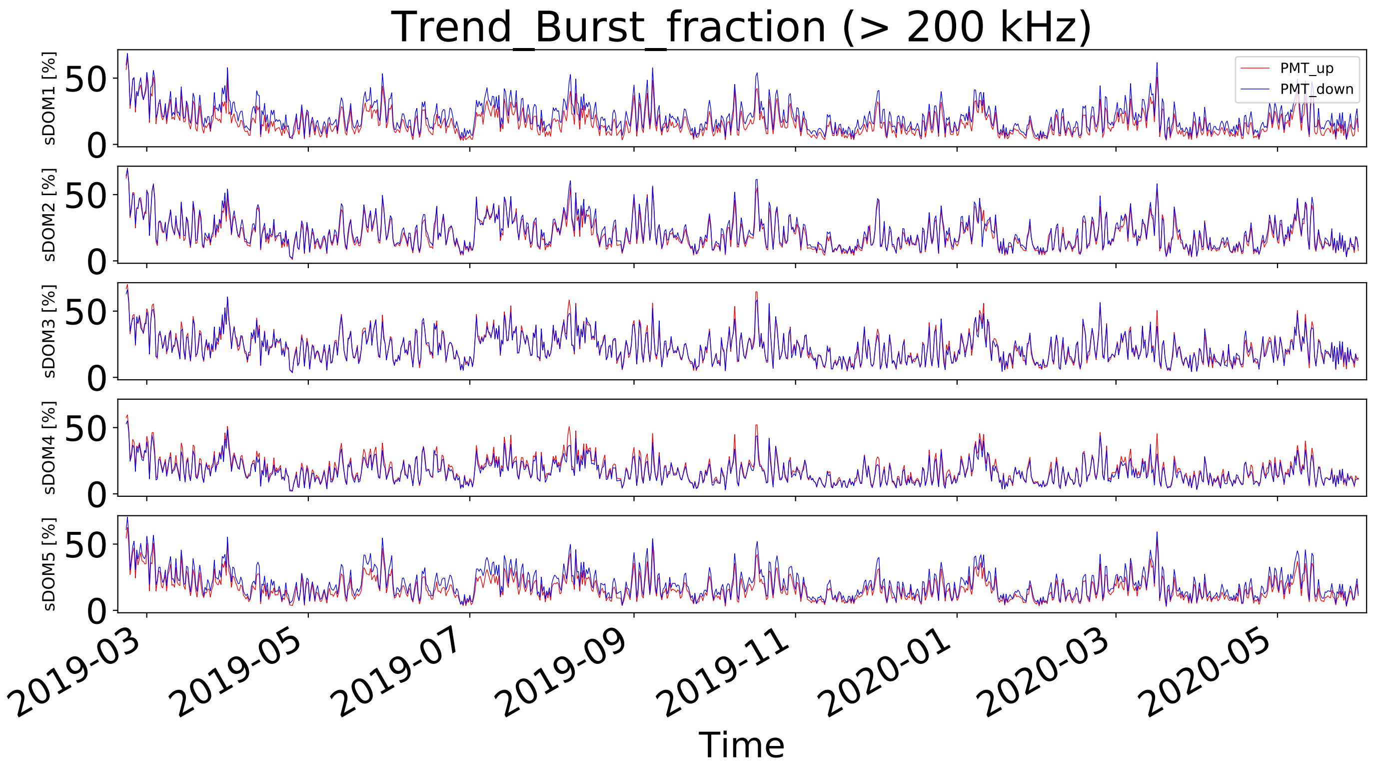

Figure 5.49: Evolution in time of the burst fraction, calculated as all the counted rates greater than 200 kHz.

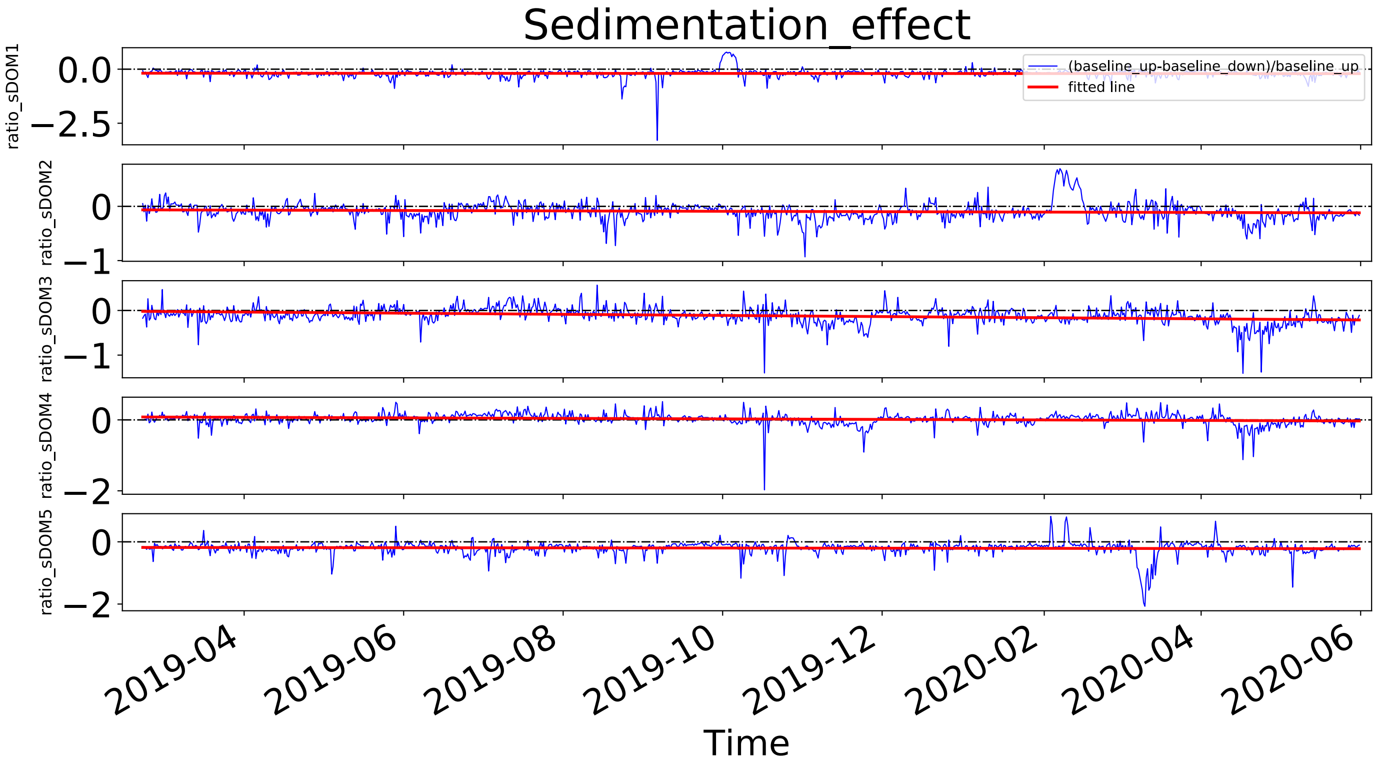

Figure 5.50: Ratio trend for all the sDOMs. The negative slopes of the fitted lines (in red) represent a decrease in the detection efficiency.

“ E finalmente io ti domando, oh uomo sciocco: Comprendi tu con l’immaginazione quella grandezza dell’universo, la quale tu giudichi poi essere troppo vasta?
Se la comprendi, vorrai tu stimar che la tua apprensione si estenda più che la potenza divina, vorrai tu dir d’immaginarti cose maggiori di quelle che Dio possa operare?
Ma se non la comprendi, perché vuoi apportar giudizio delle cose da te non capite? ”

Galileo Galilei,
"Dialogo sopra i due massimi sistemi", 1632

Conclusions

The Pacific Ocean Neutrino Experiment, P-ONE, is born from an idea of Prof. Elisa Resconi supported by the Ocean Networks Canada team and followed right after by the joint effort of other Canadian and North American universities.

Over the last four years, the TUM group focused on two pathfinders projects, STRAW and STRAW-b, pointing to the feasibility study of the candidate site chosen for the P-ONE telescope, Cascadia Basin.

STRAW, the first pathfinder, has been realised using optical calibration modules (POCAM) in combination with digital optical modules (sDOM), which enabled an initial approach to the development of what will later be the optical modules for P-ONE. STRAW allowed the first measurement of Cascadia Basin water *attenuation length* and the first monitoring of bioluminescence background intensities. The preliminary measurement of the attenuation length looked promising: at 465 nm wavelength L_c is around 30 m. The monitoring of bioluminescence background showed relatively low intensities and no significant burst period. Moreover, rates modulations on different time scales result directly correlated with underwater currents.

After the two years of monitoring, it has been possible also to measure the reduction of photon detection efficiency of the sDOMs caused by the biofouling and sedimentation effects. The obtained results are compatible with expectations and consistent with those of other neutrino telescopes currently taking data or under construction.

STRAW results stimulated the implementation of the second pathfinding phase, STRAW-b. This mooring line, equipped with ten different optical modules, aims to perform a second measurement of the attenuation length and characterise the background sources. In particular, the bioluminescence emission spectrum can be traced by the three spectrometer modules, covering in combination a wide dynamic range. The marine biology community is showing particular interest in STRAW-b as it will investigate for the first time bioluminescence emission spectrum *in situ*.

These studies are fundamental to evaluate Cascadia Basin water optical properties and all the collected data will be crucial for constraining the design of the P-ONE telescope.

Bibliography

[1] Maurizio Spurio. *Particles and astrophysics : a multi-messenger approach*. Springer, 2015.

[2] Marica Branchesi. Multi-messenger astronomy: gravitational waves, neutrinos, photons, and cosmic rays. *Journal of Physics: Conference Series*, 718:022004, may 2016.

[3] The IceCube Collaboration et. al. Multimessenger observations of a flaring blazar coincident with high-energy neutrino icecube-170922a. *Science*, 361(6398), 2018.

[4] Abbott et al. Observation of gravitational waves from a binary black hole merger. *Phys. Rev. Lett.*, 116:061102, Feb 2016.

[5] Immacolata Carmen Rea. AugerPrime: the upgrade of the Auger Observatory. Definition of photomultiplier characterization procedures and design of the test station. Master's thesis, Naples, Federico II University, 2016-06-15.

[6] C. Spannfellner. Development of pathfinder missions and instruments for the Pacific Ocean Neutrino Experiment. Master's thesis, Munich, Tech. U., 2020-04-15.

[7] *P.A. Zyla et al. (Particle Data Group), Prog. Theor. Exp. Phys. 2020, 083C01 (2020).*

[8] Thomas K. Gaisser, Ralph Engel, and Elisa Resconi. *Cosmic Rays and Particle Physics*. Cambridge University Press, 2 edition, 2016.

[9] Andrea Turcati. *Multimessenger searches for the sources of high energy cosmic rays: IceCube, Fermi, Auger, TA.* PhD thesis, Munich, Tech. U., 2019.

[10] Martin Asplund, Nicolas Grevesse, and A. Jacques Sauval. The solar chemical composition. *Nuclear Physics A*, 777:1–4, 2006.

[11] ENRICO Fermi. On the origin of the cosmic radiation. *Phys. Rev.*, 75:1169–1174, Apr 1949.

[12] Anthony M Hillas. The origin of ultra-high-energy cosmic rays. *Annual review of astronomy and astrophysics*, 22:425–444, 1984.

[13] Roberto Aloisio. Acceleration and propagation of ultra high energy cosmic rays. *Progress of Theoretical and Experimental Physics*, 2017.

[14] The Auger Collaboration. Correlation of the highest-energy cosmic rays with nearby extragalactic objects. *Science*, 318(5852):938–943, 2007.

[15] The Auger Collaboration. Observation of a large-scale anisotropy in the arrival directions of cosmic rays above $8 \cdot 10^{18}$ ev. *Science*, 357(6357):1266, 09 2017.

[16] A. A. Grib and Yu. V. Pavlov. Active galactic nuclei and transformation of dark matter into visible matter. *Gravitation and Cosmology*, 15(1):44–48, 2009.

[17] R. PENROSE and R. M. FLOYD. Extraction of rotational energy from a black hole. *Nature Physical Science*, 229(6):177–179, 1971.

[18] Alexander Aab et al. Inferences on mass composition and tests of hadronic interactions from 0.3 to 100 EeV using the water-Cherenkov detectors of the Pierre Auger Observatory. *Phys. Rev. D*, 96(12):122003, 2017.

[19] Karl-Heinz Kampert and Peter Tinyakov. Cosmic rays from the ankle to the cutoff. *Comptes Rendus Physique*, 15(4):318–328, 2014. Ultra-high-energy cosmic rays: From the ankle to the tip of the spectrum.

[20] Matthias Huber. *Multi-Messenger correlation study of Fermi-LAT blazars and high-energy neutrinos observed in IceCube*. PhD thesis, Munich, Tech. U., Munich, Tech. U.

[21] M. Ackermann, M. Ajello, A. Albert, W. B. Atwood, L. Baldini, J. Ballet, G. Barbiellini, D. Bastieri, K. Bechtol, R. Bellazzini, E. Bissaldi, R. D. Blandford, E. D. Bloom, E. Bottacini, T. J. Brandt, J. Bregeon, P. Bruel, R. Buehler, S. Buson, G. A. Caliandro, R. A. Cameron, M. Caragiulo, P. A. Caraveo, E. Cavazzuti, C. Cecchi, E. Charles, A. Chekhtman, J. Chiang, G. Chiaro, S. Ciprini, R. Claus, J. Cohen-Tanugi, J. Conrad, A. Cuoco, S. Cutini, F. D. Ammando, A. de Angelis, F. de Palma, C. D. Dermer, S. W. Digel, E. do Couto e Silva, P. S. Drell, C. Favuzzi, E. C. Ferrara, W. B. Focke, A. Franckowiak, Y. Fukazawa, S. Funk, P. Fusco, F. Gargano, D. Gasparrini, S. Germani, N. Giglietto, P. Giommi, F. Giordano, M. Giroletti, G. Godfrey, G. A. Gomez-Vargas, I. A. Grenier, S. Guiriec, M. Gustafsson, D. Hadasch, K. Hayashi, E. Hays, J. W. Hewitt, P. Ippoliti, T. Jogler, G. Jóhannesson, A. S. Johnson, W. N. Johnson, T. Kamae, J. Kataoka, J. Knödlseder, M. Kuss, S. Larsson, L. Latronico,

J. Li, L. Li, F. Longo, F. Loparco, B. Lott, M. N. Lovellette, P. Lubrano, G. M. Madejski, A. Manfreda, F. Massaro, M. Mayer, M. N. Mazziotta, J. E. McEnery, P. F. Michelson, W. Mitthumsiri, T. Mizuno, A. A. Moiseev, M. E. Monzani, A. Morselli, I. V. Moskalenko, S. Murgia, R. Nemmen, E. Nuss, T. Ohsugi, N. Omodei, E. Orlando, J. F. Ormes, D. Paneque, J. H. Panetta, J. S. Perkins, M. Pesce-Rollins, F. Piron, G. Pivato, T. A. Porter, S. Rainò, R. Rando, M. Razzano, S. Razzaque, A. Reimer, O. Reimer, T. Reposeur, S. Ritz, R. W. Romani, M. Sánchez-Conde, M. Schaal, A. Schulz, C. Sgrò, E. J. Siskind, G. Spandre, P. Spinelli, A. W. Strong, D. J. Suson, H. Takahashi, J. G. Thayer, J. B. Thayer, L. Tibaldo, M. Tinivella, D. F. Torres, G. Tosti, E. Troja, Y. Uchiyama, G. Vianello, M. Werner, B. L. Winer, K. S. Wood, M. Wood, G. Zaharijas, and S. Zimmer. THE SPECTRUM OF ISOTROPIC DIFFUSE GAMMA-RAY EMISSION BETWEEN 100 MeV AND 820 GeV. *The Astrophysical Journal*, 799(1):86, jan 2015.

[22] Joeran Stettner. Measurement of the diffuse astrophysical muon-neutrino spectrum with ten years of icecube data. 2019.

[23] The IceCube Collaboration. Icecube multi-messenger propagation, Jan 2018.

[24] A. Einstein. Näherungsweise integration der feldgleichungen der gravitation. *Sitzungsberichte der Königlich Preussischen Akademie der Wissenschaften Berlin.*, pages part 1: 688–696, 1916.

[25] A. Albert et al. Search for multimessenger sources of gravitational waves and high-energy neutrinos with advanced LIGO during its first observing run, ANTARES, and IceCube. *The Astrophysical Journal*, 870(2):134, jan 2019.

[26] T. Chiarusi and M. Spurio. High-energy astrophysics with neutrino telescopes. *The European Physical Journal C*, 65(3):649–701, 2010.

[27] M.A. Markov. On high energy neutrino physics. *Proceedings of the International Conference on High Energy Physics, University of Rochester, New York, NY, USA*, pages 578–581, 25 August - 1 September 1960.

[28] C. L. Cowan, F. Reines, F. B. Harrison, H. W. Kruse, and A. D. McGuire. Detection of the free neutrino: a confirmation. *Science*, 124(3212):103–104, 1956.

[29] Edward Kearns, Takaaki Kajita, and Yoji Totsuka. Detecting Massive Neutrinos. *Scientific American*, 281(2):64–71, August 1999.

[30] Hans-Thomas Janka. Neutrino emission from supernovae. *Handbook of Supernovae*, page 1575?1604, 2017.

[31] Roisín O'Rourke Brogan. Agn candidates for high energy neutrino emission in icecube. Master's thesis, Uppsala University, Disciplinary Domain of Science and Technology, Physics, Department of Physics and Astronomy, High Energy Physics, http://uu.diva-portal.org/smash/get/diva2:1426934/FULLTEXT01.pdf, February 2020.

[32] Daniele Vivolo. *A highly innovative design of a photomultiplier: prototypes, engineering and applications in astroparticle physics*. PhD thesis, Naples U., 2014.

[33] G. Mangano, G. Miele, S. Pastor, T. Pinto, O. Pisanti, and P. Serpico. Relic neutrino decoupling including flavour oscillations. *Nuclear Physics*, 729:221–234, 2005.

[34] Brent Follin, Lloyd Knox, Marius Millea, and Zhen Pan. First detection of the acoustic oscillation phase shift expected from the cosmic neutrino background. *Physical Review Letters*, 115(9), Aug 2015.

[35] A Faessler, R Hodak, S Kovalenko, and F Simkovic. Search for the cosmic neutrino background. *Journal of Physics: Conference Series*, 580:012040, feb 2015.

[36] Amand Faessler, Rastislav Hodak, Sergey Kovalenko, and Fedor Simkovic. Beta Decay and the Cosmic Neutrino Background. *EPJ Web Conf.*, 71:00044, 2014.

[37] Stefan Schönert, Thomas K. Gaisser, Elisa Resconi, and Olaf Schulz. Vetoing atmospheric neutrinos in a high energy neutrino telescope. *Physical Review D*, 79(4), Feb 2009.

[38] Edoardo Vitagliano, Irene Tamborra, and Georg Raffelt. Grand unified neutrino spectrum at earth: Sources and spectral components. *Rev. Mod. Phys.*, 92:045006, Dec 2020.

[39] P C Divari. Supernova neutrino reactions on114cd and116cd isotopes via charge current interaction. *Journal of Physics G: Nuclear and Particle Physics*, 40(12):125201, oct 2013.

[40] Gisela Anton. Neutrino telescopes. *Probing Particle Physics with Neutrino Telescopes*, pages 11–32, Jan 2020.

[41] Evidence for high-energy extraterrestrial neutrinos at the icecube detector. *Science*, 342(6161), 2013.

[42] M.G. Aartsen, M. Ackermann, J. Adams, Juan Antonio Aguilar Sánchez, M. Ahlers, M. Ahrens, David Altmann, Travi Anderson, G. Anton, C. Arguelles, Timothy Arlen, J. Auffenberg, S. Axani, Xiaoqiong Bai, I. Bartos, S.W. Barwick, V. Baum, Ryan Bay, J. Beatty, and M. Zoll. Icecube-gen2: A vision for the future of neutrino astronomy in antarctica. *arXiv:1412.5106*, 12 2014.

[43] Markus Ahlers, Klaus Helbing, and Carlos Pérez de los Heros. Probing particle physics with icecube. *The European Physical Journal C*, 78(11):924, 2018.

[44] Giulia De Bonis. Recent results of the antares neutrino telescope. *Nuclear and Particle Physics Proceedings*, 273-275:419–424, 2016.

[45] Jarosław Stasielak, Paweł Malecki, Dmitry Naumov, Vladimir Allakhverdian, Alexandra Karnakova, Konrad Kopański, Wojciech Noga, and on behalf of the Baikal-GVD Collaboration. High-energy neutrino astronomy—baikal-gvd neutrino telescope in lake baikal. *Symmetry*, 13(3), 2021.

[46] Rosa Coniglione. Results from the Mediterranean neutrino detectors. *PoS*, ICRC2019:006, 2019.

[47] Matteo Agostini, Michael Böhmer, Jeff Bosma, Kenneth Clark, Matthias Danninger, Christian Fruck, Roman Gernhäuser, Andreas Gärtner, Darren Grant, Felix Henningsen, Kilian Holzapfel, Matthias Huber, Reyna Jenkyns, Carsten B. Krauss, Kai Krings, Claudio Kopper, Klaus Leismüller, Sally Leys, Paul Macoun, Stephan Meighen-Berger, Jan Michel, Roger Moore, Mike Morley, Paolo Padovani, Laszlo Papp, Benoit Pirenne, Chuantao Qiu, Immacolata Carmen Rea, Elisa Resconi, Adrian Round, Albert Ruskey, Christian Spannfellner, Michael Traxler, Andrea Turcati, and Juan Pablo Yanez. The pacific ocean neutrino experiment. *Nature Astronomy*, 4(10):913–915, 2020.

[48] M. Boehmer, J. Bosma, D. Brussow, L. Farmer, C. Fruck, R. Gernhäuser, A. Gärtner, D. Grant, F. Henningsen, S. Hiller, M. Hoch, K. Holzapfel, R. Jenkyns, Na. Khera, Ni. Khera, K. Krings, C. Kopper, I. Kulin, K. Leismüller, J. Little, P. Macoun, J. Michel, M. Morley, L. Papp, B. Pirenne, C. Qiu, I. C. Rea, E. Resconi, A. Round, A. Ruskey, C. Spannfellner, and M. Traxler. STRAW (STRings for absorption length in water): pathfinder for a neutrino telescope in the deep pacific ocean. *Journal of Instrumentation*, 14(02):P02013–P02013, feb 2019.

[49] Immacolata Carmen Rea et al. STRAW-Strings for Absorption Length in Water Pathfinder for a Potential New Neutrino Telescope Site in the Pacific Ocean. *JPS Conf. Proc.*, 27:011016, 2019.

[50] A Capone, T Digaetano, A Grimaldi, R Habel, D Lo Presti, E Migneco, R Masullo, F Moro, M Petruccetti, C Petta, P Piattelli, N Randazzo, G Riccobene, E Salusti, P Sapienza, M Sedita, L Trasatti, and L Ursella. Measurements of light transmission in deep sea with the AC9 trasmissometer. *Nuclear Instruments and Methods in Physics Research Section A: Accelerators, Spectrometers, Detectors and Associated Equipment*, 487(3):423–434, July 2002.

[51] F. Henningsen. Optical Characterization of the Deep Pacific Ocean: Development of an Optical Sensor Array for a Future Neutrino Telescope. Master's thesis, Munich, Tech. U., 2018-07-19.

[52] A. Gartner. Development of an optical sensor system for the characterization of Cascadia Basin, Canada. Master's thesis, Munich, Tech. U., 2018-12-18.

[53] A. Gärtner. Realization of the "Precision Optical Calibration Module" prototype for calibration of IceCube-Gen2 . Master's thesis, Munich, Tech. U., 2016-07-24.

[54] M. Jurkovic, K. Abraham, K. Holzapfel, K. Krings, E. Resconi, and J. Veenkamp. A Precision Optical Calibration Module (POCAM) for IceCube-Gen2. *EPJ Web Conf.*, 116:06001, 2016.

[55] Zenith Polymer Diffuse Reflectance Standards, Targets and Materials. *For use over the UV, VIS and NIR spectral regions*, 2016.

[56] J.S. Kapustinsky et al. A fast timing light pulser for scintillation detectors. *Nuclear Instruments and Methods in Physics Research Section A: Accelerators, Spectrometers, Detectors and Associated Equipment*, 241(2):612 – 613, 1985.

[57] B.K. Lubsandorzhiev and Y.E. Vyatchin. Studies of 'Kapustinsky's' light pulser timing characteristics. *JINST*, 1:T06001, 2006.

[58] Roithner LaserTechnik GmbH. *XSL-365-5E*, 7 2010.

[59] Roithner LaserTechnik GmbH. *XRL-400-5E*, 9 2010.

[60] Nichia Corporation. *Specifications for blue LED*, 3 2012.

[61] Kingbright. *WP710A10LZGCK*, 7 2017. Rev. 3B.

[62] ROHM Semiconductor. *CSL0701x Series*, 11 2017. Rev. 6.

[63] A. Neiser et al. TRB3: a 264 channel high precision TDC platform and its applications. *JINST*, 8:C12043, 2013.

[64] Hamamatsu Photonics. *Hamamatsu Photonics, PHOTOMULTIPLIER TUBES - Basics and applications. 3rd edition. 2006.* 2013.

[65] S. Aiello et al. Characterisation of the Hamamatsu photomultipliers for the KM3NeT Neutrino Telescope. *JINST*, 13(05):P05035, 2018.

[66] Nautilus Marine Service GmbH. *Vitrovex by Nautilus Marine Service GmbH. 30.3.2020.url:https://www.vitrovex.com/.*

[67] S. Haddock and J. Case. Bioluminescence spectra of shallow and deep-sea gelatinous zooplankton: ctenophores, medusae and siphonophores. *Marine Biology*, 133:571–582, 1999.

[68] Li Ruohan. Development of STRAW-b: Strings for Absorption length in Water for Future Neutrino Telescope in Deep Pacific Ocean. Master's thesis, Munich, Tech. U., 2020-10-12.

[69] Eva Laura Winter. Muon Tracker for the Second Pathfinder of the Pacific Ocean Neutrino Explorer. Master's thesis, Munich, Tech. U., 2019-07-05.

[70] Edith Widder, Michael Latz, and James Case. Marine bioluminescence spectra measured with an optical multichannel detection system. *Biological Bulletin*, 165:791, 12 1983.

[71] Raymond C. Smith and Karen S. Baker. Optical properties of the clearest natural waters (200-800 nm). *Applied Optics*, 20:177–184, 01 1981.

[72] Curtis Mobley. Light and Water: Radiative Transfer in Natural Waters. *Academic Press*, 01 1994.

[73] J.A. Aguilar and A. et al. Albert. Transmission of light in deep sea water at the site of the ANTARES neutrino telescope. *Astroparticle Physics*, 23(1):131–155, Feb 2005.

[74] JG Learned. Proceedings of the 1980 International DUMAND Symposium. *II*, 272, 1980.

[75] G. Riccobene, A. Capone, et al. Deep seawater inherent optical properties in the Southern Ionian Sea. *Astroparticle Physics*, 27:1–9, 2007.

[76] Baikal Collaboration and V. A. Balkanov et al. In-situ measurements of optical parameters in Lake Baikal with the help of a Neutrino Telescope, 1999.

[77] Christian Fruck and Immacolata Carmen Rea. STRAW: STRings for Absorption length in Water. In *Proceedings of 36th International Cosmic Ray Conference — PoS(ICRC2019)*, volume 358, page 890, 2019.

[78] Ocean Networks Data Archive. *http://www.oceannetworks.ca, Ocean Networks Canada, University of Victoria, Canada*.

[79] A. Albert, M. André, M. Anghinolfi, G. Anton, M. Ardid, J. J. Aubert, J. Aublin, T. Avgitas, B. Baret, J. Barrios-Martí, S. Basa, B. Belhorma, V. Bertin, S. Biagi, R. Bormuth, J. Boumaaza, S. Bourret, M. C. Bouwhuis, H. Brânzaş, R. Bruijn, J. Brunner, J. Busto, A. Capone, L. Caramete, J. Carr, S. Celli, M. Chabab, R. Cherkaoui El Moursli, T. Chiarusi, M. Circella, J. A. B. Coelho, A. Coleiro, M. Colomer, R. Coniglione, H. Costantini, P. Coyle, A. Creusot, A. F. Díaz, A. Deschamps, C. Distefano, I. Di Palma, A. Domi, C. Donzaud, D. Dornic, D. Drouhin, T. Eberl, I. El Bojaddaini, N. El Khayati, D. Elsässer, A. Enzenhöfer, A. Ettahiri, F. Fassi, I. Felis, G. Ferrara, L. A. Fusco,

P. Gay, H. Glotin, T. Grégoire, R. Gracia Ruiz, K. Graf, S. Hallmann, H. van Haren, A. J. Heijboer, Y. Hello, J. J. Hernández-Rey, J. Hößl, J. Hofestädt, G. Illuminati, C. W. James, M. de Jong, M. Jongen, M. Kadler, O. Kalekin, U. Katz, A. Kouchner, M. Kreter, I. Kreykenbohm, V. Kulikovskiy, C. Lachaud, R. Lahmann, D. Lefèvre, E. Leonora, G. Levi, M. Lotze, S. Loucatos, M. Marcelin, A. Margiotta, A. Marinelli, J. A. Martínez-Mora, R. Mele, K. Melis, P. Migliozzi, A. Moussa, S. Navas, E. Nezri, A. Nuñez, M. Organokov, G. E. Păvălaş, C. Pellegrino, P. Piattelli, V. Popa, T. Pradier, L. Quinn, C. Racca, N. Randazzo, G. Riccobene, A. Sánchez-Losa, M. Saldaña, I. Salvadori, D. F. E. Samtleben, M. Sanguineti, P. Sapienza, F. Schüssler, M. Spurio, Th. Stolarczyk, M. Taiuti, Y. Tayalati, A. Trovato, B. Vallage, V. Van Elewyck, F. Versari, D. Vivolo, J. Wilms, D. Zaborov, J. D. Zornoza, and J. Zúñiga. Long-term monitoring of the antares optical module efficiencies using $$^{40}\mathrm{{k}}$$decays in sea water. *The European Physical Journal C*, 78(8):669, 2018.

[80] P. Bagley et al. KM3NeT: Technical Design Report for a Deep-Sea Research Infrastructure in the Mediterranean Sea Incorporating a Very Large Volume Neutrino Telescope. 2009.

[81] Tamburini C, Canals M, Durrieu de Madron X, et al. Deep-sea bioluminescence blooms after dense water formation at the ocean surface. *PLoS One*, 8(7):e67523, Jul 2013.

[82] Mark Bowlby, Edith Widder, and JAMES CASE. Patterns of stimulated bioluminescence in two pyrosomes (tunicata: Pyrosomatidae). *Biological Bulletin*, 179, 12 1990.

[83] P. Amram, S. Anvar, E. Aslanides, J-J. Aubert, R. Azoulay, S. Basa, Y. Benhammou, F. Bernard, V. Bertin, M. Billault, P-E. Blanc, F. Blanc, R.W. Bland, F. Blondeau, N. Bottu, J. Boulesteix, B. Brooks, J. Brunner, A. Calzas, C. Carloganu, E. Carmona, J. Carr, P-H. Carton, S. Cartwright, R. Cases, F. Cassol, C. Compere, S. Cooper, G. Coustillier, N. de Botton, P. Deck, F.E. Desages, J-J. Destelle, G. Dispau, J.F. Drogou, F. Drouhin, P-Y. Duval, F. Feinstein, D. Festy, J. Fopma, J-L. Fuda, P. Goret, L. Gosset, J-F. Gournay, J.J. Hernández, G. Herrouin, F. Hubaut, J.R. Hubbard, D. Huss, M. Jaquet, N. Jelley, E. Kajfasz, M. Karolak, A. Kouchner, V. Kudryavtsev, D. Lachartre, H. Lafoux, P. Lamare, J-C. Languillat, D. Laugier, J-P. Laugier, Y. Le Guen, H. Le Provost, A. Le Van Suu, L. Lemoine, P.L. Liotard, S. Loucatos, P. Magnier, M. Macelin, L. Martin, A. Massol, B. Mazeau, A. Mazure, F. Mazéas, J. McMillan, C. Millot, P. Mols, F. Montanet, J.P. Morel, L. Moscoso, S. Navas, C. Olivetto, N. Palanque-Delabrouille, A. Pallares, P. Payre, P. Perrin, A. Pohl, J. Poinsignon, R. Potheau, Y. Queinec, C. Racca, M. Raymond, J.F. Rolin, Y. Sacquin, J-P. Schuller, W. Schuster, N. Spooner, T. Stolarczyk, A. Tabary, M. Talby, C. Tao, Y. Tayalati, L.F.

Thompson, R. Triay, T. Tzvetanov, P. Valdy, P. Vernin, E. Vigeolas, D. Vignaud, D. Vilanova, D. Wark, A. Zghiche, and J. Zúñiga. Background light in potential sites for the ANTARES undersea neutrino telescope. *Astroparticle Physics*, 13(2):127 – 136, 2000.

[84] Garmt de Vries-Uiterweerd. *Signal and background in the underwater neutrino telescope ANTARES*. PhD thesis, Utrecht U., 2007.

[85] Collaboration Antares, P Amram, M Anghinolfi, Shebli Anvar, F Ardellier-Desages, E Aslanides, J.-J Aubert, R Azoulay, D Bailey, Shradhanjali Basa, M. Battaglieri, Roberto Bellotti, J Beltramelli, Y Benhammou, R Berthier, V Bertin, M Billault, R Blaes, R Bland, and André Monaco. Sedimentation and fouling of optical surfaces at the antares site. *Astroparticle Physics*, 19:253–267, 01 2003.

[86] Saeed V. Vaseghi. *Advanced Digital Signal Processing and Noise Reduction*. John Wiley and Sons, Inc., Hoboken, NJ, USA, 2006.

[87] Frank A. Whitney, Howard J. Freeland, and Marie Robert. Persistently declining oxygen levels in the interior waters of the eastern subarctic pacific. *Progress in Oceanography*, 75(2):179 – 199, October 2007.

[88] Richard Brodeur, Ian Perry, Jennifer Boldt, Linnea Flostrand, Moira Galbraith, Jacquelynne King, James Murphy, Keith Sakuma, and Andrew Thompson. *An unusual gelatinous plankton event in the NE Pacific: The Great Pyrosome Bloom of 2017*. 01 2018.